DYNAMIC DECOHESION OF BIMATERIAL INTERFACES

Thesis by

John Lambros

In Partial Fulfillment of the Requirements

for the Degree of

Doctor of Philosophy

California Institute of Technology

Pasadena, California

1994

(Submitted February 7, 1994)

To my family

The birth of high speed photography :

"In 1851 William Henry Fox Talbot attached a page of the London Times to a wheel, which he then rotated in front of his wet plate camera in a darkened room. As the wheel rotated, Talbot exposed a few square inches of the newspaper page for about 1/2000th of a second, using spark illumination from Leyden jars. This experiment resulted in a readable image and ushered in a new science and technology : high speed photography."

ACKNOWLEDGMENTS

The work presented in these pages has taken several years to conduct. Even though my name appears on the cover, I could not have completed it without the help of many individuals. I would like to thank some of these people here. First, I would like to thank my advisor, Prof. A. Rosakis, for his ideas, supervision, support and most of all friendship, during the, sometimes difficult, five years of my stay here. I would also like to thank Prof. W. G. Knauss for helping instill in me the fundamental concepts of elasticity during the two years I spent as a teaching assistant under his guidance. In addition, this project could not have been completed without the use of some of his laboratory equipment. I am also especially grateful to Prof. G. Ravichandran not only for his technical help when it was most needed, but also for the many lengthy discussions we had on all kinds of non-technical subjects. Also I would like to acknowledge Prof. J. Knowles' influence in showing me the importance of rigor and consistency, through his comprehensive lecturing and research technique.

I would like to thank each and every one of my fellow students for their friendship and support. I am especially thankful and lucky to have been in the company of people like Prof. J. Mason of the University of Notre Dame, Dr. G. Vendroux and most of all my long time roommate Dr. P. Geubelle. To all these people, and those who helped me during this time, I give my sincerest thanks.

Finally the financial support of ONR for the completion of this project is gratefully acknowledged.

ABSTRACT

In the present work, findings of an experimental study of dynamic decohesion of bimaterial systems composed of constituents with a large material property mismatch are presented. PMMA/steel or PMMA/aluminum bimaterial fracture specimens are used. Dynamic one point bend loading is accomplished with a drop weight tower device (for low and intermediate loading rates) or a high speed gas gun (for high loading rates). High speed interferometric measurements are made using the lateral shearing interferometer of Coherent Gradient Sensing in conjunction with high speed photography. Very high crack propagation speeds (terminal crack tip speeds up to $1.5c_s^{PMMA}$, where c_s^{PMMA} is the shear wave speed of PMMA) and high accelerations ($\approx 10^7$g, where g is the acceleration of gravity) are observed and reported. Issues regarding data analysis of the high speed interferograms are discussed. The effects of near tip three dimensionality are also analyzed. In crack propagation regions governed by large crack tip accelerations it is found that for accurate analysis of the optical data use of a transient elastodynamic crack tip field is necessary. Otherwise use of a K^d-dominant analysis is sufficient. Using the dynamic complex stress factor histories obtained by fitting the experimental data, a dynamic crack growth criterion is proposed. In the subsonic regime of crack growth it is seen that the opening and shearing displacements behind the propagating crack tip remain constant, i.e., the crack retains a self-similar profile during crack growth at any speed. This forms the basis of the proposed dynamic interfacial fracture criterion. It is also found that the process of dynamic interfacial fracture is highly unstable. This is corroborated by both the very large measured values of crack tip speed and acceleration and by the observation that the energy release rate at the propagating crack tip decreases with increasing crack tip speed. A mechanism of energy transfer from the metal to the PMMA side of the specimen is believed to be responsible for the high transient and transonic effects. An analysis and discussion of this phenomenon is also presented in this work.

TABLE OF CONTENTS

CHAPTER 1

INTRODUCTORY CONCEPTS

1.1 Motivation and Objectives

The use of advanced composite materials in engineering applications began several decades ago and has seen a continuous growth ever since. The McGraw-Hill Dictionary of Scientific and Technical Terms (4th ed.) defines a composite as "a structural material composed of combinations of metal alloys or plastics, usually with the addition of strengthening agents." In practical terms, composite materials come in many forms such as fiber or particulate reinforced polymer composites, metal matrix composites, laminates and others. Even though heralded as the materials of the future when they were first introduced, and despite their rapid growth and evolution, composites have not managed to replace metals as basic structural materials.

Primary reasons for the less than ideal performance of composites are their low ductility, low tensile strength and low fracture toughness. Observations of these traits have been made by several researchers (e.g., Hashin (1983), Evans (1989) and Mecholsky (1989)). Still ongoing research into the damage and failure modes of composite materials attempts to identify the phenomena that control the relatively low toughness of composites, and to improve their performance. For fiber reinforced laminate composites in particular, possible failure mechanisms that decrease strength and toughness include fiber-matrix debonding and ply delamination. These failure mechanisms may occur either quasi-statically in a structure subjected to static loading, or dynamically in a structure subjected to static or dynamic loading. In any event, eventual failure of the structure is always

catastrophic (dynamic) in nature. (This demonstrates the importance of analyzing dynamic effects in interface problems). Parameters that determine the size and type of fiber debonding are : the strength of the fiber-matrix interface and the elastic property mismatch between fiber and matrix (which is usually quite severe). In the case of ply delamination, the interlaminar interface strength is also important. Since these are all parameters that are related to interfacial effects, the implication is that local interfacial fracture behavior is important in evaluating the macroscopic toughness performance of composite structures. Local interfacial effects may be either at the fiber-matrix level or inter-laminate level. For these reasons, therefore, in recent years there has been a renewed interest in investigating interfacial fracture mechanics from a continuum point of view. (A brief description of recent findings of static linear elastic interfacial fracture mechanics is presented in section 1.2). Up to this point most of the research activity on interface fracture is on issues regarding the *quasi-static* failure of bimaterial systems. To fully understand the *catastrophic* nature of composite fracture, which is important in many engineering applications, a good understanding of *dynamic* interfacial fracture mechanics is necessary. Due to the complexity of this problem, however, only a few theoretical investigations have been made so far (Goldshtein (1967), Brock and Achenbach (1973), Willis (1971), Willis (1973), Atkinson (1977), Yang et al. (1991) and Deng (1991)). A single experimental study on this subject is currently available (Tippur and Rosakis (1991)).

In the current work we investigate the essentially unexplored area of experimental dynamic interfacial fracture mechanics. The general objective sought by this investigation is the understanding of the highly transient dynamic interfacial crack initiation, growth and arrest in bimaterial systems. In particular, in the context of the present thesis, it is intended to obtain a physically based and accurate criterion for crack initiation and growth in bimaterial systems. Use of high speed photography and interferometric optical diagnostics can provide real time measurements of mechanical fields at the vicinity of initiating and propagating interfacial crack tips. The particular optical method used here is the newly

developed method of Coherent Gradient Sensing (CGS). (Tippur et al. (1991), Rosakis (1993)) This is a full field lateral shearing interferometer which has shown great promise in real time imaging of dynamic crack tip fields in homogeneous materials. A detailed optical analysis of the method of CGS is given in section 2.1. In the same section the effect of near-tip three-dimensional deformations on the analysis of experimental data is discussed. Different loading configurations, involving an air gun or a drop weight tower, are used to provide impact loading for PMMA/steel or PMMA/aluminum bimaterial fracture specimens. The details of the experimental procedure are discussed in chapter 2. In chapter 3 the theoretical background necessary to quantitatively analyze the dynamic interferograms is given. In addition, results for the case of subsonic interfacial crack growth are presented in this chapter, and are discussed in the light of transient effects. The time history of fracture parameters extracted from the dynamic CGS interferograms is examined and used to propose a dynamic fracture criterion for bimaterial systems. The proposed criterion is presented and critically discussed in chapter 4. Experimental observations concerning transonic and intersonic crack growth along a bimaterial interface are described in chapter 5. Finally, in chapter 6 a summary of the main results of this investigation, along with a discussion of some possible future work on the subject, is presented.

1.2 Elements of static linear elastic interfacial fracture mechanics

In this section some general concepts of linear elastic interfacial fracture mechanics are presented. These concepts will subsequently be extended to dynamic fracture of interfaces later on in this manuscript.

The first investigation of the problem of static interfacial fracture mechanics is attributed to Williams (1959). He studied the stresses near the tip of a crack between two dissimilar elastic media. He showed that the resultant stresses exhibit a singularity of an oscillatory nature very close to the crack tip. The same type of singularity was observed by

(Sih and Rice (1964), Rice and Sih (1965), Erdogan (1965), England (1965) and Malyshev and Salganik (1965)). All of the above authors obtained explicit solutions for near tip stresses in particular two-dimensional fracture problems. After the time of these initial investigations the study of bimaterial fracture subsided somewhat. A renewed interest was developed recently, stemming from the increased use of composite materials in engineering applications, and the problem of interfacial fracture was revisited. A recent noteworthy contribution is that of Rice (1988), who gives a detailed analysis of linear elastic interfacial fracture mechanics using the method of Muskhelishvilli potentials. A summary of the results of Williams (1959) and Rice (1988) is given in the following section. (For a review of elasticity and plasticity aspects of interfacial fracture also see Shih (1991)).

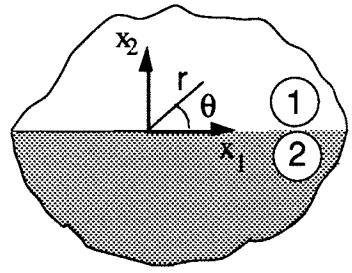

Figure 1: Geometry of interfacial crack problem.

1.2.1 Static interfacial crack-tip fields

Consider the two-dimensional problem of a semi-infinite traction free crack lying along an interface between two linearly elastic, isotropic and homogeneous materials, as shown in figure 1. As shown by Dundurs (1969) the solution to such a problem can only depend on two dimensionless combinations of the elastic moduli of the materials. These are called the Dundurs parameters and are given by,

$$\alpha = \frac{\mu_1(\kappa_2 + 1) - \mu_2(\kappa_1 + 1)}{\mu_1(\kappa_2 + 1) + \mu_2(\kappa_1 + 1)} \quad \text{and} \quad \beta = \frac{\mu_1(\kappa_2 - 1) - \mu_2(\kappa_1 - 1)}{\mu_1(\kappa_2 + 1) + \mu_2(\kappa_1 + 1)}, \tag{1.1}$$

where μ is the shear modulus and $\kappa=3-4\nu$ for plane strain conditions and $(3-\nu)/(1+\nu)$ for plane stress conditions, with ν the Poisson's ratio of the material. Subscripts 1 and 2 refer to the material above and below the interface respectively.

The complete structure of the asymptotic in-plane stress field surrounding the crack is given by Shih (1991),

$$\sigma_{\alpha\beta} = \frac{1}{\sqrt{2\pi r}}\left\{Re\left[Kr^{i\varepsilon}\right]f^{I}_{\alpha\beta}(r,\theta) + Im\left[Kr^{i\varepsilon}\right]f^{II}_{\alpha\beta}(r,\theta)\right\}, \tag{1.2}$$

where $\alpha, \beta=1, 2$. Throughout this work we adopt the usual convention of indicial notation in which a repeated index denotes a sum. Greek indices take the values of 1, 2 and Roman indices of 1, 2, 3. In expression (1.2) K is called the complex stress intensity factor and is given by $K = K_1 + iK_2$, r, θ are spatial coordinates, and $f^{I,II}$ are known functions of r and θ. These functions are explicitly stated in Symington (1987). The tractions ahead of the interface can be expressed as,

$$\sigma_{22} + i\sigma_{12} = \frac{K}{\sqrt{2\pi r}}\left(\frac{r}{L}\right)^{i\varepsilon}, \tag{1.3}$$

where L is a normalizing length scale. The quantity ε is called the (quasi-static) oscillatory index and is related to the Dundurs parameter β through,

$$\varepsilon = \frac{1}{2\pi} ln\left(\frac{1-\beta}{1+\beta}\right). \tag{1.4}$$

From equation (1.3) it is clear that oscillatory stresses of the order of $r^{-1/2+i\varepsilon}$ are predicted ahead of the crack tip. In addition, this solution predicts interpenetration of the crack faces behind the tip, thus violating the assumption of traction free crack faces. The

extent of the contact zone, r_c, is defined in Rice (1988) as the maximum distance behind the crack tip at which the crack face opening displacement becomes zero. This is given by,

$$r_c = e^{\frac{-\pi/2-\phi+\tan^{-1}(2\varepsilon)}{\varepsilon}}. \tag{1.5}$$

In the above equation ϕ is called the phase angle and is defined as

$$\phi = \tan^{-1}\left\{\frac{Im\left(KL^{i\varepsilon}\right)}{Re\left(KL^{i\varepsilon}\right)}\right\}. \tag{1.6}$$

Any length L can be used as a scale in a particular problem, even though usually a characteristic length of the problem is chosen (e.g., crack length, thickness etc.). It is clear from (1.3) and (1.6) that the phase angles corresponding to two different length scales L_1 and L_2 can be related by

$$\phi_2 - \phi_1 = \varepsilon \ln\left(\frac{L_2}{L_1}\right). \tag{1.7}$$

Thus a change in length scale denotes a shift in the phase angle ϕ.

A final quantity of interest in the present study is the energy release rate G. This is given by

$$G = \frac{F}{4\mu_1}|K|^2, \tag{1.8}$$

where F is a function of material properties of the two constituents of the interface (see Rice (1988)).

The solution described above has certain inconsistencies that have often led researchers to question its validity entirely. The oscillatory behavior of the stresses ahead of the crack tip is physically unacceptable. Also unacceptable, within the framework of the initial boundary value problem, is the predicted interpenetration of the crack faces. This clearly violates the assumptions of traction free crack faces under which the solution was derived. In the work by Comninou (1977a) a model involving frictionless contact behind the crack tip was proposed. This indeed eliminated the presence of interpenetration, but led to a surprising result, namely that under purely tensile remote loading, the interface crack has zero K_1 and non-zero K_2. Other studies involving contact are also found in the work of Comninou (1977b), Gautsen and Dundurs (1987) and Gautsen and Dundurs (1988).A different approach that eliminated both the oscillatory stresses ahead and the contact behind the crack tip was presented by Knowles and Sternberg (1983). To eliminate these problems, a neo-Hookean behavior of the elastic constituents of the interface was assumed. This shows that the above mentioned pathologies are indeed an artifact of linear elasticity theory. Similar conclusions were reached in recent analytical work by Geubelle and Knauss (1992a), Geubelle and Knauss (1992b) when modeling interfaces between generalized neo-Hookean materials. Nevertheless, the linear elastic solution has some merit, primarily because of its simplicity, and should not be completely discarded. It may be used in experimental analysis if one invokes a small scale contact criterion as described in detail in Rice (1988) and Shih (1991). If there is a substantial region over which equation (1.2) is valid (called a K-dominance region) and if the contact zone size (given by equation (1.5)) is very small compared to all other dimensions involved in the problem and is completely embedded within the K-dominance region, then the complex stress intensity factor K can be used as a parameter controlling the stress field surrounding the crack (Ravichandran and Knauss (1989) and Geubelle and Knauss (1991)). It is clear at this point that the stress field surrounding an interfacial crack, *under small scale contact conditions*, can be

characterized by two fracture parameters, namely K_1, K_2 (or G, ϕ) with an appropriate length scale.

1.2.2 Quasi-static interfacial crack initiation and growth

Quasi-static crack initiation and propagation in homogeneous solids are well understood after extensive research on the subject spanning several decades. Criteria proposed for crack initiation and growth in homogeneous solids are those of critical opening stress (Erdogan and Sih (1963)), critical energy release rate (Griffith (1921)), critical crack opening displacement (Wells (1961), Wells (1963)) and critical crack opening angle (Shih et al. (1979)). In all cases propagation occurs at a phase angle $\phi = tan^{-1}(K_{II}/K_I) = 0$, but initiation need not. An angle of $\phi=0$ corresponds to a pure mode I (opening mode) condition. Crack growth at $\phi=0$ has also been observed experimentally in homogeneous materials. A complication arises though for interfacial crack tip fields. In general all stress components ahead of an interfacial crack contain coupled symmetric and antisymmetric spatial variations. So a mode separation, as performed in homogeneous fracture, is not possible in bimaterial fracture. Both fracture parameters describing the bimaterial field must be involved in the development of any initiation or quasi-static crack growth criterion. Such a criterion for crack initiation has been proposed by Liechti as a dependence of G_c on ϕ_c of the type shown in figure 2. Using an optical method developed during the work of Liechti and Knauss (1982a)and Liechti and Knauss (1982b) he provided experimental verification of such a dependence (Liechti and Chai (1991), Liechti and Chai (1992)). Other experimental results pointing to this end have been provided by Foltyn and Ravichandar (1993), Hutchinson (1989), O'Dowd et al. (1992), and Wang and Suo (1990). From figure 2 we see that there is a minimum in the value of the energy released during crack propagation, but this quickly increases around certain phase angles, which essentially correspond to a large amount of "shearing" around the crack tip. A larger amount of energy has to be provided to grow the crack tip when it is in a state of "high

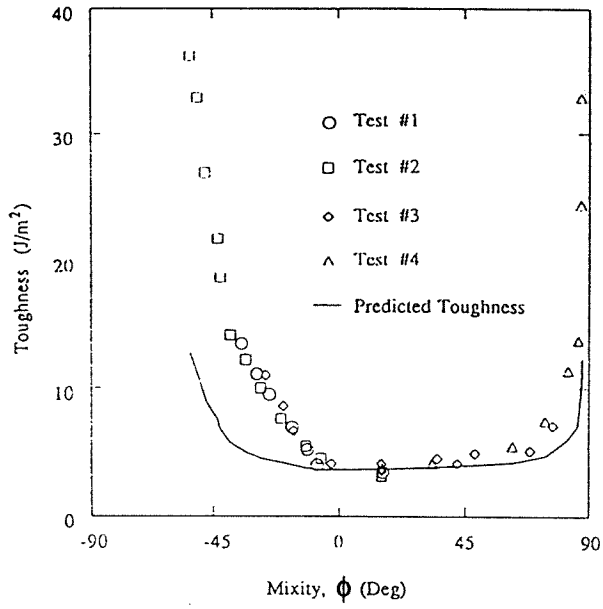

Figure 2: Quasi-static interfacial toughness of glass/epoxy system (from Liechti and Chai (1992)).

shear." The (G,ϕ) crack initiation criterion observed by the above researchers is now well established and is widely believed to indeed control the (macroscopic) quasi-static failure of interfaces.

A relation of G and ϕ of the type shown in figure 2 is also believed to be the condition for *dynamic initiation* of interface cracks with the appropriate dynamic values for energy release rate and phase angle. Although some experimental work has been done on the subject of quasi-static interfacial fracture, very little has been done on dynamic interface fracture. No experimental data exists to corroborate this dynamic initiation model. Nevertheless, when comparing with the case of homogeneous materials where the steady state value of the quasi-static fracture toughness is usually also the value of the dynamic initiation fracture toughness, then the above criterion also seems feasible. In chapter 4 of the current work we shall propose a criterion for dynamic crack growth of an interface crack. This growth criterion will be consistent with an *initiation* criterion of the type mentioned above based on G and ϕ.

CHAPTER 2

EXPERIMENTAL PROCEDURES

In the present study it was intended to experimentally investigate, in real time, the stress field around the tip of a dynamically propagating interfacial crack. A reliable, full-field optical technique was needed, that was also capable of real time imaging when used in conjunction with a high speed camera set up. The method chosen was the lateral shearing interferometer of Coherent Gradient Sensing (CGS). This is an interferometer recently developed by Tippur et al. (1991). A brief description of the optical method and its application to the bimaterial problem are given in the next section.

2.1 Coherent Gradient Sensing interferometer (CGS)

The method of CGS for use in mechanics was first proposed by Tippur et al. (1991) and is described in detail by Rosakis (1993). The set-up of the method in a transmission configuration for the case of a dynamically loaded bimaterial specimen is shown schematically in figure 3. A coherent, monochromatic, collimated laser beam is incident on the deforming specimen. After transmission through the specimen it acquires an optical path difference and looses collimation. The resulting, now non-collimated, beam passes through two line diffraction gratings G_1 and G_2 of fine pitch p (typically 40 lines/mm). They are situated a distance Δ apart and perform a shearing of the incident wave front as described below. The gratings' output intensity is transmitted through a filtering lens L. A diffraction spot pattern is obtained on the filtering plane, which is located at the back focal plane of the lens L. At this plane all but one diffraction orders are blocked. The

one remaining diffraction spot (either of ±1 orders), shown in figure 3 as the open circle on the filtering plane, is imaged to produce an interference pattern. For the case of a dynamic

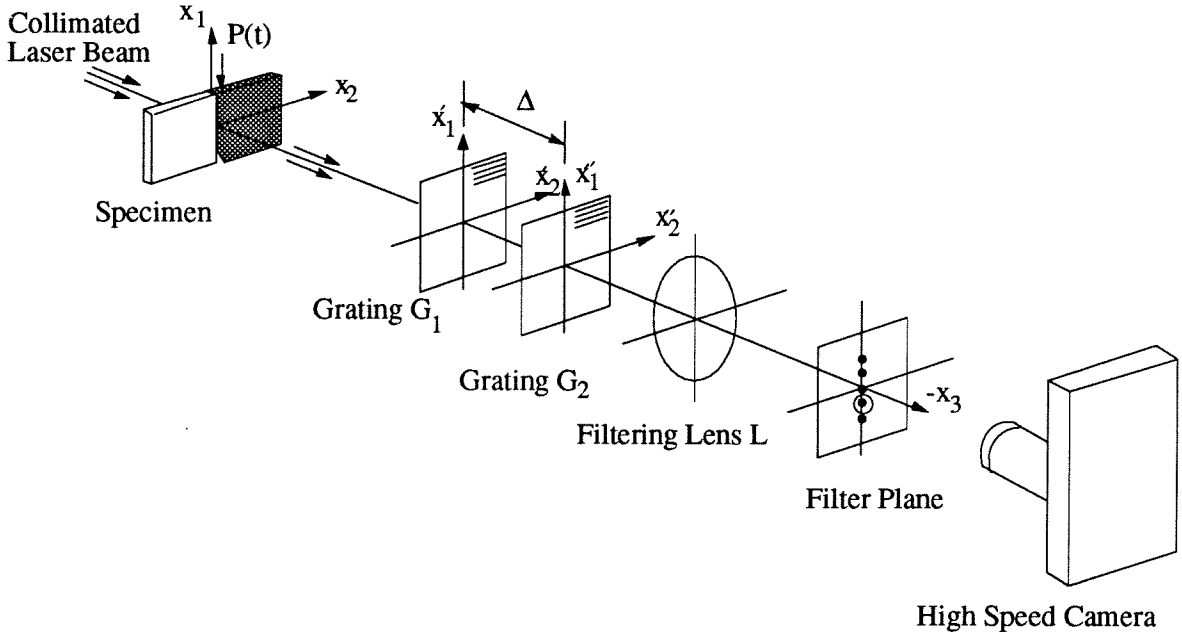

Figure 3: Schematic of CGS set-up in transmission.

experiment the imaging medium is a high speed camera focused on the specimen.

For the sake of simplicity and clarity the procedure used to analyze the above interferometer will follow the line of Murty (1964). This is the simple shearing analysis usually performed for lateral shearing interferometers. A more rigorous analysis using Fourier optics, which yields the same results as the current method, can be found in Tippur (1992) and Lee et al. (1993). The working principle of CGS is illustrated in figure 4. Without losing generality, the line gratings are assumed to have a sinusoidal transmittance. A plane wave propagating along the optical axis will be diffracted into three wavefronts E_0 and $E_{\pm 1}$ by grating G_1. The angle between the propagation directions of E_0 and $E_{\pm 1}$ is given by the diffraction equation

$$\theta = sin^{-1}\left(\frac{\lambda}{p}\right) \approx \frac{\lambda}{p}, \tag{2.1}$$

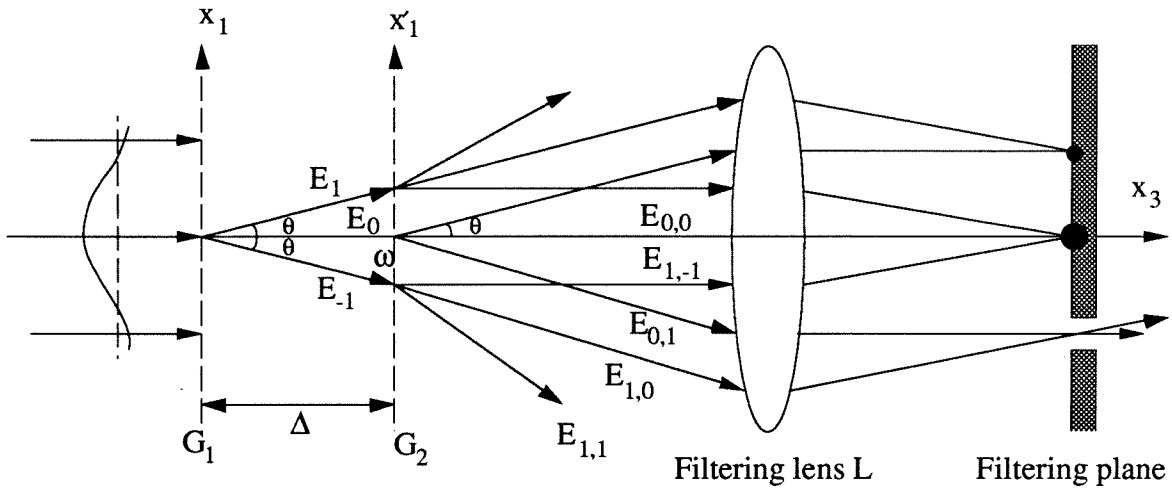

Figure 4: Working principle of CGS interferometer.

where λ is the wavelength of light and p the grating pitch. (The value of λ used in all dynamic experiments is 514 nm and of p 0.0254mm (40 lines/mm). These correspond to a diffraction angle of about 1.2°). The second grating G_2 will diffract each wave front emerging from G_1 into three additional wavefronts. Thus nine wavefronts will emerge from the second grating. Each of these is traveling in distinctly different directions, some of which are parallel. Wavefronts having parallel directions of propagation are then brought to focus on the back focal plane of lens L, forming a set of diffraction spots. Of these, only the +1 or -1 orders are allowed through to the image plane. In figure 4 the -1 order has been allowed through.

Now consider a distorted wavefront emerging from the deforming specimen. Mathematically this is represented as having a phase (or optical path) change $S(x_1,x_2)$ that is dependent upon the local specimen deformation. In figure 4 this is shown as a curved line incident on G_1. If a large portion of such a bundle of light has rays nearly parallel to

the optical axis, then when it passes through the interferometer, the diffraction spots on the filtering plane will be locally surrounded by a small halo of light. If, as is shown in figure 4, we allow the -1 spot through, then an interference pattern caused by the superposition of the two wavefronts traveling along the parallel directions $E_{0,1}$ and $E_{1,0}$ will be visible on the image plane. The resulting image would consist of a superposition of the original wavefront with itself, after being sheared (displaced) by an amount approximately equal to ω. This distance is given by

$$\omega = \Delta \tan\theta \approx \Delta\theta, \tag{2.2}$$

for small θ.

The condition for constructive interference of $E_{0,1}$ and $E_{1,0}$ on the image plane of the camera is

$$S(x_1 + \omega, x_2) - S(x_1, x_2) = m\lambda, \tag{2.3}$$

where m=0,±1,±2,... . By dividing both sides of (2.3) with ω and substituting for ω and θ from (2.1) and (2.2) we obtain,

$$\frac{S(x_1 + \omega, x_2) - S(x_1, x_2)}{\omega} = \frac{mp}{\Delta}. \tag{2.4}$$

If now we let $\omega \to 0$, which essentially means moving the two diffraction gratings closer together (i.e., $\Delta \to 0$) or increasing the grating pitch (i.e., $p \to \infty$), then the condition for interference on the image plane becomes,

$$\frac{\partial(S(x_1, x_2))}{\partial x_1} = \frac{mp}{\Delta}, \qquad m = 0, \pm 1, \pm 2, \ldots . \tag{2.5}$$

If the grating lines are parallel to the x_1 direction then in a similar fashion it can be shown that the condition for constructive interference becomes

$$\frac{\partial\left(S(x_1,x_2)\right)}{\partial x_2}=\frac{np}{\Delta}, \qquad n=0,\pm1,\pm2,\ldots \ . \tag{2.6}$$

For solid mechanics applications, it is desirable to relate the quantity $S(x_1,x_2)$ to the stress state in the deforming specimen. Consider a planar wavefront normally incident on an optically and mechanically isotropic, transparent plate of initial uniform thickness h and refractive index n. In our case this would be the test specimen whose centerplane, as shown in figure 3, lies in the (x_1, x_2) plane. When it undergoes any kind of deformation (static or dynamic), the transmitted wavefront will be expressed as $x_3+S(x_1, x_2)=const$, where $S(x_1, x_2)$ is the optical path change acquired during refraction. As discussed in detail by Rosakis (1993), $S(x_1, x_2)$ is related to the deformation state by the relation,

$$S(x_1,x_2)=2h(n-1)\int_0^{1/2}\varepsilon_{33}d\left(x_3/h\right)+2h\int_0^{1/2}\delta n d\left(x_3/h\right). \tag{2.7}$$

The first term of equation (2.7) represents the net optical path difference due to the plate thickness change caused by the strain component ε_{33}. The second term is due to the stress induced change of refractive index of the material. This change in the refractive index δn is given by the stress optical relation (Maxwell relation),

$$\delta n=D_1\left(\sigma_{11}+\sigma_{22}+\sigma_{33}\right), \tag{2.8}$$

where D_1 is the stress optic coefficient and σ_{ij} are Cartesian components of the stress tensor. The above relation is strictly true for isotropic linear elastic solids. For such solids the strain component ε_{33} can also be related to the stress and equation (2.7) then becomes

$$S(x_1,x_2) = 2hc_\sigma \int_0^{1/2} \left\{ (\sigma_{11}+\sigma_{22}) \left[1 - D_2 \left(\frac{\sigma_{33}}{\nu(\sigma_{11}+\sigma_{22})} \right) \right] \right\} d(x_3/h), \tag{2.9}$$

where

$$c_\sigma = \left[D_1 - \frac{\nu}{E}(n-1) \right], \qquad D_2 = -\left[\frac{\nu D_1 + \dfrac{\nu(n-1)}{E}}{D_1 \dfrac{\nu(n-1)}{E}} \right].$$

E, ν and c_σ are the Young's modulus, Poisson's ratio and the stress optical coefficient of the material respectively.

2.1.1 Effects of three dimensionality on data analysis

The discussion of the previous section was intentionally kept as general as possible within the assumptions of isotropic linear elasticity. For either a homogeneous or a bimaterial cracked linear elastic plate of uniform thickness and finite in-plane dimensions, the optical path difference S acquired by light transmission through the specimen thickness, will in general depend on the details of the three-dimensional elastostatic or elastodynamic stress state that would exist at the vicinity of the crack tip. It will be a function of the applied loading, as well as of the in-plane dimensions and thickness of the specimen. For bimaterial systems it is also expected to depend on the material mismatch.

Given the lack of full-field, three-dimensional analytical solutions in fracture mechanics, experimental information can strictly be extracted by means of detailed numerical calculations. Nevertheless there exist certain non-trivial special cases for which

available asymptotic solutions, based on two-dimensional analyses, may provide adequate approximations for $S(x_1,x_2)$ at certain regions near the crack tip. In particular, it has been argued that conditions of plane stress will dominate in thin, *homogeneous* cracked plates at distances from the crack front larger than half the specimen thickness. This would imply that if only interference fringes outside the three-dimensional zone are analyzed the results could be interpreted on the basis of a plane stress analysis (see Rosakis and Ravi-Chandar (1986) and Rosakis (1993)).

To illustrate the extent of the near tip three dimensionality, reference is made to figure 5 which shows a three-dimensional representation of the ratio $\sigma_{33}/\nu(\sigma_{11}+\sigma_{22})$ for a precracked three point bend specimen of a *homogeneous* material. This is the same quantity that appears in the second term of the integrand of the optical path change relation, equation (2.9). The above ratio is often called the degree of plane strain. It is a measure of near tip three dimensionality and has been obtained by means of a three-dimensional finite element calculation which models a stationary crack in a three point bend specimen subjected to dynamic loading. In regions where the deformation is locally plane stress, this measure equals zero (i.e., $\sigma_{33}=0$). When the deformation approaches plane strain like conditions the ratio approaches 1 (i.e., $\sigma_{33}=\nu(\sigma_{11}+\sigma_{22})$). In figure 5 only one half of the specimen thickness is shown. The top surface visible in the figure corresponds to the mid-plane of the specimen. The traction free crack surface is on the left-hand side of the picture. The maximum extent of the three-dimensional zone is approximately 0.4-0.5h, ($\theta=0°$), whereas at $\theta\approx120°$, the plane stress approximation is adequate much closer to the crack tip, down to $0.1h$. For more details on the issue of three-dimensional near tip deformations in a homogeneous cracked plate see Krishnaswamy et al. (1991).

For bimaterial specimens an equivalent numerical calculation can be made. Figure 6 provides the same three-dimensional view of the contours of the ratio $\sigma_{33}/\nu(\sigma_{11}+\sigma_{22})$ for a PMMA/aluminum bimaterial system (PMMA is Poly-Methylmethacrylate). This is one of the bimaterial combinations that has been used in the experimentation of dynamic interface

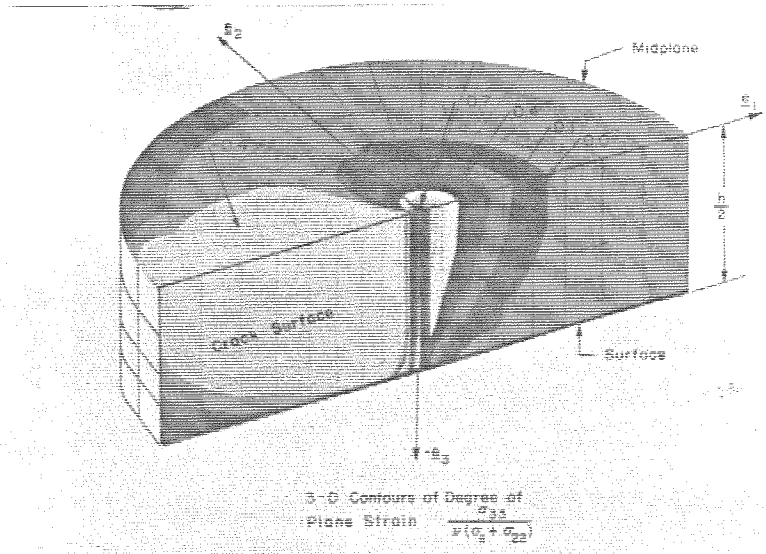

Figure 5: Contours of numerically calculated degree of plane strain in a dynamically loaded homogeneous cracked plate (from Krishnaswamy et al. (1991)).

fracture presented in this work. (Details of the specimen preparation and experimental procedures are described in the two next sections). In figure 6 only the PMMA side of the bond is visible. This is of course the side relevant for the analysis of transmission CGS patterns since PMMA is transparent. As is obvious from a comparison of figures 5 and 6, the nature of the three dimensional deformation in bimaterials is different than that of homogeneous systems. In the bimaterial case there is a large three dimensional region, of width of approximately half the specimen thickness, that extends along the bond line. Unlike the homogeneous case, there exists no plane stress region at any visible distance ahead of the crack tip. However, there exists a wedge of plane stress conditions defined by $100°<\theta<150°$ and down to $r<0.2h$. (For more details on the numerical analysis leading to this result see Lee and Rosakis (1992)). Note that there exist other numerical analyses of three dimensional effects around interfacial cracks, most notably that of Nakamura (1991). Although his results are qualitatively similar to those above, they are not directly relevant to

this particular study because of the different geometry used and, more importantly, because the mismatch parameter ε in his case was assumed to be zero.

We can now use the results of the numerical computation when interpreting optical patterns using relation (2.9). If we choose to analyze only points outside the three-dimensional region, in the region of plane stress conditions, then the optical path difference S in (2.9) will simplify to

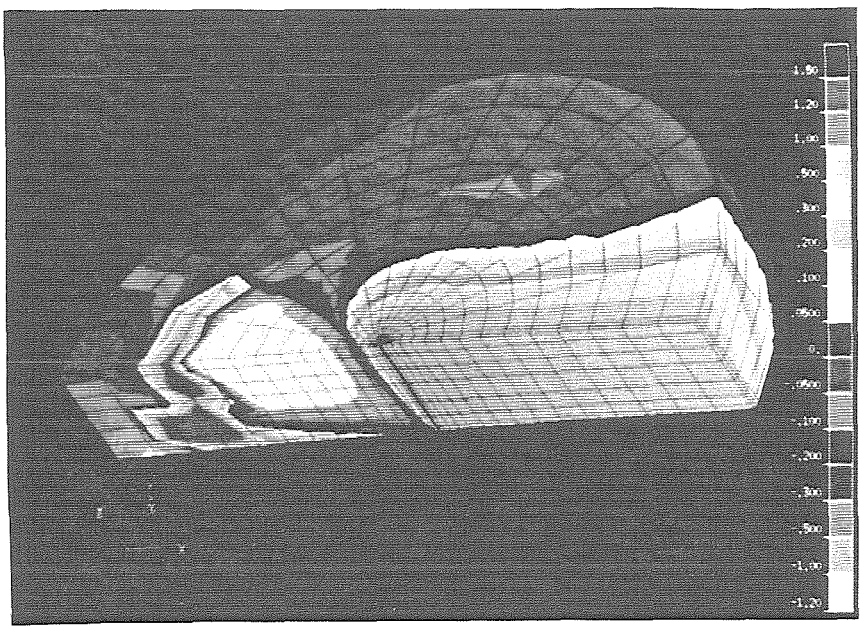

Figure 6: Contours of numerically calculated degree of plane strain in a dynamically loaded bimaterial cracked plate.

$$S(x_1,x_2) \approx c_\sigma h\left[\hat{\sigma}_{11}(x_1,x_2)+\hat{\sigma}_{22}(x_1,x_2)\right], \tag{2.10}$$

where $\hat{\sigma}_{11}$ and $\hat{\sigma}_{22}$ are *thickness averages* of the in-plane stress components in the plate.

Thus for points outside the near-tip three-dimensional region the CGS patterns assume a simple interpretation in terms of two-dimensional stress field approximations. In particular, equations (2.5) and (2.6) in conjunction with equation (2.10) now indicate that

the fringes obtained from regions surrounding the three-dimensional zone can be related to the in-plane gradients of $\hat{\sigma}_{11}+\hat{\sigma}_{22}$ as follows

$$c_\sigma h\frac{\partial(\hat{\sigma}_{11}+\hat{\sigma}_{22})}{\partial x_1}=\frac{mp}{\Delta}, \qquad c_\sigma h\frac{\partial(\hat{\sigma}_{11}+\hat{\sigma}_{22})}{\partial x_2}=\frac{np}{\Delta}, \qquad m,n=0,\pm1,\pm2,\ldots, \tag{2.11}$$

where in the case of transmission c_σ is the stress optical coefficient of PMMA.

2.2 Bimaterial experiments

In order to intensify the dynamic effects at the interface, it was decided to use bimaterial constituents that had a very large mechanical property mismatch. This would allow us to investigate easier the more extreme cases of interfacial behavior. In addition, it approximates closely the type of extreme elastic property mismatch occurring in composite materials which often utilize the strengthening effects of a very stiff fiber embedded in a very compliant matrix. To be able to use a transmission CGS arrangement in our experimentation, one side of the bond, the more compliant side, was chosen to be Plexiglas (Poly-Methylmethacrylate or PMMA). This is a transparent polymer that is easily machined and handled. At room temperature it behaves in a brittle fashion. The other side of the bond was chosen as either 6061-T6 aluminum or AISI 4340 steel, both of which are considerably stiffer and tougher than Plexiglas. Throughout this study, the PMMA side of each specimen will be referred to as material-1 and the metal side as material-2. So with reference to figure 1, the more compliant material occupies the positive x_2 plane.

The mechanical properties of the constituents are shown in table 1. These were measured in the laboratory using an ultrasound technique and were cross-referenced from data available in the literature (Beinert and Kalthoff (1981) and General (1989)). Table 1 also shows the value of the plane stress quasi-static oscillatory index, defined by equation (1.4), for the bimaterial combinations of PMMA/aluminum ($\varepsilon^{P/A}$) and PMMA/steel ($\varepsilon^{P/S}$).

Also shown is the value of $\varepsilon^{P/R}$ for Plexiglas bonded to a rigid substrate. As can be seen, these three values are extremely close. This would suggest that we can expect intense interfacial effects during the dynamic fracture event. It also suggests that the approach of some researchers (Hutchinson (1989), Nakamura (1991)) to set ε=0 invoking small material mismatch cannot be applied in our case.

PROPERTY	PMMA	6061-T6 Aluminum	AISI 4340 Steel
E (GPa)	3.24	80	208
ν	0.35	0.33	0.3
c_d (m/s)	2080	6600	5970
c_s (m/s)	1000	3330	3190
c_R (m/s)	935	3100	2950
ρ (Kg/m^3)	1190	2710	7830
$\varepsilon^{P/A} = 0.0981$	$\varepsilon^{P/S} = 0.1037$	$\varepsilon^{P/R} = 0.1073$	

Table 1: Mechanical properties of interface constituents.

One of the most critical parameters influencing the behavior of any bimaterial system is the bonding procedure and eventual bond strength. A detailed analysis of the bonding procedure used in this study is provided in the next section.

2.2.1 Bimaterial specimen preparation

The specimen preparation procedure follows the lines of Tippur and Rosakis (1991). Although some modifications have been made here, the main bonding method remains the same. The PMMA and metal sides of the bond are plates of nominally equal thickness of 9mm. Both are machined to have flat and square edges to allow for accurate bonding. The adhesive used is a commercially available product that consists of two components; a Methylmethacrylate monomer (MMA), compound A, and a catalyst,

compound B, which can polymerize the monomer. Details of the constituents of the adhesive are given in table 2. The bonding process essentially follows the manufacturers instructions. Each side to be bonded is roughened by sandblasting with 10-20μm sized glass beads. Both surfaces are then thoroughly cleaned before bonding. The adhesive is prepared from a mixture of 100 parts (by weight) MMA and 13 parts catalyst. A thin layer of the adhesive mixture is then applied on the metal face of the bond and held against the PMMA side. Two metallic clamps are used to keep the two constituents in place. A uniform pressure is then applied. The bond is cured to peak strength at room temperature for 24 hours. The result is a bimaterial specimen of PMMA bonded to aluminum or steel. The bond thickness is estimated to be about 100μm (Tippur and Rosakis (1991)).

Compound A	**Compound B**
Methylmethacrylate Monomer	Traces of Benzoyl Peroxide (catalyst)
Traces of titanium dioxide (dye)	Methyl Ethyl Ketone (solvent)
Traces of acrylic synthetic resin	

Table 2: Adhesive constituents.

Because of the complexity of the interfacial crack problem, most theoretical studies available are for two materials, perfectly bonded along a straight line interface. The particular adhesive described above was used in an attempt to avoid introducing a third material into the system. The elastic properties of the adhesive after polymerization are almost identical to those of material-1 (PMMA). This allows use of the *bimaterial* solutions in the analysis of experimental data. Of course locally the interface profile will have a roughened profile. The roughened bond surfaces provide a mechanical bond between the two constituents. Macroscopically though, the bond line approximates as well as possible a straight bimaterial interface. Nevertheless, possible problems arising from this issue are further discussed in section 2.3.

The crucial issue of bond strength has been addressed by the performance of bond calibration tests by Tippur and Rosakis (1991). For the specimen to be able to well simulate a theoretically perfect bond, the toughness of the interface must be *at least* as much as that of homogeneous Plexiglas, the more compliant of the two constituents. If not, the interface would become a favorable path for crack growth and experimental results would be biased. The bond calibration tests of Tippur and Rosakis (1991) essentially consist of a static test to measure the fracture toughness of a specimen made up of two halves of PMMA bonded together using the procedure described above. It was shown that the fracture toughness of the bonded PMMA specimens was over 95% of that of homogeneous PMMA. Indeed we see that the adopted bonding procedure results in a glue material whose stiffness and toughness characteristics are almost exactly those of PMMA. Additional quasi-static crack growth tests in PMMA/steel three point bend edge cracked plates were performed in the context of this work. In those experiments it was seen that the measured *quasi-static* initiation toughness was about 1.1MPa$\sqrt{m}$. This value is also over 95% of the toughness of homogeneous PMMA. This testifies that the toughness between the PMMA and steel bond is at least as much as that of homogeneous PMMA. (These facts were also claimed to be true by the adhesive manufacturer. Nevertheless the above mentioned tests were performed to check the validity of their claims).

In the experiments described in the next two sections, bimaterial fracture specimens containing either a blunt notch or a sharp pre-crack along the interface were used. After being bonded using the procedure described above, to create a starter notch in a specimen use of a band saw was made. In all cases the notch was cut along the interface. Care was taken to cut equally into the PMMA and metal sides of the bond. A slow cut speed insured no or very little residual stresses in the PMMA. The length of the starter notch in all cases was 25mm. The width of the notch, which was dictated by the width of the band saw blade, was approximately 750μm.

In some experiments, a sharp pre-crack was used. It was introduced by covering part of the bond surface, the prospective crack face, with grease so as to stop the bonding action of the glue. Unfortunately it was seen that after curing the crack front was not very well defined. There was a mixture of adhesive and lubricant around the, not very straight, crack front. To ensure that the crack front was straight and far removed from the region of initial bonding, it was stably grown in a quasi-static fashion. A displacement controlled Instron machine was used to grow the crack 2-3mm along the interface. In the process a CGS interferometer was set up in front of the specimen to monitor crack growth. Using the interferometer it was possible to observe the stability of crack growth and verify that the crack front was indeed a straight line through the thickness. The latter is possible in a transmission arrangement because if a slanted crack front forms, then two crack tips are clearly visible on the image plane. In the case that a specimen had a slanted crack front it was discarded. A verification of how straight the crack front was, was obtained by visually inspecting the eventual fracture surfaces at the end of each dynamic test. Clearly visible distinct marks showed the position of the crack tip after initially bonding and subsequently growing the crack quasi-statically. An illustration of a CGS fringe pattern from a quasi-static PMMA/steel three point bend experiment is shown in figure 7. Fringes, which represent contours of the gradient of the trace of in-plane stresses, are visible only on the PMMA side of the bond. The crack tip is located at the position where the fringes meet the interface.

Initially it was feared that the static loading and unloading of the specimen would cause damage to accumulate near the initial crack tip along the interface. This could affect the results of subsequent dynamic initiation tests since the new crack would now be initiating along a weakened bond line. It was decided therefore to recalibrate the bond strength after a specimen had been statically loaded once. Two PMMA halves were bonded together in the fashion described in section 2.2.1 for the earlier calibration tests. A sharp crack was introduced along the interface as described above. The crack was then grown

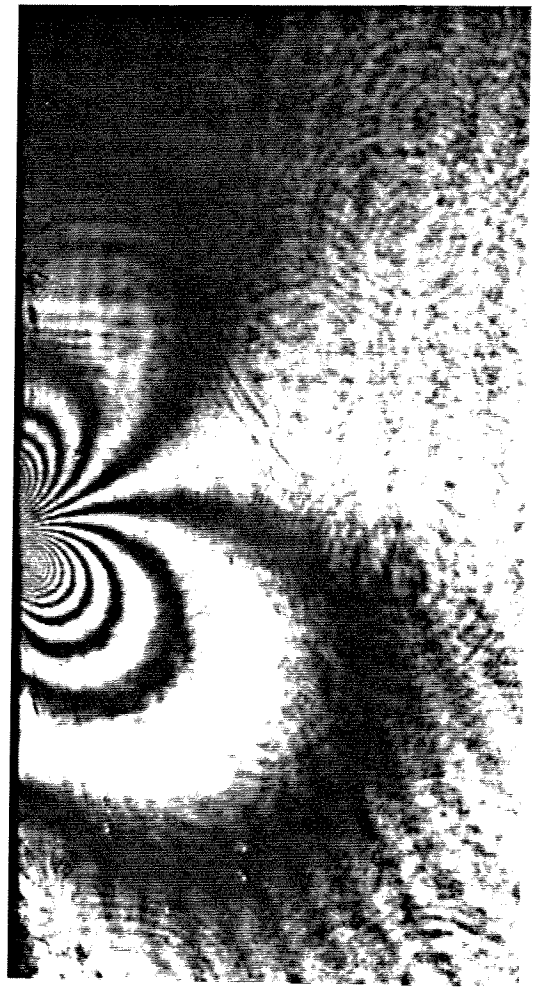

Figure 7: CGS fringe pattern obtained during quasi-static crack propagation along a bimaterial interface.

2mm quasi-statically and the specimen unloaded. It was then reloaded to failure and the new fracture toughness was recorded. Once again a fracture toughness in excess of 95% that of homogeneous PMMA was measured. This implies that even after the quasi-static crack growth procedure the bond still retains its strength. It also points to the fact that the adhesive used is essentially PMMA which is fairly brittle at room temperature.

2.2.2 Drop weight tower experiments

The first series of dynamic tests performed utilized a drop weight loading device to provide impact loading. The specimens used had a width of 127mm, a total length of 305mm and nominal thickness 9mm. A schematic of the specimen geometry is shown in figure 8, along with all relevant dimensions. Only specimens containing blunt starter notches were tested in this loading device. A notch length of 25mm was used so as to

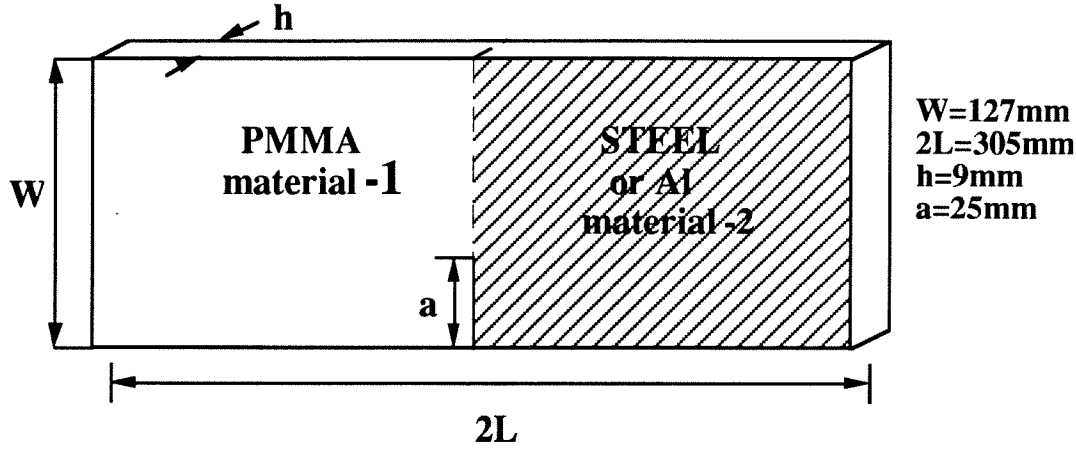

Figure 8: Specimen geometry and dimensions.

provide a crack to width ration (a/W) of 0.2. This ratio has been seen in the past to produce reliable results for homogeneous materials. In Tippur et al. (1991) and Lee and Rosakis (1992) it was shown that for a three point bend edge cracked plate with a/W of 0.2 a significant area of K-dominance was present around the crack tip.

The bimaterial specimens were impacted using a drop weight tower. This device is a model 8100-A Dynatup tower with a 200Kg free falling weight. This large mass funnels down to a rounded end (tup) with a radius of curvature of about 10mm. The loading on the specimen can thus be approximated as a dynamic line load across the specimen thickness. In two dimensions it may be simulated as a point load. The impactor tup is instrumented so as to provide a time history of the load applied on the specimen. This load history was recorded for each test on a digital oscilloscope (Nicolet model 4570) and kept for future use as an input boundary condition to a finite element simulation of each experiment. The

PMMA/steel or aluminum specimens are supported by resting them on two very thin glass slides in the manner shown in figure 9. These glass slides were found to be able to sustain

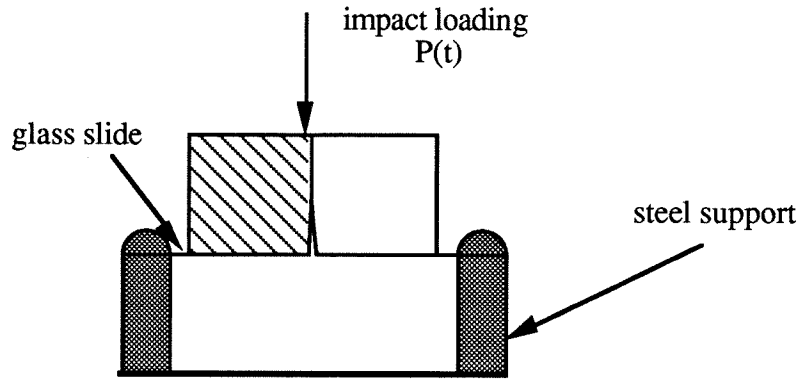

Figure 9: Specimen support using glass slides.

only about 20N of load in bending before they broke. This means that the bottom surface of the specimen can be considered essentially traction free throughout the event. A test of this kind, i.e., where one side of the specimen is impacted and the other is traction free, is often referred to as a dynamic one point bend experiment. This is to distinguish it from a three point bend test, where there are two supports on the side of the specimen opposite the side of impact.

True symmetric one or three point bend loading cannot be achieved dynamically since it is extremely difficult, if not impossible, to apply the impact load exactly on the interface, which is about 100μm thin. In addition, since the wave speeds of PMMA and steel (or aluminum) are vastly different (see table 1) the loading history at the crack tip would be completely different depending on which side of the bond line impact occurred. Having such an experimental uncertainty was unacceptable. Thus it was chosen to consistently impact the specimen a small distance (5mm) into the metal side of the bond. The reason we chose to impact the metal side is that at high loading rates Plexiglas tends to shatter around the impact point. At low loading rates though (impact speeds of 1-2m/s) one could perform experiments impacting the PMMA side. Because of time constraints this was

not done, but should be done in the future, if one wishes to acquire a complete understanding of the mechanics of dynamic decohesion of interfaces.

Figure 10 shows a schematic of the experimental set-up for the drop weight experiments. In all, except one, drop weight experiments the nominal impact velocity used was 4m/s. This would correspond to a relatively low loading rate at the crack tip. (By loading rate we mean the rate of increase of the stress intensity factor K. From subsequent analysis of experimental data, see chapter 3, we can quantify a low loading rate as being around 10^5MPa$\sqrt{m}$/s and a high loading rate as being over 10^6MPa$\sqrt{m}$/s). Intense stress waves generated by the impact and reflected from the specimen boundaries, load the notch tip up to crack initiation. The initiated crack tip propagates dynamically along the interface. The technique of CGS in transmission (described in section 2.1) was used in conjunction with high speed photography to record dynamic crack tip fields in a region approximately 50mm in diameter around the crack tip. This field of view is the size of the collimated beam transmitted through the PMMA half of the specimen. The light source used was a Spectra-Physics Argon-ion pulsed laser (model 166-09) operating at a wavelength of λ=514.5nm (green light). At this wavelength, the CW (continuous) power output of the laser is 2.5W. The beam emerging from the PMMA is processed by two diffraction gratings (see figure 10) located at a distance Δ=50mm apart. The gratings were provided by the Photosciences Co. (Torrance, CA). They are Ronchi line gratings on glass with a 40 line/mm ruling. This corresponds to a pitch p=0.0254mm. The angular sensitivity of the interferometer with these settings is 0.015°/fringe. Both gratings were anti-reflection coated to avoid light intensity loss and ghost images created by multiple reflections in the inter-grating distance Δ.

After emerging from the second grating, the light is collected by a high speed camera. Filtering of the -1 diffraction order occurs inside the camera by internal separation of the beams. The camera focuses the (undeformed) specimen surface onto the film track. The high speed camera is of the rotating mirror type (Cordin Co., model 330A). A rotating

mirror attached to a compressed air driven turbine shaft, reflects the image onto a film track which is on a stationary drum surrounding the mirror. The turbine shaft rotates at high speeds (~8000 rps) and the image is swept over the film track. Individual frames are obtained by operating the laser light source in a pulsed mode. High power, short duration pulses are produced the expose individual frames on the film track. The film exposure time is the duration of each pulse. The interframe time is the time between successive pulses. Because of the high propagation speeds involved in any dynamic crack growth experiment, a very short exposure time is needed to avoid image blurring. The exposure time used in all experiments was 30ns. A typical interframe time used (i.e., time between pulses) was 1.2μs (about 840,000 frames/s). At this pulse rate and duration, the peak power of each pulse is about 50W. Even so, because of the light losses in the optical components, very sensitive 35mm black and white film had to be used (Kodak TMAX-3200).

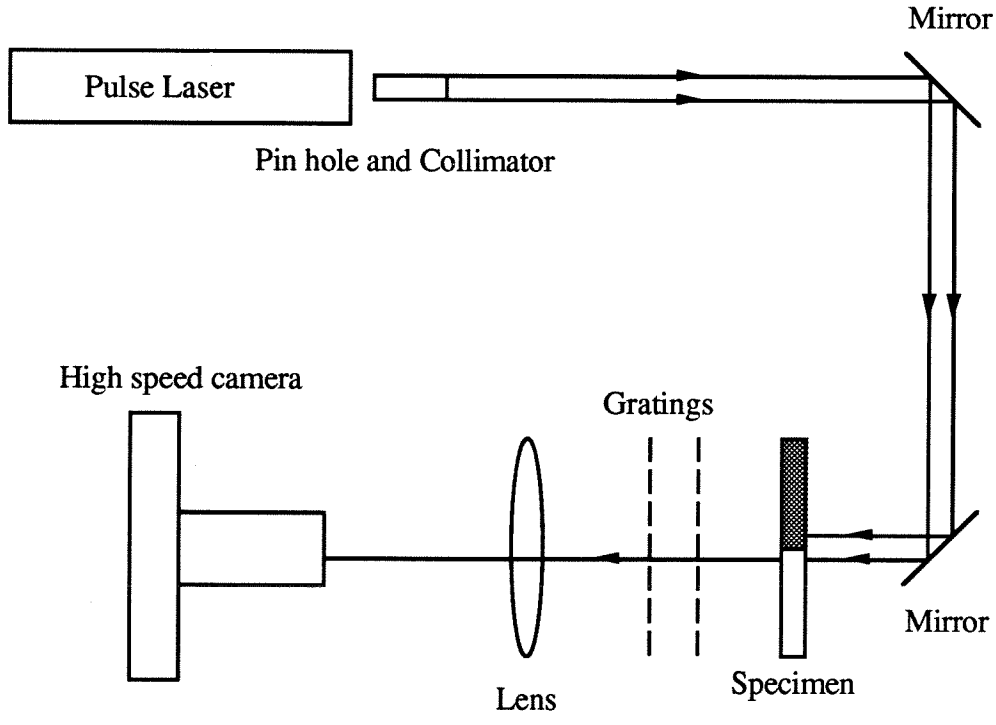

Figure 10 : Schematic of drop weight set up.

When running the camera at a framing rate of 1.2μs the total image recording time is about 95μs. This is because the total number of frames obtainable by this camera is 80. The time of 95μs is a very short window of observation. Therefore precise triggering of the laser is very important. A strain gauge placed on the specimen at the point of impact, senses the impacting tup. Its output is then delayed appropriately and the resulting signal is used to trigger the light source. The desired delay time was found after performing one test at a very low framing rate (i.e., a long interframe time) to determine the time of crack initiation. Subsequently the 95μs window can be shifted to observe either crack initiation or propagation behavior.

A typical sequence of selected interferograms from a drop weight tower test is shown in figure 11. These are from a PMMA/aluminum configuration impacted at 2m/s. Frames at 7μs intervals are shown. These particular interferograms, along with those from the remaining drop tower tests will be analyzed in detail in chapter 3 to obtain values of the near tip fracture parameters.

2.2.3 Gas gun experiments

In an attempt to drive the speed of crack propagation higher, for reasons that will become apparent later on in this thesis, it was decided to impact the bimaterial specimens using a high speed gas gun. Such a gun can produce higher loading rates than a drop weight device, even though it usually sustains the loading for a shorter time. Even so it is possible with a high enough loading rate to initiate the crack in a very short time period. The gas gun used in our experiments was manufactured in house. It is capable of firing a 75mm long, 50mm in diameter, steel projectile at speeds up to 100m/s. However, in all experiments presented in this work the impact velocity was 20m/s. The projectile velocity was measured by placing an LED at the exit of the gun barrel. The same optical technique and recording system as for the drop weight tower experiments were used. For a detailed discussion of these, refer to the immediately preceding section.

Figure 11: Sequence of CGS interferograms showing crack propagation along a PMMA/Al interface.

A schematic of the CGS set up, as used with a gas gun loading device, is shown in figure 12. A one point bend test is illustrated there. A series of such tests was performed,

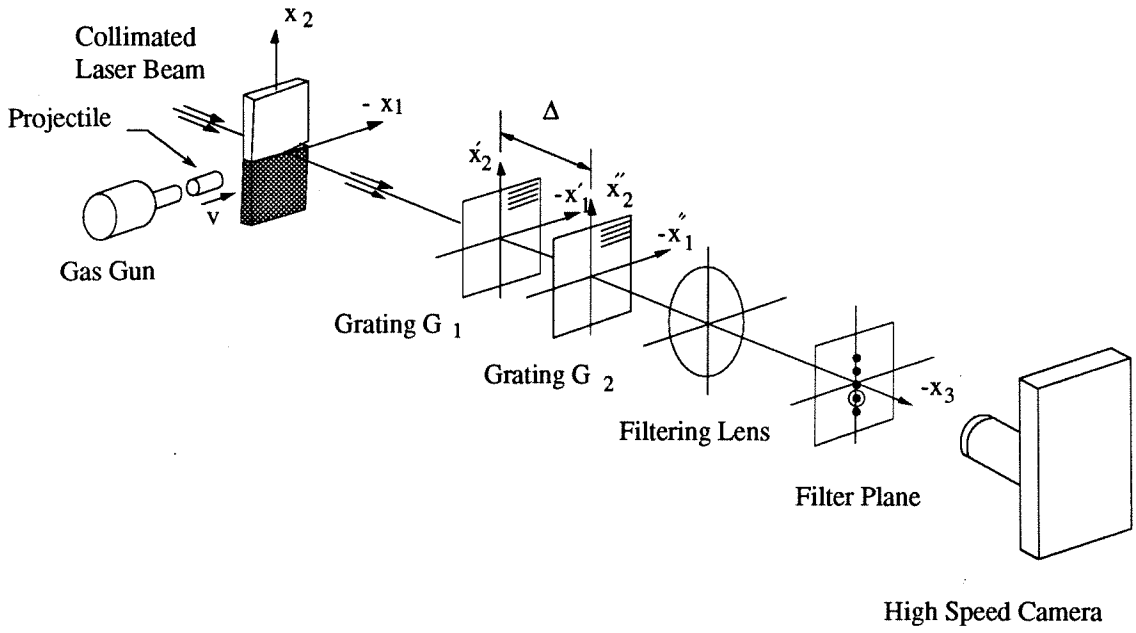

Figure 12 : Set-up CGS interferometer for air gun experiments.

during all of which the steel side was the one impacted, exactly as was the case in all drop weight experiments. In addition to the one point bend loading, two different loading geometries were used with air gun impact. All three loading configurations used in these tests are shown in figure 13. (Case (a) is the one point bend test). Each of these three geometries was tested while having either a starter notch (750μm wide) or a *sharp* starter crack. Overall therefore there were six types of tests conducted using gas gun loading ; three different geometries with two different types of starter defects. During all one point bend tests (type (a) in figure 13) the initial notch or crack present propagated dynamically along the interface. In all experiments utilizing geometries (b) or (c) though, the crack branched into the PMMA side of the bond. This occurred whether a thick notch or sharp crack were initially on the interface. No growth along the interface was observed in either case (b) or (c). Therefore no results on dynamic interfacial crack *growth* can be extracted from these experiments. Only conclusions regarding dynamic crack kinking can be drawn.

The crack kinking results are not discussed here since they are not directly relevant to the goals of the current study, i.e., the investigation of dynamic crack growth along bimaterial interfaces. In any case the fact that under certain dynamic loading conditions the starter crack initiates into the PMMA is an additional testimony to the strength of the bond. This fact becomes important in the discussion of some dynamic effects presented in subsequent chapters.

A typical sequence of interferograms resulting from a one point bend air gun test is shown in figure 14. Again only the PMMA side of the specimen produces fringes since it is transparent. A detailed qualitative and quantitative analysis of the fringe patterns will be made in the next chapter. Their similarities and differences with patterns obtained from drop weight tower tests will also be discussed there.

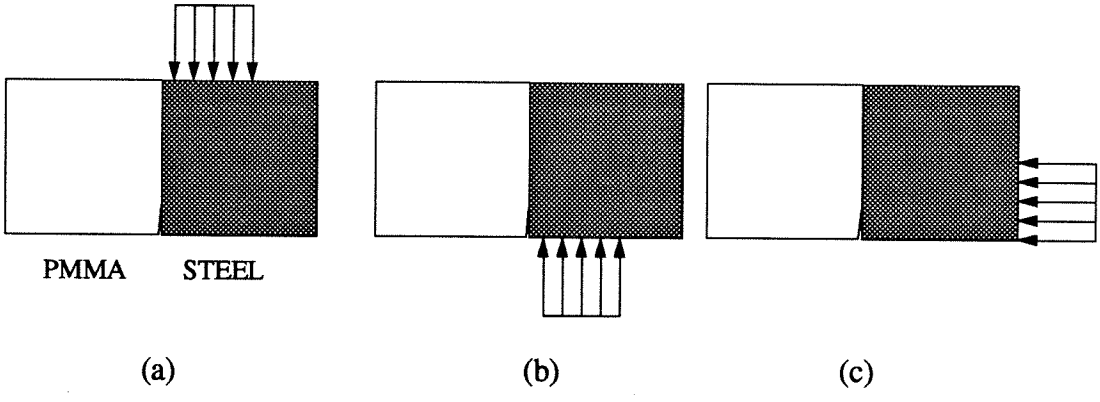

Figure 13: Loading geometries used in air gun tests.

2.3 Limitations and uncertainties of the experimental procedure

The fact that any type of experimentation in interfacial fracture is difficult, is evident from the fact that a relatively small number of experimental studies are available. The first and most crucial variable in an interfacial fracture experiment is the quality of the bond. Thetheoretical idealization of an interface as perfect and straight rarely models reality, but is most commonly used because of its simplicity. In some experimental studies researchers

t=3 μs
v=140 m/s

t=8 μs
v=720 m/s

t=13 μs
v=1100 m/s

t=16.5 μs
v=1100 m/s

Figure 14: Sequence of interferograms from a PMMA/steel air gun test.

have managed to accomplish atomistically sharp interfaces (see O'Dowd et al. (1992)). This is indeed a remarkable accomplishment from a scientific point of view. However the difficulty of producing such bonds and the resulting low strength have limited their applicability to engineering applications. In most cases interfaces are created with the aid of some adhesive. In the current study PMMA plates were bonded to metal plates using a MMA monomer and a catalyst as an adhesive. The details of this procedure were outlined in section 2.2.1. It was also shown there that the bond strength obtained was at least that of homogeneous PMMA. The bond strength in these specimens therefore seems to be satisfactory and is very repeatable. Overall the nature of the structure is still bimaterial since the mechanical properties of the adhesive are very close to those of PMMA. There will of course be some variation of mechanical properties over the 100μm wide interface. The monomer cannot polymerize to become *exactly* the same as the PMMA plate. Macroscopically though the structure would look like a bimaterial having a straight interface. If data is extracted from distances considerably away from the crack tip (2-3mm), as compared to the interface thickness, the interface will seem as a straight line. This argument is intensified by the work of Gu (1991) who performed an analytical investigation of the trimaterial problem, i.e., a bimaterial with a thin layer of adhesive between the two constituents. He found that between the macroscopic bimaterial K-field and the local near tip K-field there were only very small changes in phase angle, which vanished as the thickness of the bond went to zero.

Extreme care was taken when preparing the bimaterial specimens. The plates that would compose the bimaterial were machined to ensure flat and parallel edges. The thickness of the two plates though was not exactly the same, because of slight thickness variations in the commercially obtained PMMA. (Metals can be machined to an exact thickness specification). Differences in thickness between the two plates could be up to 0.3mm. Even if all components did have exactly the same thickness, though, it is doubtful

that they could be glued perfectly straight. Exactly what problems this thickness mismatch can cause is not clear. In hindsight it does not seem to be very severe, but its effects really cannot be quantified especially in the dynamic case.

Dynamic interfacial experimentation dramatically increases the importance of interfacial effects. It also introduces additional sources of experimental error. Paramount amongst these is the uncertainty in measuring the crack tip speed. This problem has haunted dynamic fracture experimentalists since the early days of the subject. The procedure employed to measure crack tip speed from our experimental data is simple in concept. From dynamic interferograms, of the type shown in figures 11 and 14, it is possible to measure the location of the crack tip with time. The crack tip is at the point at which all fringes are supposed to converge and meet the interface. As can be seen by the interferograms, determining the exact location of the tip is not immediately straightforward. To subsequently determine the crack tip speed by differentiation induces additional error. Differentiation is performed by fitting polynomial expressions to the crack length history and then differentiating. Errors in the crack length arise form improper positioning of the tip on the picture and from miscalculation of the scaling involved in the printed photographs. An additional error in velocity is introduced by the differentiation procedure. It was estimated that for the higher velocities the error can be in excess of $\pm$100m/s. (More results on velocity error are seen in section 3.1). This is somewhat better than most dynamic fracture experiments in the past (see Rosakis and Zehnder (1985)) because of the increased framing rate of our high speed camera system, $2\text{x}10^6$ fps, as opposed to $1\text{-}2\text{x}10^5$ fps of previously used systems. Nevertheless this remains the single most important cause of uncertainty in dynamic experimentation. One thing to note is that an overestimation of the crack tip speed for one time instant will most likely imply an underestimation for the next time instant since we are essentially taking the difference of successive crack lengths. Thus the error in crack tip speed will not always be on the same side. This makes the measured velocity data at least a very good average value.

A limitation of the experimental technique that also affects crack tip placement is the invariable presence of a shadow region around the propagating crack tip. When analyzing the optical method of CGS in transmission in section 2.1, it was noted that as a collimated beam passes through a transparent deforming material it acquires a pointwise optical path change (referred to as S in that section). If one considers the profile of rays refracted through the material one would equivalently see something of the type shown in figure 15. The initially undeformed specimen (seen from a through thickness view) deforms mainly at the vicinity of the crack front. When setting up the interferometer in front of such a specimen the physical dimensions of each component (lenses, gratings etc.) will block some of the transmitted rays; those that deviate most from parallelism in figure 15. This is an aperture effect and will result in a dark area (shadow region) around the crack tip. The aperture effect is limiting to any optical system. It can be improved, but cannot be eliminated. The susceptibility of a lens to this effect is indicated by the lens's f number. It is defined as the lens focal length over the lens diameter. The bigger the f number the worse the shadow spot problem. The camera and lenses used in this study have an f number of 22. This is rather large for a single lens. For a high speed camera system it is somewhat above average, but this is a price that is paid for having a high framing rate. The shadow effects are seen clearly in figure 14, especially at higher crack tip speeds, where larger deformations occur around the crack tip.

A second limitation of the high speed camera system is its exposure time. The exposure time, i.e., the time during which light is incident on the film track, has to be short enough to "freeze" the motion of a fast running object, but also long enough to provide enough light to expose the negative. The 30ns laser pulse width used in our experiments is the exposure time. It was seen to be long enough to expose the film with not much difficulty. In addition very sharp interferograms were obtained. The 30ns pulse time leads to a blur in the location of the crack tip of about 0.3mm (for a crack running at 1000m/s and an image magnification of 10). To calculate velocity though we take the difference

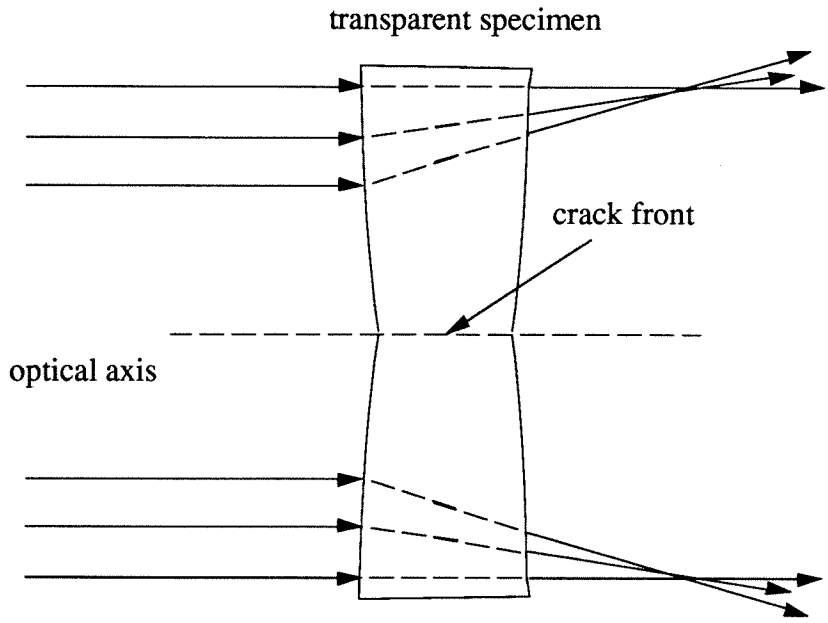

Figure 15: Profile of rays transmitted through transparent deforming cracked plate specimen.

between two successive pictures. And since the camera is operated at a framing rate of about $1x10^6$ fps, the difference in crack tip position induced by blurring is negligible (less than 0.03mm).

CHAPTER 3

SUBSONIC CRACK GROWTH ALONG BIMATERIAL INTERFACES

3.1 Experimental observations

3.1.1 Drop weight tower experiments

Several experiments were performed using the drop weight tower device. A sequence of interferograms from a PMMA/aluminum three point bend test was presented in figure 11. Figure 16 shows another sequence of interferograms from a PMMA/aluminum three point bend drop weight tower test. This figure has been taken from Tippur and Rosakis (1991). A third sequence of interferograms, this time from a one point bend PMMA/steel experiment, is shown in figure 17. Qualitatively all three figures are similar. In all tests time $t=0\mu s$ corresponds to the time of crack initiation. Interferograms at negative times have been taken before initiation. In figure 16 it can be seen that between $t=-42\mu s$ and $t=0\mu s$ the fringe pattern surrounding the initial notch tip grows in size and also rotates with respect to the notch line. The size of the fringe pattern at each time depends on the magnitude of the stress field around the tip. The particular orientation of each lobe of the pattern is dependent on the relative amounts of normal (opening) and shearing stresses around the tip (i.e., the stress mixity). The loading history of the initial notch tip can be qualitatively described as follows. After the specimen is impacted, on the metal side, a compressive stress pulse travels the vertical width of the specimen. It is reflected as a tension pulse from the traction free end on the bottom of the plate. Although impact is

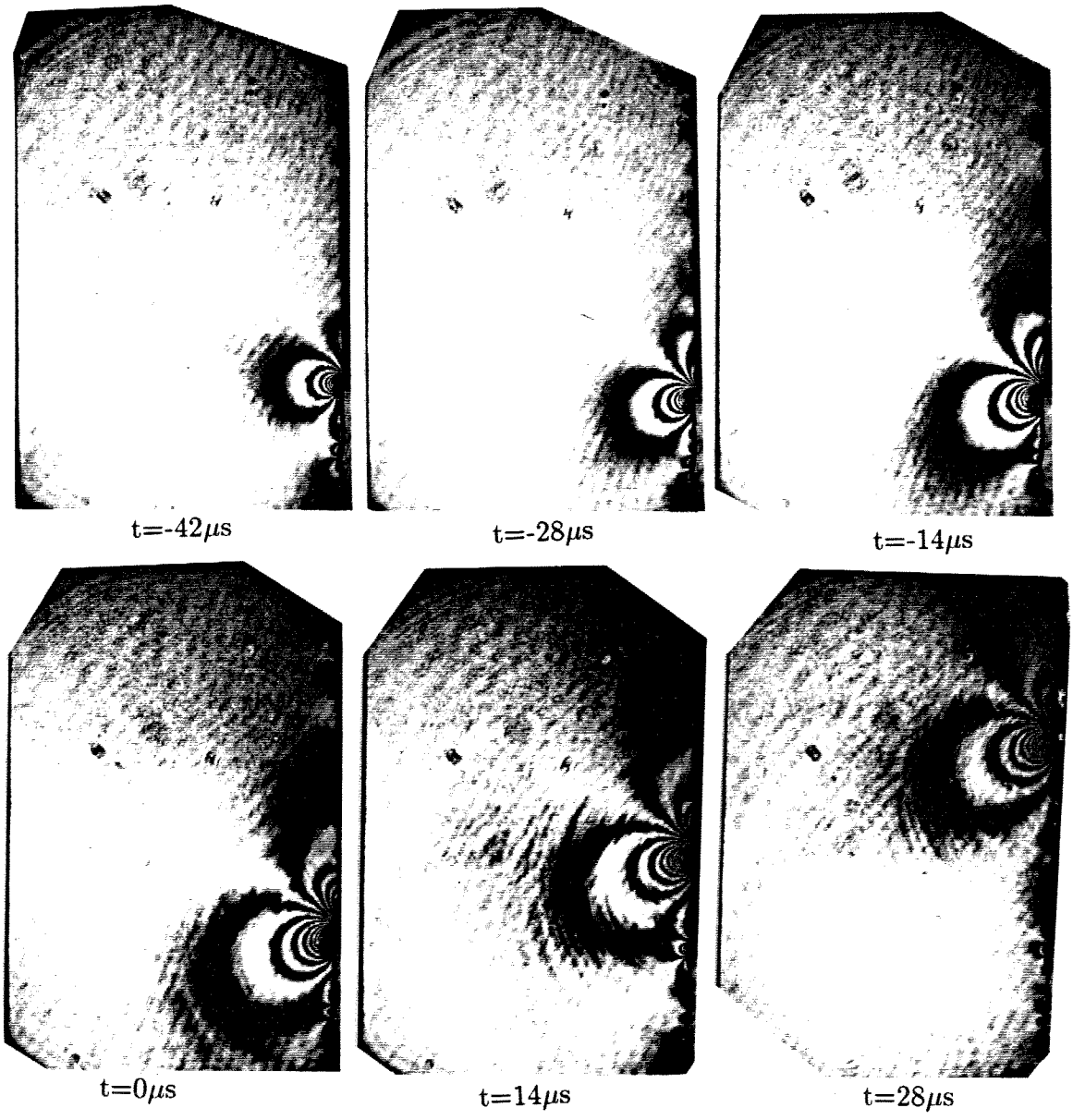

Figure 16: Selected sequence of CGS interferograms from a PMMA/aluminum three point bend drop weight tower impact test (from Tippur and Rosakis (1991)).

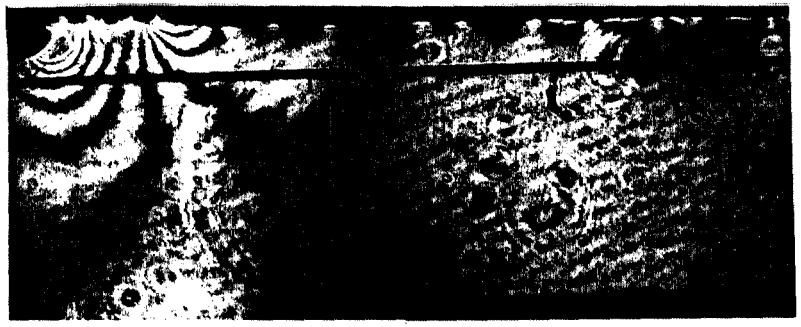

t=9.5 μs
v=640 m/s

t=16.5 μs
v=790 m/s

t=23 μs
v=800 m/s

t=32 μs
v=880 m/s

Figure 17: Selected sequence of CGS interferograms from a one point bend PMMA/steel drop weight tower test.

always on the side of the metal, a part of the initial impact pulse will also be transmitted into the PMMA side because of the existence of the bond. However, waves in the aluminum side travel much faster than in the PMMA side so the wave generated upon impact reaches the notch tip from the aluminum side first. The tip is thus loaded by subsequent arrivals of reflected waves from other boundaries of the *aluminum* plate. A time of about 65-70μs passes between the time of impact and the time of crack initiation. In this time no waves traveling in the PMMA have reached the notch tip. All deformation effects visible in the interferograms of the PMMA side are from leakage of energy from the aluminum side to the PMMA through waves crossing the interface. Essentially throughout all tests, *the crack is driven by the metal side of the bond.* Fortunately the complexity of the problem is somewhat lessened by the fact that Stoneley waves are not possible in either PMMA/aluminum or PMMA/steel interfaces (Cagniard (1962)).

The stresses around the tip grow in magnitude and change in mixity as reflected waves from other boundaries of the metal plate reach the crack tip. This is experimentally observed as a change in the size and orientation of the fringe pattern as seen in figure 16. The fringe pattern at early times (t=-42μs) is shear dominated, though the magnitude of the stresses seems rather low. The stresses at this time are primarily generated by the first reflection of the original compressive wave from the traction free end directly opposite to the impact area. They are not strong enough to initiate motion of the notch tip at this particular stress mixity. As more reflected waves reach the notch tip the stress field grows in magnitude. It is worth noting that the wave reflected from the lower right-hand corner of the aluminum side arrives at the notch tip at about the time of notch initiation. This wave is a tensile release wave that impinges at the notch at almost 90°. It therefore generates large opening stresses round the tip. This causes the observed fringe pattern to rotate. The stress field achieves appropriate conditions for notch initiation, and a crack starts propagating

dynamically along the interface. It is once more worth noting at this point that it is a wave traveling in the aluminum side that causes crack initiation.

In contrast to the pre-initiation stages, the fringe pattern around the *propagating* crack tip does not change much either in size or orientation (see figures 11, 16 and 17). This suggests that the stress field surrounding the crack tip remains relatively constant throughout crack propagation. It is the recognition of this fact that provided the strong suspicion that some fundamental physical quantities, such as stresses or crack face displacements, must remain constant during crack propagation. In chapter 4, where a particular fracture criterion will be proposed, we will investigate this further.

After the crack initiates intense stress waves are emanated from the crack tip. These waves are visible in figures 11, 16 and 17 as discrete kinks in otherwise smooth fringes. This observation is a reliable sign of the existence of very strong dynamic effects and of high velocities of crack growth that are a large fraction of the Rayleigh wave speed of PMMA (c_R^{PMMA}). It should be noted that such waves are not usually visible after crack initiation in homogeneous PMMA specimens of the same configuration and loading, where the observed maximum crack-tip speeds are around $0.4 c_R^{PMMA}$. However, such waves do appear in optical CGS or caustic patterns of growth in high strength materials (see Rosakis (1993)), when crack tip speeds are in excess of $0.4 c_R^{STEEL}$.

The actual crack tip speed and acceleration histories corresponding to the PMMA/steel experiment shown in figure 17 are plotted in figures 18(a,b). These plots were obtained in the manner outlined in section 2.3. The crack-tip speed increases to its largest value in a very short time (~15μs). This is evident by the presence of large crack-tip accelerations at the beginning of crack growth. Consistent with the observation of stress waves during crack growth is the measured maximum crack tip speed. This is seen to be around 800m/s or $0.85 c_R^{PMMA}$. This observation was rather surprising given previous experience with dynamic crack growth in homogeneous PMMA specimens of the same configuration and loading (maximum speeds of ~$0.35 c_R^{PMMA}$).

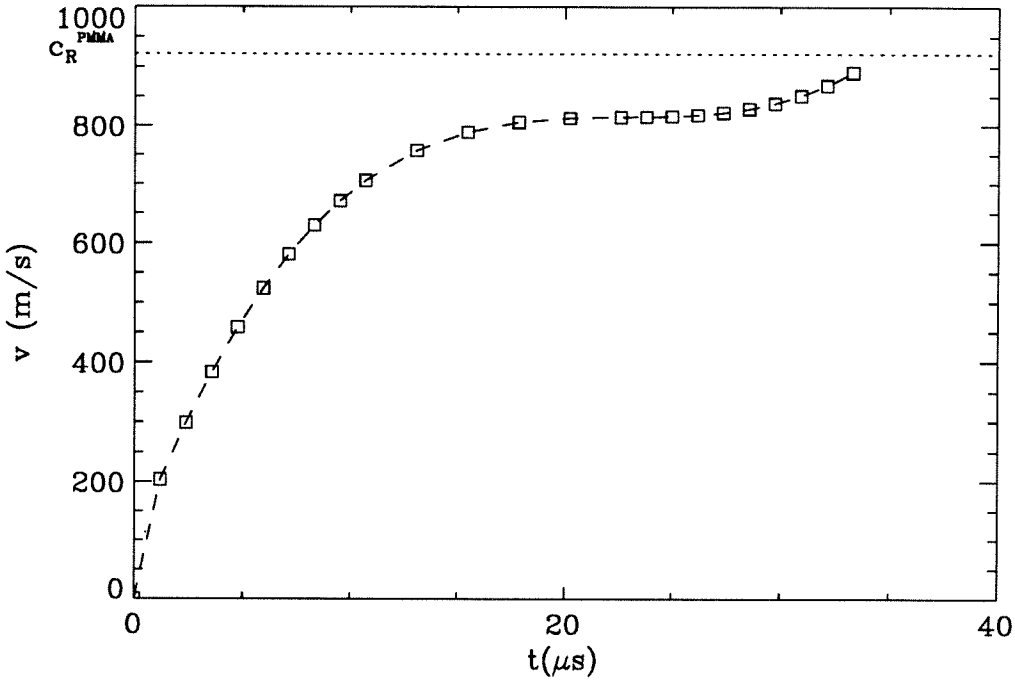

(a)

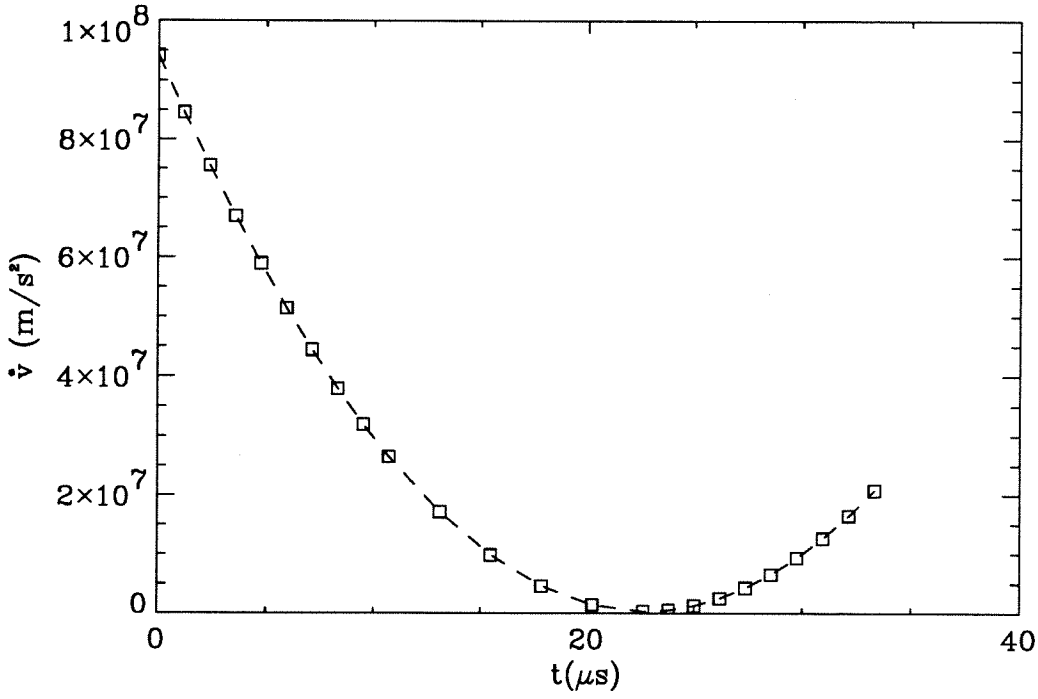

(b)

Figure 18: Velocity, (a) and acceleration, (b) time histories for the experiment shown in figure 17.

Attributing such a phenomenon to the existence of a weak bond is not very convincing since the bond calibration technique revealed a bond fracture toughness very close to that of PMMA. In fact a strong bond is *necessary* in order to drive the crack tip to higher speeds. It is already obvious in these experiments that energy transfer across the interface from the metal side is responsible for crack initiation and growth, simply because in the time frames involved very little wave motion occurs in PMMA. A strong bond is necessary because otherwise less energy would be transferred and the crack tip would not be able to propagate as fast. This fact will become even more obvious in the higher loading rate experiments described in the next section. In addition we believe that these effects of energy transfer are more pronounced because of the large mismatch of elastic properties between PMMA and aluminum or steel.

One noteworthy point is that the values of acceleration quoted in figure 18(b) are not meant to be exact quantitative results. They are products of two differentiations of the crack length history and are susceptible to error. Nevertheless these values shed light into the orders of magnitude of acceleration encountered in such an experiment.

A quantitative analysis of all interferograms presented here will be made in sections 3.2 and 3.3.

3.1.2 Gas gun experiments

Because of the intrinsic difficulties associated with the problem of dynamic interfacial fracture, few theoretical studies have been performed (Goldshtein (1967), Brock and Achenbach (1973), Atkinson (1977), Willis (1971), Willis (1973)). Even so it should be noted that there is a disagreement on the theoretically predicted value of the terminal velocity for dynamically propagating interfacial cracks. Atkinson (1977) claimed a terminal velocity equal to the lower of the Rayleigh wave speeds of the two constituents. In contrast Willis (1973) argued that the terminal velocity was a little greater than the lower of the two

Rayleigh wave speeds. More recently the problem of dynamic interfacial crack growth has been studied by Yang et al. (1991). They provided an asymptotic solution for the stress field surrounding the tip of a dynamically propagating bimaterial crack. (Details of their analysis are presented in section 3.2.1.) One very important conclusion of their study is that as the crack tip velocity approaches the lower of the two Rayleigh wave speeds a finite amount of energy has to be transmitted to the crack tip to maintain extension at $c_R^{(1)}$ with non-zero complex stress intensity factor. This is unlike the homogeneous case where an infinite amount of energy has to be transmitted to the crack tip to maintain extension at c_R if the stress intensity factor is non-zero (Freund (1990)). This obviously makes it energetically impossible for a crack in a *homogeneous* solid to exceed the material's Rayleigh wave speed, but apparently no such restriction exists in the bimaterial case.

As was seen in figure 18, experimental measurements from the drop tower tests resulted in crack-tip speeds close to c_R^{PMMA} (the lower Rayleigh wave speed). In fact towards the end of our observation window, the velocity seemed to rise further. Since no energetic restrictions exist for the bimaterial case, we believed that it would be possible to drive the interfacial crack to higher speeds by subjecting the specimen to different loading histories resulting in higher rates of loading. Use of a high speed gas gun and a one point bend loading configuration were made to produce loading rates in cracked bimaterial plates that were higher than those encountered in drop weight tower experiments. The experimental procedure followed was described in section 2.2.3. A sequence of selected interferograms from such a test was shown in figure 14. The resulting crack tip-speed and acceleration histories for this particular test are shown in figures 19(a,b). In figure 19(a) we have superposed error bars for the measured velocity at each time instant. The error bars contain estimates of all factors affecting crack-tip speed measurements as described in section 2.3. It is clear that the Rayleigh wave speed of Plexiglas (c_R^{PMMA}) has been exceeded by the crack tip. In addition it seems that the shear wave speed of Plexiglas has been exceeded. (Recall $c_R^{PMMA} = 920m/s$ in plane stress and $c_S^{PMMA} = 1000m/s$.) Observations

and results for crack growth exceeding c_S^{PMMA} will be discussed in chapter 5. In subsequent sections we will only focus on the case of *subsonic* crack growth and in particular $v < c_R^{PMMA}$. (v=crack tip speed).

In the gas gun experiments it was observed that the time of crack initiation was around 30μs after impact. In these experiments therefore the influence of the metal side on crack propagation is even more pronounced than before, since in 30μs a dilatational wave in PMMA travels less than half the specimen width. In these tests crack initiation is essentially due to the higher loading rates exerted by the air gun device. In all air gun tests the steel side of the specimen was impacted at 20m/s. This is five times larger than that produced from the drop weight device. This means that the initial compressive wave generated by the air gun is much more intense than that generated by the drop weight tower. (The strength of the compressive wave will roughly be $0.5\rho c_0 v_0$ where ρ is the density, c_0 is a wave speed of the material and v_0 the impact velocity). Another significant difference between the two types of experiments is the width of the impactor. The drop weight device applies a load over a very small area (<3mm) on the top of the specimen. The impact area in an air gun test is dictated by the diameter of the projectile used. In our case this was 50mm. Figure 20(a) shows a schematic of the impacting projectile. Figure 20(b) shows an approximation of the wavefront diagram present in the metal side only, a short time after impact. The main compressive wave (A) generated, extends about 50mm in length. In addition, an unloading wave (B) originates at the left corner of the loading area and propagates at c_S^{STEEL}. This allows the top surface of the specimen to remain traction free outside the loading area. Two other waves will be generated at the corner of the interface C. Both waves A and C will provide some energy transfer into the PMMA side and will load the crack tip when they travel the width of the specimen. For comparison purposes, the quarter circle in the PMMA side in figure 20(b) represents the relative position of a dilatational wave traveling in PMMA.

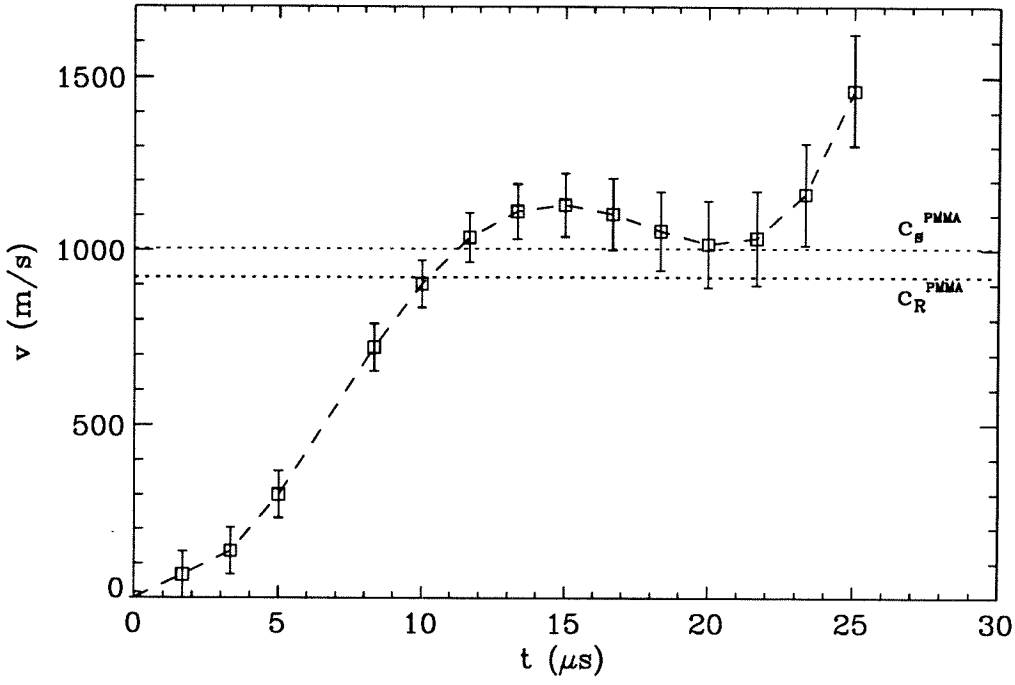

(a)

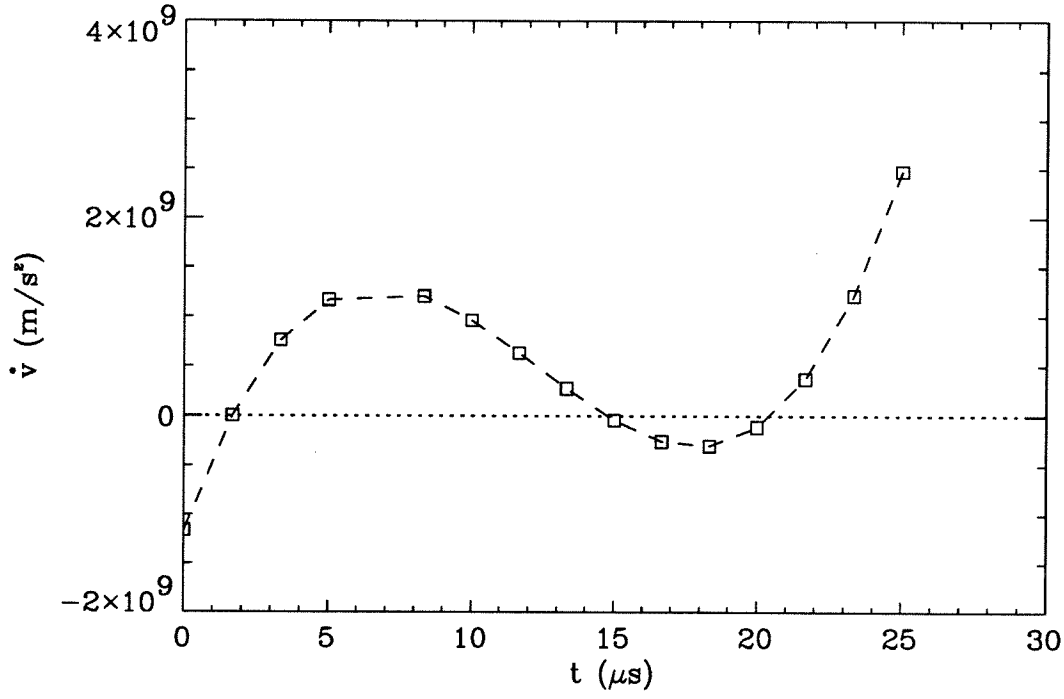

(b)

Figure 19: Velocity, (a) and acceleration, (b) time histories for the experiment shown in figure 14.

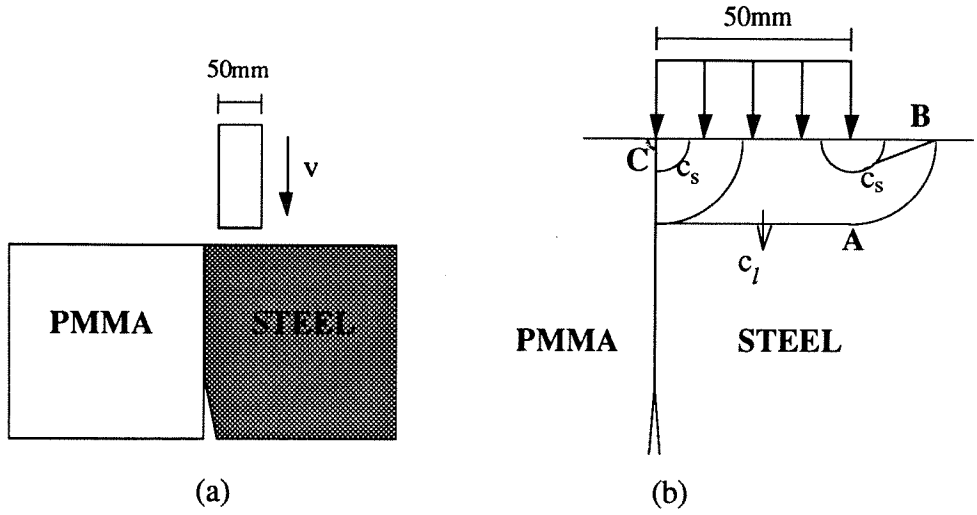

Figure 20: (a) Schematic of impact geometry in air gun experiments, (b) Wave diagram after impact in steel side.

The main dilatational wave A is almost normal to the interface and is traveling parallel to it. Thus it loads the crack tip in a shear fashion. The wave then reflects off the bottom surface as a tension wave and reloads the crack tip again in shear. Because the magnitudes of waves A, B and C are much greater than in the case of drop weight tower loading, the crack tip after a very short time has enough energy stored in it to initiate propagation, even though it is in a shear dominated stress field. The observed initiation time of about 30μs is much less than the 70μs of the previous experiments. It also correlates well with the time it takes wave A to travel the width of the specimen, reflect off the bottom surface of the metal side and reach the tip once again. The fact that in the air gun tests the crack initiates and grows under shear conditions can also be seen by looking at the first two interferograms of figure 14. They do not resemble those obtained during propagation after drop weight loading (see figures 11 and 16). They more resemble the pre-initiation pictures in figure 16, which are also shear dominated (at a time when the stresses have not reached a level high enough to initiate crack growth). Quantitative evidence that

growth in the gas gun experiments is more shear dominated than in the drop weight experiments is provided in chapter 4.

3.2 Theoretically predicted crack-tip fields and data reduction

Even though the optical method of Coherent Gradient Sensing provides full field information about stress gradients, it is impractical to actually compute them point by point for each interferogram. It is more efficient, and of greater practical value, to identify the few fracture parameters that characterize the crack-tip stress field. Typically in optical experiments quantitative analysis of the results is performed, by extracting two-dimensional, near tip fracture parameters such as stress intensity factor K and phase angle ϕ, or global parameters such as energy release rate G. This procedure has been guided by theoretical predictions that show crack tip autonomy in the region surrounding a crack tip. Crack tip autonomy means that the asymptotic stress field predicted at a crack tip has a universal spatial structure. The only difference between particular crack problems is in the quantities K and ϕ. Traditionally, deriving K and ϕ from optical experiments is performed by fitting the experimentally obtained fringe patterns to the theoretically predicted stress field which has K and ϕ as parameters. Herein lies the advantage of using a full field optical technique rather than a point or line measurement. Instead of *assuming* the existence of the theoretically predicted spatial structure of the stress field, it is possible to *verify* its *dominance* in whole or in part of a fracture specimen. A region surrounding the crack tip in which the stress field is well described by the most singular term of the asymptotic expansion for stress is called a K-dominant region (K^d in the dynamic case). In certain cases it is possible that no region of K^d-dominance exists. This usually occurs in regions relatively far from the crack tip or in experiments showing transient effects. (e.g., rapidly changing crack tip speed). In such cases the deformation field around the crack tip may be better approximated by a higher order analysis (see Freund and Rosakis (1992)).

In Tippur and Rosakis (1991) use of the quasi-static plane stress asymptotic stress field (equation (1.2)) was made when extracting data from dynamic interferograms. Obviously this is not a correct approach. However, those were the only theoretical results available at the time. Since then a few researchers (Yang et al. (1991), Wu (1991), Deng (1991) and Deng (1992)) have determined the spatial structure of the near tip stress field around a bimaterial crack, propagating dynamically under plane stress and steady-state conditions. In the next section we will present the singular stress field derived by Yang et al. (1991). A higher order transient analysis obtained by Liu et al. (1993) is presented in section 3.2.2. A description of the procedure followed to fit the field to the optical interferograms and determine the region of K^d-dominance will be given in section 3.2.3.

3.2.1 Singular field (K^d-dominance)

For interfacial cracks propagating dynamically under steady-state conditions in bimaterial specimens Yang et al. (1991) observed that near the crack tip the stress field assumes the form,

$$\sigma_{\alpha\beta} = Re\left\{\frac{K^d r^{i\varepsilon}}{\sqrt{2\pi r}}\right\}\tilde{\sigma}^{(1)}_{\alpha\beta}(\theta,v) + Im\left\{\frac{K^d r^{i\varepsilon}}{\sqrt{2\pi r}}\right\}\tilde{\sigma}^{(2)}_{\alpha\beta}(\theta,v)\ , \tag{3.1}$$

where r, θ are polar coordinates of a coordinate system *translating* with the crack tip at speed v and $K^d = K_1^d + iK_2^d$ is the *complex dynamic* stress intensity factor. Analytical expressions for $\tilde{\sigma}^{(1)}_{\alpha\beta}$ and $\tilde{\sigma}^{(2)}_{\alpha\beta}$ are given in Yang et al. (1991). Equation (3.1) is in analogy to the static result shown in equation (1.2). Most features of the quasi-static stress field are maintained here. One difference though is that the material mismatch parameter $\varepsilon = \hat{\varepsilon}(v)$ is now a function of crack-tip speed as well as of the moduli of the materials of the bimaterial combination.

By using equation (3.1) and after some algebraic manipulation $\hat{\sigma}_{11} + \hat{\sigma}_{22}$ for material-1 (above the interface) can be written as,

$$\hat{\sigma}_{11}+\hat{\sigma}_{22}=\frac{A}{\sqrt{2\pi r_1}}\left[\left(1+\alpha_s^2-2\eta\alpha_s\right)e^{\varepsilon(\pi-\theta_1)}\cos\left(\frac{\theta_1}{2}-\phi-\varepsilon\ln r_1\right)\right.$$

$$\left.+\left(1+\alpha_s^2+2\eta\alpha_s\right)e^{-\varepsilon(\pi-\theta_1)}\cos\left(\frac{\theta_1}{2}+\phi+\varepsilon\ln r_1\right)\right],\ r\to 0,\ 0\le\theta\le\pi, \tag{3.2}$$

where

$$A=\frac{\left(\alpha_1^2-\alpha_s^2\right)|K^d|}{\left(4\alpha_1\alpha_s-\left(1+\alpha_s^2\right)^2\right)\cosh(\varepsilon\pi)},$$

$$\alpha_{1,s}=\left(1-\frac{\dot{a}^2}{c_{1,s}^2}\right)^{1/2},\quad \theta_1=\tan^{-1}\left[\left(\alpha_1 x_2\right)/x_1\right],\quad r_1=\sqrt{x_1^2+\alpha_1^2x_2^2},$$

$$K^d(t)=K_1^d(t)+iK_2^d(t),\qquad \phi(t)=\tan^{-1}\left(K_2^d(t)/K_1^d(t)\right),$$

and $c_{1,s}$ are the longitudinal and shear wave speeds respectively and $\varepsilon=\hat{\varepsilon}(v),\ \eta=\hat{\eta}(v),$ are functions of crack-tip speed and material properties. Parameters ε and η are two mismatch parameters that characterize the interface. They are derived in Yang et al. (1991) . Parameter ε is given by

$$\varepsilon=\frac{1}{2\pi}\ln\left(\frac{1-\beta}{1+\beta}\right). \tag{3.3}$$

This equation is the same as (1.4) only now β is a function of crack-tip speed v in addition to material properties, and is given by

$$\beta=-H_{12}\left(H_{11}H_{22}\right)^{-\frac{1}{2}}.$$

Parameter η can also be expressed as a function of $H_{\alpha\beta}$ through,

$$\eta = (H_{22}/H_{11})^{\frac{1}{2}}.$$

Functions $H_{\alpha\beta}$ are given in the appendix for the sake of brevity. ε is called the (dynamic) oscillatory index and η the traction resolution factor.

The variation of ε and η with crack tip speed is shown in figures 21 and 22 respectively. Both these figures are for a PMMA/steel bimaterial combination having the material properties shown in table 1. Material-1 is PMMA and Material-2 is steel. The plots are for crack tip speeds below the Rayleigh wave speed of Plexiglas, which is the regime in which (3.1) is valid. The parameters are such that $\varepsilon \to \varepsilon_0$, $\eta \to 1$ as $v \to 0$ and equation (3.1) reduces to equation (1.2) for $v=0$. ε_0 is now the quasi-static oscillatory index seen in section 1.2. It can be clearly seen in figure 21 that ε is an increasing function of crack-tip speed, but for low values it does not vary drastically. At around 60%-70% of the shear wave speed of Plexiglas, c_S^{PMMA}, it starts increasing rapidly and asymptotes to infinity as the crack tip speed approaches the Rayleigh wave speed of Plexiglas (at the dotted line in figure 21). This implies that oscillatory effects will become more dominant as the crack-tip speed increases. The effects of ε will be discussed in more detail in section 3.3. On the other hand, the variation of η is not as severe and the quantity remains bounded at the Rayleigh wave speed of PMMA.

The field quantity of interest in analyzing the CGS fringe patterns for material-1 is $ch\partial(\hat{\sigma}_{11}+\hat{\sigma}_{22})/\partial x_1$ (see equation (2.11)). By differentiating equation (3.2) with respect to x_1 we have,

$$\begin{aligned} ch\frac{\partial(\hat{\sigma}_{11}+\hat{\sigma}_{22})}{\partial x_1} = \frac{chr_1^{-3/2}e^{-\varepsilon(\pi-\theta_1)}A}{2\sqrt{2\pi}}\Bigg[& -(1+\alpha_s^2-2\eta\alpha_s)e^{2\varepsilon(\pi-\theta_1)}\cos\left(\frac{3\theta_1}{2}-\phi-\varepsilon\ln r\right) \\ & -(1+\alpha_s^2+2\eta\alpha_s)\cos\left(\frac{3\theta_1}{2}+\phi+\varepsilon\ln r\right) \\ & +2\varepsilon(1+\alpha_s^2-2\eta\alpha_s)e^{2\varepsilon(\pi-\theta_1)}\sin\left(\frac{3\theta_1}{2}-\phi-\varepsilon\ln r\right) \\ & -2\varepsilon(1+\alpha_s^2+2\eta\alpha_s)\sin\left(\frac{3\theta_1}{2}+\phi+\varepsilon\ln r\right)\Bigg], \end{aligned} \tag{3.4}$$

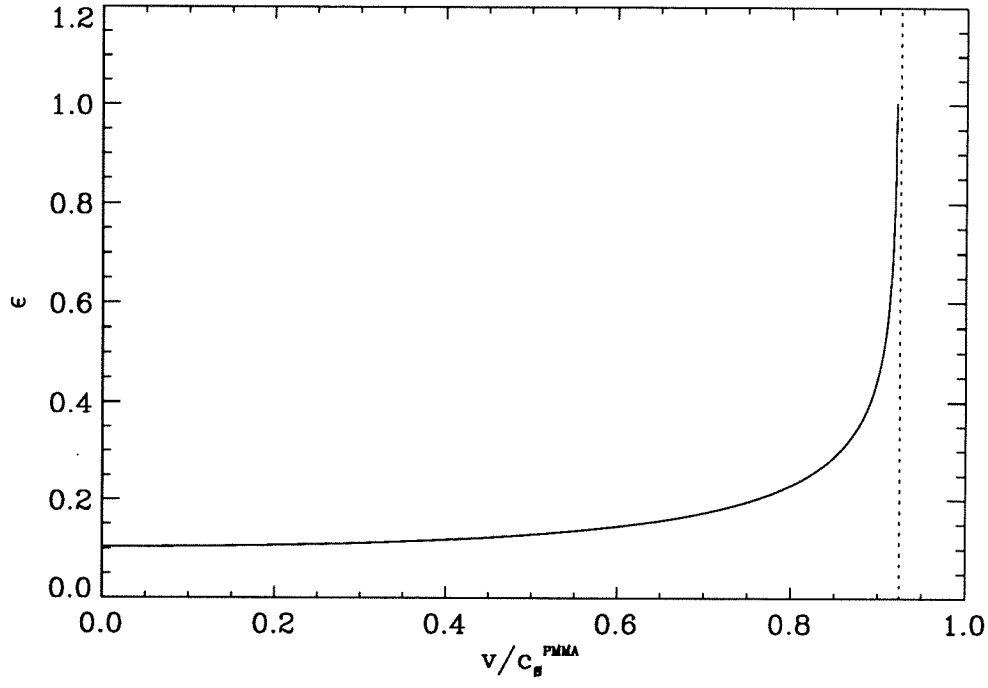

Figure 21: Variation of oscillatory index with velocity for a PMMA/steel bimaterial system (plane stress conditions).

where A is as defined in (3.2) and $0 \leq \theta \leq \pi$. One note to be made here is that to obtain the stress field in the lower material we need to substitute $-\pi$ for π in equation (3.2). In the present study though we only obtain interferograms from the deformation of material-1 (PMMA) so this need not be done.

The above relation exhibits crack tip autonomy. Only the values of the dynamic complex stress intensity factor and the crack tip speed are undetermined by the asymptotic analysis. The crack-tip velocity is an external parameter that must be furnished by separate experimental measurements. In our case these measurements are made by recording the crack length variation with time. It is possible to investigate the effect of v on the predicted fringe pattern by plotting contours of equation (3.4) for different values of crack propagation velocity. Such plots are shown in figures 23(a,b). Values of $|K^d| = 1Pa\sqrt{m}$

and ϕ=45° have been used in both 23(a) and (b). The difference between the two is that they represent crack growth at speeds $v = 0.3c_s^{PMMA}$ and $v = 0.8c_s^{PMMA}$. Clearly the orientation of the stress field depends considerably on crack tip speed. This effect is created by the presence

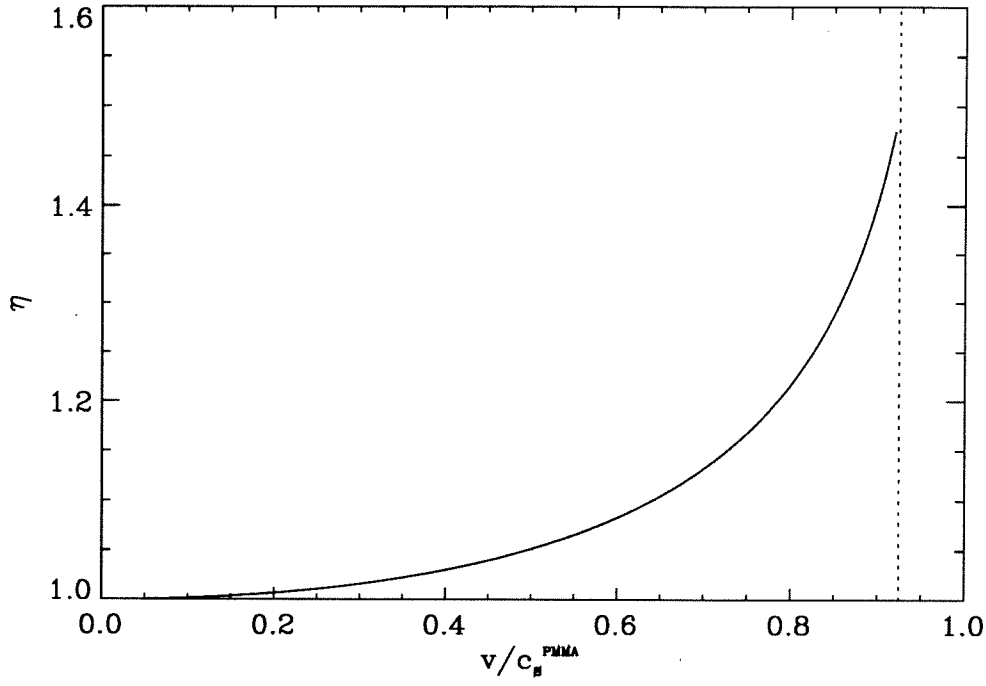

Figure 22: Variation of traction resolution factor with velocity for a PMMA/steel bimaterial system (plane stress conditions).

of the term εlnr in the arguments of the sines and cosines in equation (3.4). It is obviously a complementary effect to a change in phase angle ϕ.

The value of K^d will depend upon the particular geometry and loading of each specimen and has to be determined experimentally. It is expected to vary with time as reflected waves from the specimen boundaries return to the crack tip. We can use equation (3.4) to extract K^d as a function of time from optical interferograms like those seen in figures 11, 14, 16 and 17. From the above discussion it becomes obvious that extraction of parameters like K^d is possible *provided* that experimental data are gathered from a region

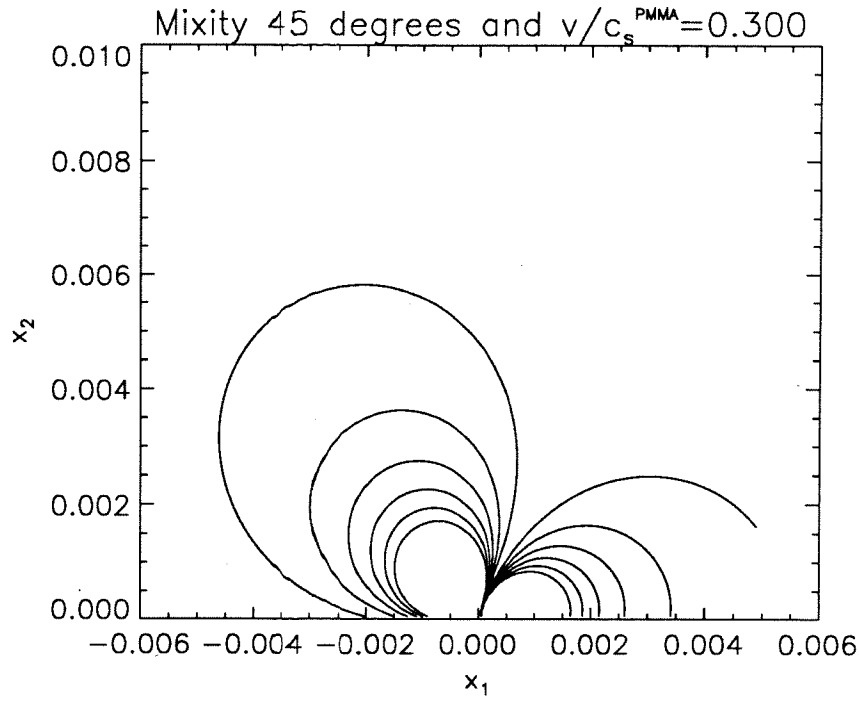

(a)

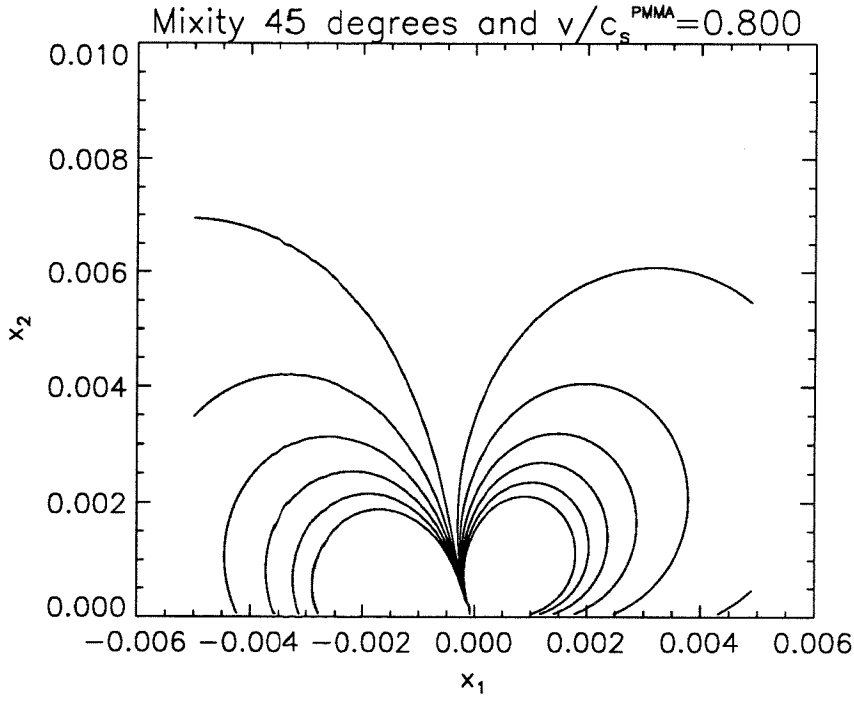

(b)

Figure 23(a,b): Theoretically predicted fringe patterns, from equation (3.4), at two different values of crack-tip speed ($|K^d|$=1PA$\sqrt{m}$, ϕ=45°).

near the moving crack tip characterized by the structure presented in equations (3.2) and (3.4), i.e., that there exists a region of K^d-dominance. The procedure of obtaining K^d is outlined in section 3.2.3, and determining its region of dominance, is outlined in section 3.3. In the case that no region in the specimen is characterized by such a K^d-field, the use of a higher order analysis is mandated. Such an analysis for a transiently propagating interfacial crack has been provided by Liu et al. (1993) and is presented in the next section.

3.2.2 Higher order transient analysis

When determining the singular stress field of equation (3.1) an assumption of steady-state crack growth was made by Yang et al. (1991). However, it has been experimentally observed that very high crack tip accelerations occur during the initial stages of dynamic interfacial crack growth (see figures 18 and 19). In these cases it is obvious that the assumption of steady-state crack growth is violated. It is this reason that motivated Liu et al. (1993) to lift the restriction of steady-state conditions and to provide a transient higher order analysis of interfacial crack growth. In Liu et al. (1993) it was shown that the x_1-gradient of the trace of the stress tensor under plane stress transient conditions is given by,

$$\begin{aligned}\frac{(\sigma_{11}+\sigma_{22})_{,1}}{2\mu(\alpha_l^2-\alpha_s^2)} &= |A_0(t)|\left\{\Pi_0(\theta_l)\cos(\varepsilon \ln r_l)+\tilde{\Pi}_0(\theta_l)\sin(\varepsilon \ln r_l)\right\}r_l^{-3/2} \\ &+\dot{\varepsilon}\left\{\Pi_d(\theta_l)\cos(\varepsilon \ln r_l)+\tilde{\Pi}_d(\theta_l)\sin(\varepsilon \ln r_l)\right\}r_l^{-1/2}(\ln r_l)^2 \\ &+\left\{\Pi_t(\theta_l)\cos(\varepsilon \ln r_l)+\tilde{\Pi}_t(\theta_l)\sin(\varepsilon \ln r_l)\right\}r_l^{-1/2}\ln r_l \\ &+\left\{\Pi_n(\theta_l)\cos(\varepsilon \ln r_l)+\tilde{\Pi}_n(\theta_l)\sin(\varepsilon \ln r_l)\right\}r_l^{-1/2} \\ &+|A_2(t)|\left\{\Pi_2(\theta_l)\cos(\varepsilon \ln r_l)+\tilde{\Pi}_2(\theta_l)\sin(\varepsilon \ln r_l)\right\}r_l^{-1/2} \\ &+O(r_l),\end{aligned} \tag{3.5}$$

where

$$\Pi_0(\theta_l) = a_0(t)e^{-\varepsilon\theta_l}\cos\left(\frac{3\theta_l}{2} - \Phi(A_0)\right) + b_0(t)e^{\varepsilon\theta_l}\cos\left(\frac{3\theta_l}{2} + \Phi(A_0)\right),$$

$$\tilde{\Pi}_0(\theta_l) = a_0(t)e^{-\varepsilon\theta_l}\sin\left(\frac{3\theta_l}{2} - \Phi(A_0)\right) - b_0(t)e^{\varepsilon\theta_l}\sin\left(\frac{3\theta_l}{2} + \Phi(A_0)\right),$$

$$\Pi_2(\theta_l) = a_0(t)e^{-\varepsilon\theta_l}\cos\left(\frac{\theta_l}{2} - \Phi(A_2)\right) + b_0(t)e^{\varepsilon\theta_l}\cos\left(\frac{\theta_l}{2} + \Phi(A_2)\right),$$

$$\tilde{\Pi}_2(\theta_l) = a_0(t)e^{-\varepsilon\theta_l}\sin\left(\frac{\theta_l}{2} - \Phi(A_2)\right) - b_0(t)e^{\varepsilon\theta_l}\sin\left(\frac{\theta_l}{2} + \Phi(A_2)\right),$$

$$\Pi_d(\theta_l) = |\Omega_d(t)|e^{-\varepsilon\theta_l}\cos\left(\frac{\theta_l}{2} - \Phi(\Omega_d)\right) - |\tilde{\Omega}_d(t)|e^{\varepsilon\theta_l}\cos\left(\frac{\theta_l}{2} + \Phi(\tilde{\Omega}_d)\right),$$

$$\tilde{\Pi}_d(\theta_l) = |\Omega_d(t)|e^{-\varepsilon\theta_l}\sin\left(\frac{\theta_l}{2} - \Phi(\Omega_d)\right) + |\tilde{\Omega}_d(t)|e^{\varepsilon\theta_l}\sin\left(\frac{\theta_l}{2} + \Phi(\tilde{\Omega}_d)\right),$$

$$\begin{aligned}\Pi_d(\theta_l) = {} & |A_t(t)|e^{-\varepsilon\theta_l}\cos\left(\frac{\theta_l}{2} - \Phi(A_t)\right) - |\tilde{A}_t(t)|e^{\varepsilon\theta_l}\cos\left(\frac{\theta_l}{2} - \Phi(\tilde{A}_t)\right) \\ & + |B_t(t)|e^{-\varepsilon\theta_l}\cos\left(\frac{5\theta_l}{2} - \Phi(B_t)\right) - |\tilde{B}_t(t)|e^{\varepsilon\theta_l}\cos\left(\frac{5\theta_l}{2} - \Phi(\tilde{B}_t)\right) \\ & + 2\dot{\varepsilon}\left\{|\Omega_d(t)|e^{-\varepsilon\theta_l}\sin\left(\frac{\theta_l}{2} - \Phi(\Omega_d)\right) - |\tilde{\Omega}_d(t)|e^{\varepsilon\theta_l}\sin\left(\frac{\theta_l}{2} - \Phi(\tilde{\Omega}_d)\right)\right\}\theta_l,\end{aligned}$$

$$\begin{aligned}\tilde{\Pi}_t(\theta_l) = {} & |A_t(t)|e^{-\varepsilon\theta_l}\sin\left(\frac{\theta_l}{2} - \Phi(A_t)\right) + |\tilde{A}_t(t)|e^{\varepsilon\theta_l}\sin\left(\frac{\theta_l}{2} - \Phi(\tilde{A}_t)\right) \\ & + |B_t(t)|e^{-\varepsilon\theta_l}\sin\left(\frac{5\theta_l}{2} - \Phi(B_t)\right) + |\tilde{B}_t(t)|e^{\varepsilon\theta_l}\cos\left(\frac{5\theta_l}{2} - \Phi(\tilde{B}_t)\right) \\ & - 2\dot{\varepsilon}\left\{|\Omega_d(t)|e^{-\varepsilon\theta_l}\cos\left(\frac{\theta_l}{2} - \Phi(\Omega_d)\right) + |\tilde{\Omega}_d(t)|e^{\varepsilon\theta_l}\cos\left(\frac{\theta_l}{2} - \Phi(\tilde{\Omega}_d)\right)\right\}\theta_l,\end{aligned}$$

$$\begin{aligned}\Pi_{tt}(\theta_l) = {} & |A_{tt}(t)|e^{-\varepsilon\theta_l}\cos\left(\frac{\theta_l}{2} - \Phi(A_{tt})\right) - |\tilde{A}_{tt}(t)|e^{\varepsilon\theta_l}\cos\left(\frac{\theta_l}{2} - \Phi(\tilde{A}_{tt})\right) \\ & + |B_{tt}(t)|e^{-\varepsilon\theta_l}\cos\left(\frac{5\theta_l}{2} - \Phi(B_{tt})\right) - |\tilde{B}_{tt}(t)|e^{\varepsilon\theta_l}\cos\left(\frac{5\theta_l}{2} - \Phi(\tilde{B}_{tt})\right)\end{aligned}$$

$$+\left|C_{tt}(t)\right|e^{-\varepsilon\theta_l}\cos\left(\frac{9\theta_l}{2}-\Phi\left(C_{tt}\right)\right)-\left|\tilde{C}_{tt}(t)\right|e^{\varepsilon\theta_l}\cos\left(\frac{9\theta_l}{2}-\Phi\left(\tilde{C}_{tt}\right)\right)$$

$$+\left\{\left|A_t(t)\right|e^{-\varepsilon\theta_l}\sin\left(\frac{\theta_l}{2}-\Phi\left(A_t\right)\right)+\left|\tilde{A}_t(t)\right|e^{\varepsilon\theta_l}\sin\left(\frac{\theta_l}{2}-\Phi\left(\tilde{A}_t\right)\right)\right\}\theta_l$$

$$+\left\{\left|B_t(t)\right|e^{-\varepsilon\theta_l}\sin\left(\frac{5\theta_l}{2}-\Phi\left(B_t\right)\right)-\left|\tilde{B}_t(t)\right|e^{\varepsilon\theta_l}\sin\left(\frac{5\theta_l}{2}-\Phi\left(\tilde{B}_t\right)\right)\right\}\theta_l$$

$$-\dot{\varepsilon}\left\{\left|\Omega_d(t)\right|e^{-\varepsilon\theta_l}\cos\left(\frac{\theta_l}{2}-\Phi\left(\Omega_d\right)\right)-\left|\tilde{\Omega}_d(t)\right|e^{\varepsilon\theta_l}\cos\left(\frac{\theta_l}{2}-\Phi\left(\tilde{\Omega}_d\right)\right)\right\}\theta_l^2,$$

$$\tilde{\Pi}_{tt}(\theta_l)=\left|A_{tt}(t)\right|e^{-\varepsilon\theta_l}\sin\left(\frac{\theta_l}{2}-\Phi\left(A_{tt}\right)\right)+\left|\tilde{A}_{tt}(t)\right|e^{\varepsilon\theta_l}\sin\left(\frac{\theta_l}{2}-\Phi\left(\tilde{A}_{tt}\right)\right)$$

$$+\left|B_{tt}(t)\right|e^{-\varepsilon\theta_l}\sin\left(\frac{5\theta_l}{2}-\Phi\left(B_{tt}\right)\right)+\left|\tilde{B}_{tt}(t)\right|e^{\varepsilon\theta_l}\cos\left(\frac{5\theta_l}{2}-\Phi\left(\tilde{B}_{tt}\right)\right)$$

$$+\left|C_{tt}(t)\right|e^{-\varepsilon\theta_l}\sin\left(\frac{9\theta_l}{2}-\Phi\left(C_{tt}\right)\right)+\left|\tilde{C}_{tt}(t)\right|e^{\varepsilon\theta_l}\sin\left(\frac{9\theta_l}{2}-\Phi\left(\tilde{C}_{tt}\right)\right)$$

$$-\left\{\left|A_t(t)\right|e^{-\varepsilon\theta_l}\cos\left(\frac{\theta_l}{2}-\Phi\left(A_t\right)\right)+\left|\tilde{A}_t(t)\right|e^{\varepsilon\theta_l}\cos\left(\frac{\theta_l}{2}-\Phi\left(\tilde{A}_t\right)\right)\right\}\theta_l$$

$$-\left\{\left|B_t(t)\right|e^{-\varepsilon\theta_l}\cos\left(\frac{5\theta_l}{2}-\Phi\left(B_t\right)\right)+\left|\tilde{B}_t(t)\right|e^{\varepsilon\theta_l}\cos\left(\frac{5\theta_l}{2}-\Phi\left(\tilde{B}_t\right)\right)\right\}\theta_l$$

$$-\dot{\varepsilon}\left\{\left|\Omega_d(t)\right|e^{-\varepsilon\theta_l}\sin\left(\frac{\theta_l}{2}-\Phi\left(\Omega_d\right)\right)+\left|\tilde{\Omega}_d(t)\right|e^{\varepsilon\theta_l}\sin\left(\frac{\theta_l}{2}-\Phi\left(\tilde{\Omega}_d\right)\right)\right\}\theta_l^2.$$

This x_1-gradient contains 4 orders of r_l. They are $r_l^{-3/2}$, $r_l^{-1/2}(\ln r)^2$, $r_l^{-1/2}\ln r$ and $r_l^{-1/2}$. It also contains 28 undetermined functions of time. Some of these constants are related in a complicated fashion presented in Liu et al. (1993). For this study, and for the subsequent fitting procedure, all 28 functions of time shall be considered independent because it is far too complex to do otherwise. The two first functions, $|A_0|$ and $\Phi(A_0)$, are related to $/K^d/$ and ϕ (or K_1^d, K_2^d) of Yang et al. (1991). In fact the spatial structure of the most singular term of equation (3.5) reduces to equation (3.4). Under steady-state conditions, equation (3.5) reduces to an expression with 4 terms which are identical to the

first 4 terms of the higher-order steady-state expansion derived by Deng (1992). There is an essential difference however. The undetermined parameters of the transient asymptotic analysis are still allowed to be functions of time while in steady-state they are required to be constant. The transient higher order contributions to the expression of (3.5) are those that exhibit a $r_l^{-1/2}(\ln r)^2$ and $r_l^{-1/2}\ln r$ radial dependence. It is worth noting that most of these transient terms are multiplied by the quantity $\dot{\varepsilon}$, the rate of change of the oscillatory index with time ($\dot{\varepsilon} = \varepsilon'(v)\dot{v}$). Thus, to a certain extent , $\dot{\varepsilon}$ is a measure of transience of the propagating crack. If $\dot{\varepsilon}=0$ most, but not all transient terms disappear. Those that remain are those related to the rate of change of the complex stress intensity factor. Note that it is possible for $\dot{\varepsilon}$ to be small if a large acceleration exists and $\varepsilon'(v)$ is small. Conversely it is possible to have a large $\dot{\varepsilon}$ corresponding to small $\dot{v}$ but large $\varepsilon'(v)$. Whether or not $\dot{\varepsilon}$ can be used as reliable measure of transience will be investigated in a subsequent section.

It is clear at this point that analysis of the fringe patterns obtained from a dynamic experiment can be made using either equation (3.4) or equation (3.5). The choice of one or the other depends on whether a region of K^d-dominance has been established somewhere outside the near tip three-dimensional zone. Use of either equation allows estimation of the time variation of the relevant parameters. The procedure of doing so is outlined in the next section.

3.2.3 Fitting procedure

Data reduction to obtain values of the stress intensity factor is performed by a least squares fitting procedure. The quantity minimized when fitting a K^d-dominant field is the difference of the measured fringe value, $np/ch\Delta$, and the theoretically predicted one from equation (3.4). Define function $\hat{f}$ as follows,

$$\hat{f}(r,\theta;K_1^d,K_2^d) = \frac{K_1^d C}{\sqrt{2\pi r}}\left\{P_{11}\cos\left(\frac{\theta_1}{2}\right)\cos\left(\varepsilon\ln(r_1)\right) + P_{12}\sin\left(\frac{\theta_1}{2}\right)\sin\left(\varepsilon\ln(r_1)\right)\right\}$$

$$+\frac{K_2^d C}{\sqrt{2\pi r}}\left\{-P_{11}\cos\left(\frac{\theta_1}{2}\right)\sin\left(\varepsilon \ln(r_1)\right)+P_{12}\sin\left(\frac{\theta_1}{2}\right)\cos\left(\varepsilon \ln(r_1)\right)\right\}, \quad (3.6)$$

where

$$C=\frac{2\left(\alpha_1^2-\alpha_s^2\right)}{D\cosh(\pi\varepsilon)},$$

$$D=4\alpha_1\alpha_s-\left(1+\alpha_s^2\right)^2,$$

and P_{11} and P_{12} are functions of crack tip speed and material properties given in the appendix. The quantities α_1, α_s, r_1 and θ_1 have been defined in section 3.2.1. This is the same expression as (3.4) but has a linear dependence on coefficients K_1^d and K_2^d The quantity χ^2 to be minimized is given by,

$$\chi^2=\sum_{i=1}^{N}\left[f_i-\hat{f}\left(r_i,\theta_i;K_1^d,K_2^d\right)\right]^2. \quad (3.7)$$

In the above, N is the number of data points to be fitted, $f_i=np/ch\Delta$ is the measured stress gradient at each point with coordinates r_i, θ_i, centered at the current crack tip. Function $\hat{f}$ contains K_1^d and K_2^d as parameters which are evaluated by minimizing (3.7) with respect to themselves. When fitting the expression for a transient higher order stress field, $\hat{f}$ becomes equivalent to equation (3.5). The least squares fit is still linear, but 28 constants, A_0, A_1, A_t ..., need to be fitted. Otherwise the procedure is identical.

Values of r_i, θ_i from each interferogram are obtained by digitizing the fringe pattern. Digitization is done by hand using a digitizing tablet connected to a computer. The centerline of each fringe on the image is digitized. Both bright and dark fringes are traced so the value of the fringe order n in f_i ranges in 0, ±1/2, ±1, ±3/2... . By digitizing both bright and dark fringes we double the number of available data points, which aids the accuracy of the fitting procedure. Unfortunately the sign of each fringe is undetermined by

simply observing the interferogram. This is a problem with all full field interferometric techniques. External information has to be employed to determine whether a particular lobe of the CGS pattern represents an increase or decrease in stress. Recall that the CGS optical technique provides us with contours of constant stress gradient. By assuming that the opening stresses in front of the crack tip have large positive values, then we can deduce the sign of each lobe of the fringe pattern. The direction of optical differentiation in all experiments was the x_1 axis. As we approach the tip along the x_1 axis from -∞ stress has to increase, which means a positive gradient. As we move away from the tip to +∞ stress decays to zero. This specifies one positive and one negative lobe for each fringe pattern. The zero stress region surrounding the fringe pattern is seen as the undisturbed portion of the laser beam. In this region $n=0$.

Both stress fields shown earlier (equations (3.4) and (3.5)) were derived under the assumption of two-dimensional plane stress conditions. In addition, the interference condition, equation (2.11), governing the CGS interferometer has been derived assuming plane stress conditions. When analyzing optical data, therefore, care must be taken to use only data points r_i, θ_i from a region of the specimen that does indeed approximate two-dimensional plane stress conditions. The region in which such conditions are valid in a three point bend bimaterial specimen was determined by a numerical analysis of Lee and Rosakis (1992) presented earlier in section 2.1.1. In figure 6 a plot indicating the extent of the three-dimensional zone was presented. For data analysis purposes the predicted three-dimensional zone was approximated as shown schematically in figure 24. Only data points r_i, θ_i outside this region were used. Also no points outside a circle or radius $r=1.1h$, h specimen thickness, were considered in order to avoid far field effects.

By taking points outside the predicted three-dimensional deformation zone we are allowed to use a two-dimensional plane stress representation to fit the data. After minimization of χ^2, the quality of each fit is judged by the average percentage error between the experimental data points f_i and the corresponding value of $\hat{f}(r,\theta;K_1,K_2)$. This

measure of error was seen to be equivalent to the quantity χ^2/N. In addition we can visually observe how accurate a fit is by how well the fit predicted fringe pattern follows the experimentally obtained fringe pattern from which it was derived. Examples of this procedure are shown in the next section.

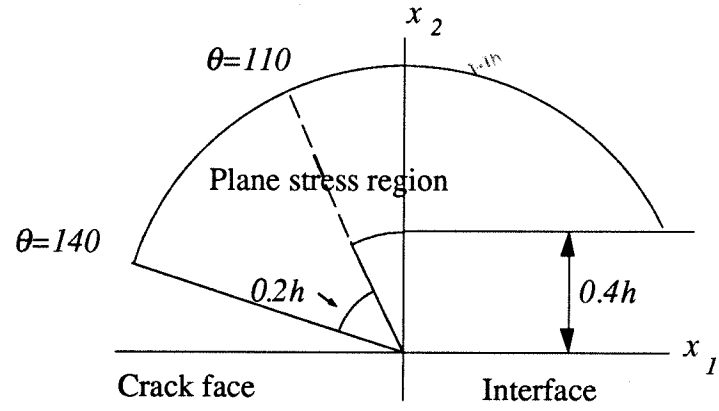

Figure 24: Idealization of plane stress region for data analysis purposes.

Let us note in passing that equation (1.2), the quasi-static interfacial stress field of Rice (1988), is used to fit interferograms at times before crack tip initiation. The fitting procedure is again exactly the same only $\hat{f}$ is given by equation (1.2).

3.3 Analysis of experimental data

3.3.1 Importance of transient effects

The asymptotic result of equation (3.4) was derived under the assumption of steady-state conditions. These conditions are clearly violated in the early stages of dynamic interfacial crack growth experiments as is evident from the large initial accelerations seen in figure 18 and 19. One would therefore expect that in the regime for times close to $t=0\mu s$, equation (3.5), the higher order transient stress field, would better approximate the actual stress field in the specimen. By observing equation (3.5) we see that the term of order

$r_1^{1/2}(\ln r)^2$ is multiplied by the rate of change of the oscillatory index $\dot{\varepsilon}(=\varepsilon'(v)\dot{v})$. The term of order $r_1^{1/2}(\ln r)^2$ is the most dominant transient term for small distances away from the crack tip, but if $\dot{\varepsilon}$ is close to zero, it may be less important than the other higher order terms. It was thus proposed in section 3.2.2 that $\dot{\varepsilon}$ could be considered a partial measure of transience around the propagating crack tip since it controls the relative importance of the most dominant transient term in equation (3.5). An example of the variation of ε and $\dot{\varepsilon}$ with time for a typical drop weight tower one point bend test is shown in figures 25(a,b). This is for the PMMA/steel test shown in figure 17. In figure 25(b), $\dot{\varepsilon}$ exhibits a local maximum at about $t=10\mu s$ after initiation. It then starts increasing again after 25μs. At short times after initiation, $\varepsilon'(v)$ is close to zero although $\dot{v}$ is large ($10^7 g$). This accounts for the initially low values of $\dot{\varepsilon}$. At later times ($t>25\mu s$) and as the crack tip velocity approaches the Rayleigh wave speed of PMMA, $\dot{\varepsilon}$ increases again.

To demonstrate the phenomenon of the existence of highly transient effects in some of the experimental data, let us now attempt to analyze the frame of figure 17 at t=9.5μs. This corresponds to a local maximum value of $\dot{\varepsilon}$ in this particular test. By following the fitting procedure described in section 3.2.3, we can obtain the coefficients of either equation (3.4) or equation (3.5). The result of such a fit for the K^d-dominant field (equation (3.4)) is shown in figure 26(a). The diamonds are digitized data points from the interferogram at t=9.5μs. The solid line is the contour of the quantity $\partial(\hat{\sigma}_{11}+\hat{\sigma}_{22})/\partial x_1$ calculated numerically by using the results for K^d from the fit generated by the same data points. As can be clearly seen, equation (3.4) cannot represent the data to any reasonable extent. The deformation of field of this particular picture therefore is nowhere near K^d-dominant. The result of the fit of the transient higher order field (equation (3.5) derived earlier is shown in figure 26(b). The data points are exactly the same as before and the solid line is the result of the fit. The fit is very good over a large area of the specimen. All features of the field are successfully captured by equation (3.5). This shows that the K^d-dominant analysis cannot be used for cases were $\dot{\varepsilon}$ is high.

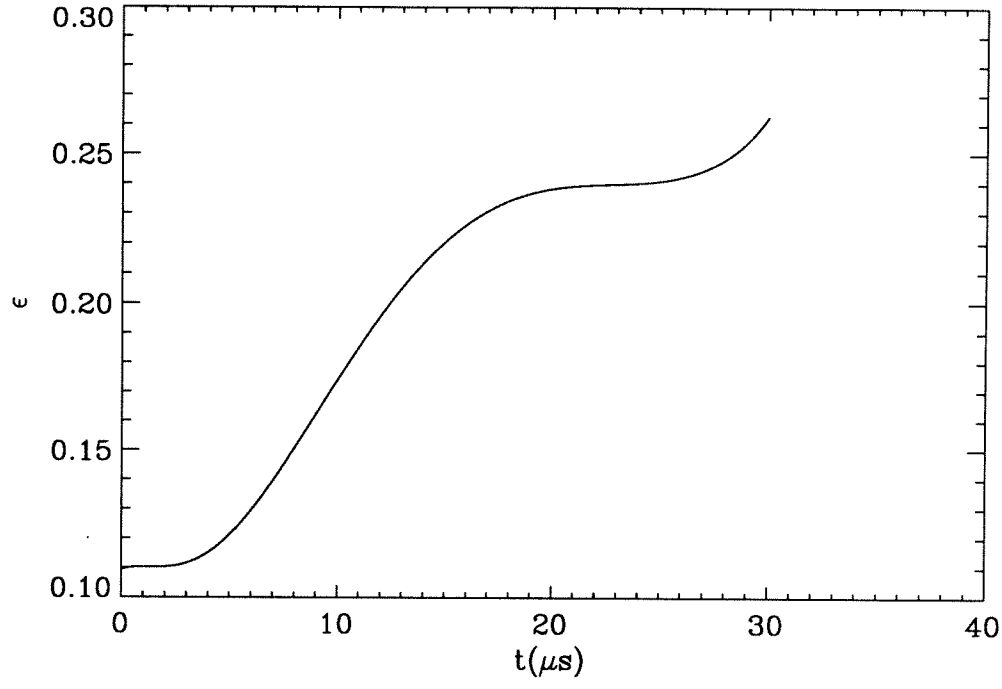

(a)

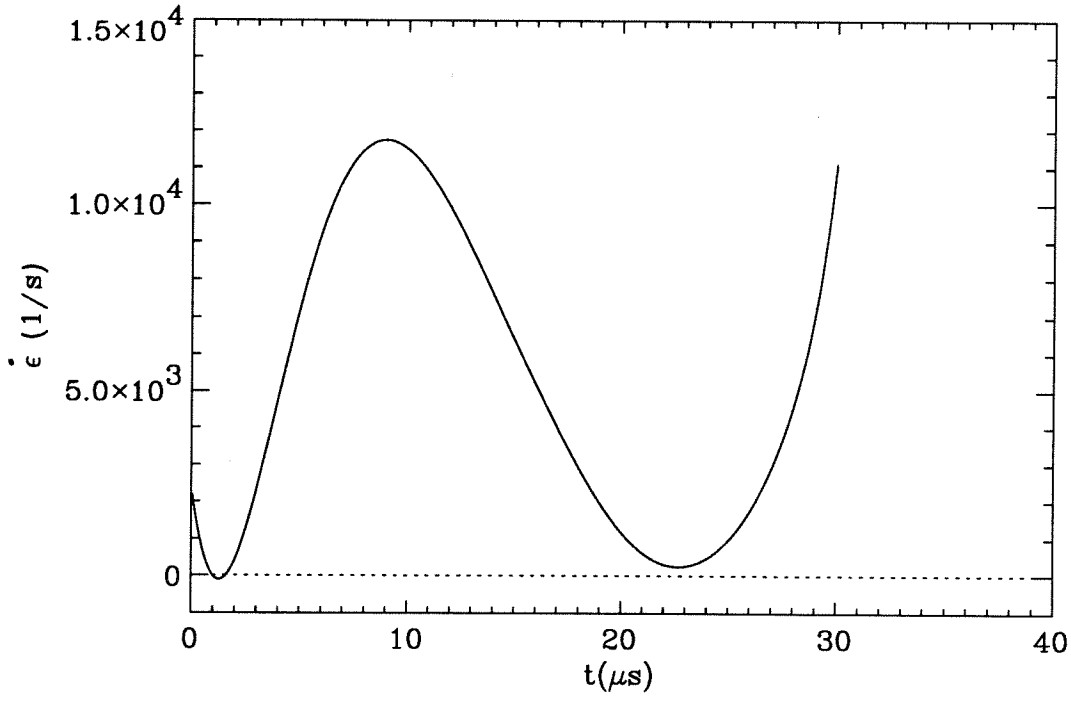

(b)

Figure 25: Time histories of oscillatory index ε, (a), and its time derivative, (b), for the experiment shown in figure 17.

To further investigate the effect of $\dot{\varepsilon}$ on the interpretation of optical data, we choose to analyze an interferogram corresponding to the minimum value of $\dot{\varepsilon}$ within the duration of this particular test. This occurs at $t=23\mu s$. Figure 27(a) shows the result of the K^d-dominant fit to the experimental data. As the crack tip is approached, equation (3.4) seems to adequately describe the experimental measurement. However as the distance from the crack tip is increased, K^d-dominance is lost. Nevertheless, the lack of K^d-dominance in figure 27(a) ($\dot{\varepsilon}\sim1.0\text{x}10^2\text{s}^{-1}$) is not as dramatic as in figure 26(a) ($\dot{\varepsilon}\sim1.2\text{x}10^4\text{s}^{-1}$). Figure 27(b) shows the result of the fit of the transient higher order field to the same experimental data points as in figure 27(a). The fit is now much better over the whole range of radii since higher order terms have been included. These terms are more important further away from the crack tip where the effect of the most singular term has decayed. A second example of the region of K^d-dominance in a particular interferogram at a low value of $\dot{\varepsilon}$ is shown in figure 28. It is clear once again that a K^d-dominant field seems to exist at radii close to the crack tip ($r<0.5h$).

Qualitatively similar results were obtained when analyzing experiments performed using gas gun impact. Figure 29 shows the extent of K^d-dominance in the interferogram corresponding to $t=8\mu s$ in figure 14. As can be seen only the innermost fringes are well described by the K^d-dominant approximation. To well describe the whole fringe pattern we have to make use of the higher order analysis. The result of the higher order transient fit for the same interferogram ($t=8\mu s$ in figure 14) is shown in figure 30. Here the white lines,

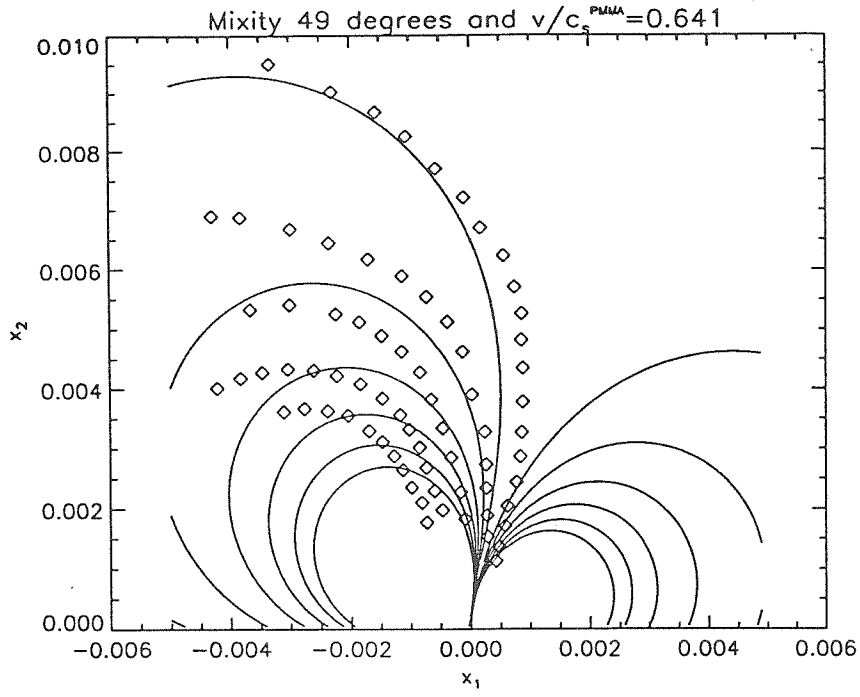

(a)

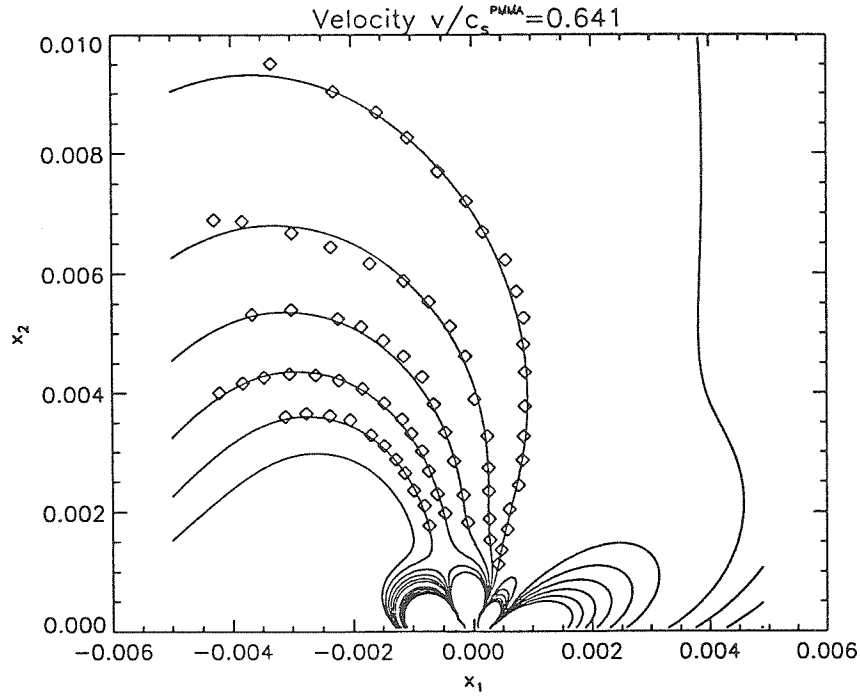

(b)

Figure 26: Comparison of digitized data points from the frame corresponding to t=9.5μs in figure 17 with, (a) a K^d-dominant fit, equation (3.4), (b) a higher order fit, equation (3.5). (Crack lies on negative x_1 axis.)

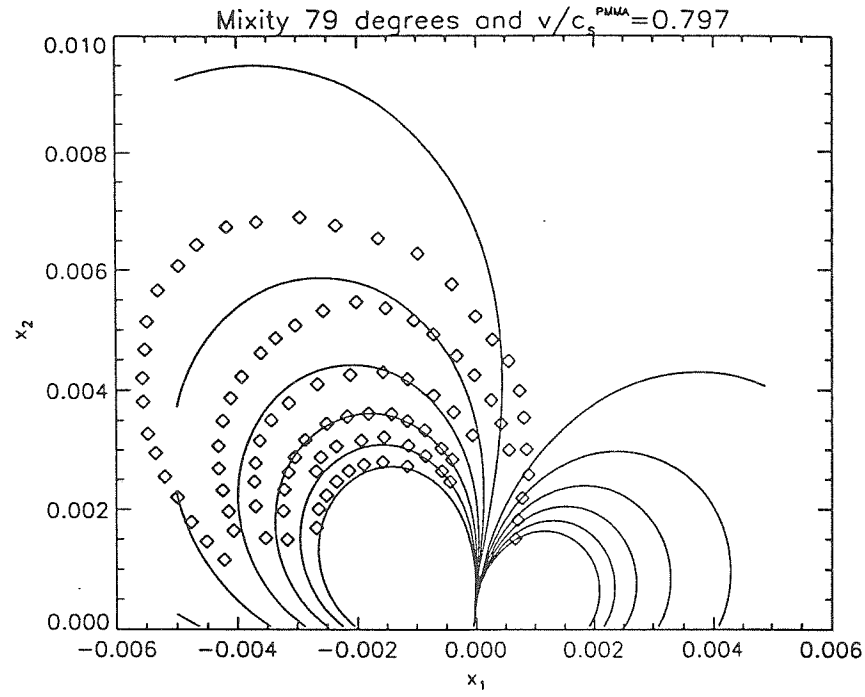

(a)

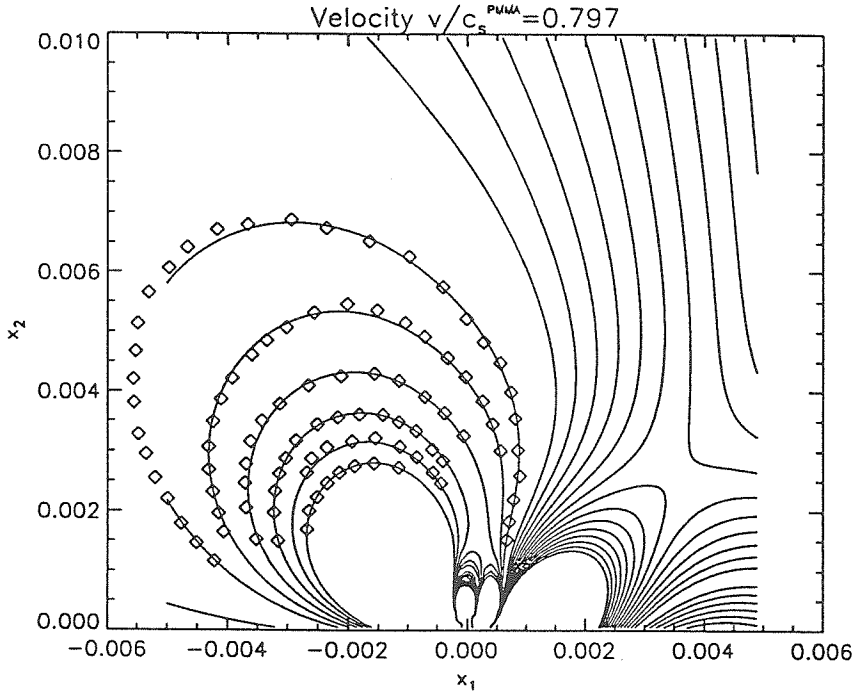

(b)

Figure 27: Comparison of digitized data points from the frame corresponding to t=23μs in figure 17 with, (a) a K^d-dominant fit, equation (3.4), (b) a higher order fit, equation (3.5). (Crack lies on negative x_1 axis.)

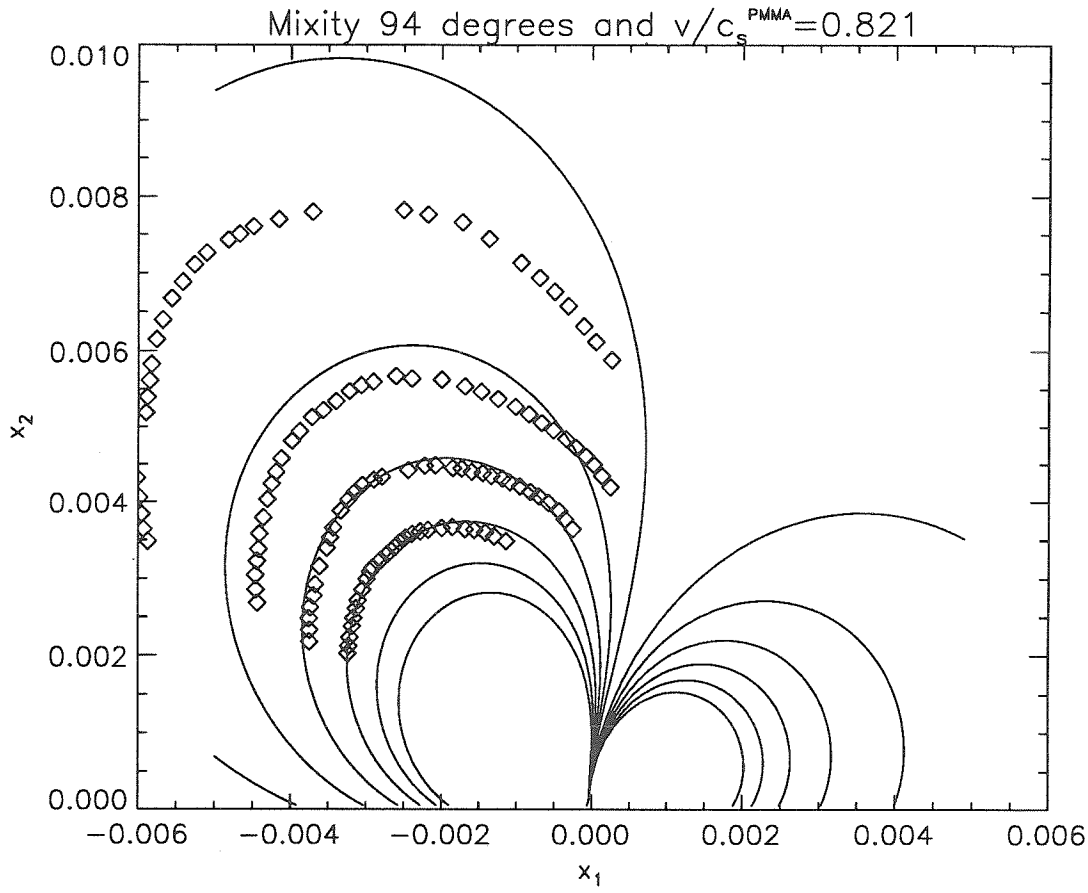

Figure 28: Comparison of digitized data points from an interferogram at t=20μs in figure 17 (not shown) with a K^d-dominant fit. (Crack lies on negative x_1 axis.)

obtained from plotting the field of equation (3.5) using the values of the fitted parameters, are superposed on the actual picture (instead of the digitized points as in figures 26 and 27).

The above discussion points to the following conclusions : Interferograms corresponding to times that are close to the maximum value of $\dot{\varepsilon}$, clearly show the effect of transience on the near tip deformations. No region of K^d-dominance can be found anywhere around the crack tip in such cases. When $\dot{\varepsilon}$ is minimum there is a region close to the crack tip that is well characterized by a K^d-dominant stress field. In these cases a higher

order analysis is helpful only in fitting the fringe pattern outside the region of K^d-dominance.

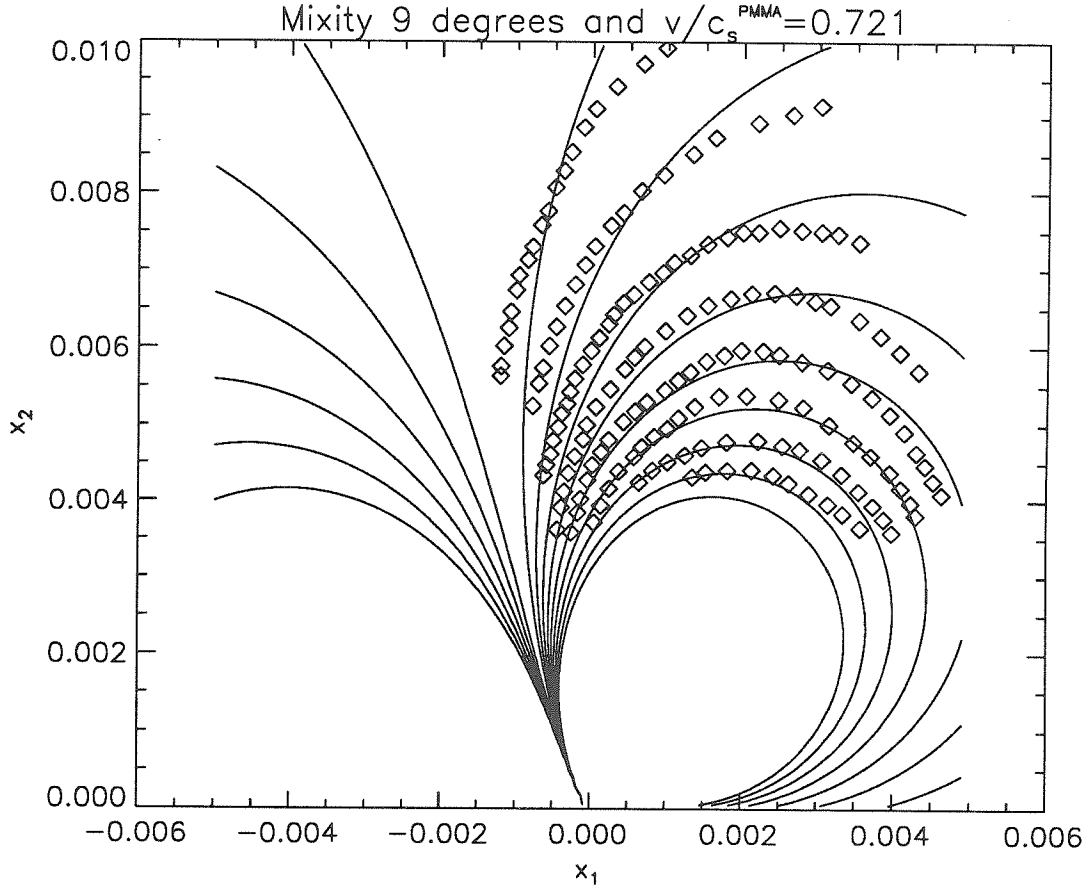

Figure 29: Comparison of digitized data points from an interferogram to t=8μs in figure 14 with a K^d-dominant fit. (Crack lies on negative x_1 axis.)

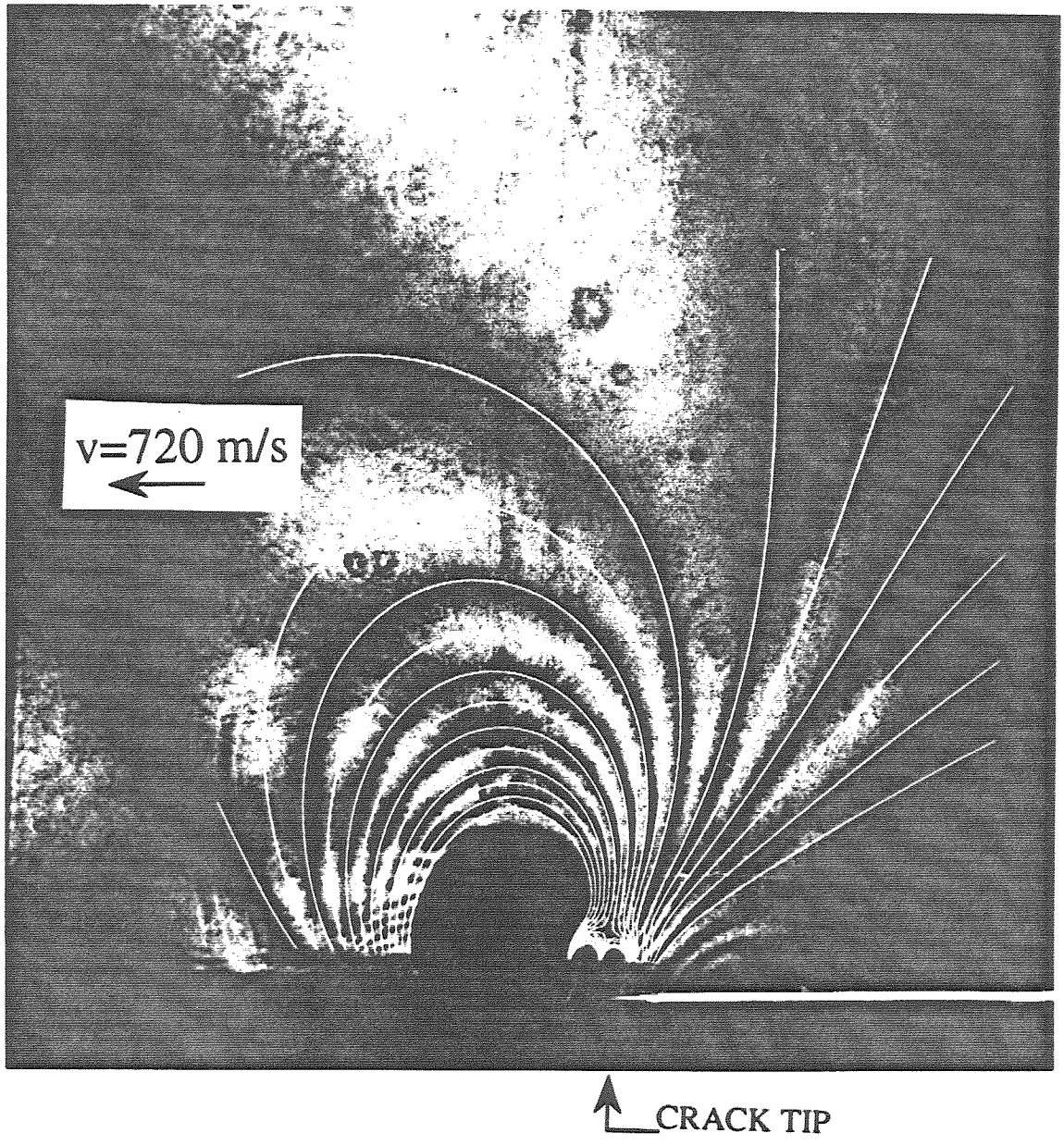

Figure 30: Comparison between the CGS fringe pattern and the fitted higher order transient stress field, equation (3.5), for a crack propagating in a PMMA/steel interface.

3.3.2 History of fracture parameters

The main goal of this research project is to identify a physically meaningful and accurate criterion governing dynamic crack propagation along bimaterial interfaces. Traditionally, for historical reasons and engineering applicability, dynamic fracture criteria in homogeneous materials have been formulated in terms of the homogeneous stress intensity factor K_I (Kanninen and Popelar (1985), Freund (1990)). Also initiation criteria for bimaterial cracks have been based on the energy release rate G and phase angle ϕ of a K-dominant field, as explained in section 1.2. (No criterion has ever been proposed for dynamic crack growth in bimaterials.) To be able to compare with these results we shall also attempt formulation of a dynamic propagation criterion using the results of the dynamic complex stress intensity factor K^d. To use K^d as a fitting parameter of the interferograms it is necessary to make sure that during the fracture event a substantial K^d-dominant region exists around the propagating crack tip. For this reason, all results presented in this section, and used in chapter 4 to determine a fracture criterion, are from interferograms in which a K^d-dominant region could be established. Data from interferograms which involve very high transient effects are ignored in obtaining values of K^d. Nevertheless an attempt is made to propose a dynamic fracture criterion that is physically based. It will then be possible to apply the criterion in cases were K^d-dominace cannot be established. For further discussion on this issue see section 4.2.

The variation of stress intensity factors K_1^d and K_2^d for the PMMA/steel drop weight tower test presented in figure 17, are shown in figures 31(a,b). The energy release rate G and phase angle ϕ for the same test are shown in figures 32(a,b). G for the case of dynamic interfacial crack growth is given by (Yang et al. (1991)),

$$G = \frac{F}{4\mu_1}|K|^2, \tag{3.8}$$

where F is a function of velocity and bimaterial system material properties shown explicitly in the appendix. Note that F is finite at the Rayleigh wave speed of Plexiglas. Equation (3.8) is analogous to the quasi-static result seen in equation (1.8). The phase angle in figure 32(b) has been calculated from

$$\phi = tan^{-1}\left(\frac{K_2}{K_1}\right). \tag{3.9}$$

This implies that a length scale of 1m has been used in this particular plot. The phase angle ranges from $-\pi$ to π to cover all possible sign combinations of K_1 and K_2.

On all plots in figures 31 and 32 $t=0\mu s$ corresponds to the estimated time of crack initiation. Pre-initiation values of K_1^d and K_2^d were determined by fitting the quasi-static stress field of equation (1.2) to interferograms before $t=0\mu s$. Again only results from pictures that exhibited K^d-dominance are shown. Unfortunately determining the time of initiation in each test is not an absolute science. It was observed that when fitting a K^d-field to pictures a few microseconds after $t=0\mu s$ the fit was good only on the outer most fringes. This is contrary to what would be expected at first glance, on the basis of asymptotics. An example of such a case is shown in figure 33 for the interferogram corresponding to $t=2\mu s$ for the experiment shown in figure 17. It can be seen that the three outer fringes are in very good agreement with the K^d-dominant fit, while the inside fringes are not. Gradually as time progressed (2-10μs) the quality of the fit deteriorated from the inside out until all K^d-dominance was lost. This occurred when $\dot{\varepsilon}$ was a maximum and it is this particular effect that was illustrated in the previous section. The gradual collapse of the K^d-field between pictures agreed reasonably well timewise with a dilatational wave being emitted from the crack tip and traveling radially outwards. Such waves would indeed start being emitted when the crack tip initiated. They would travel

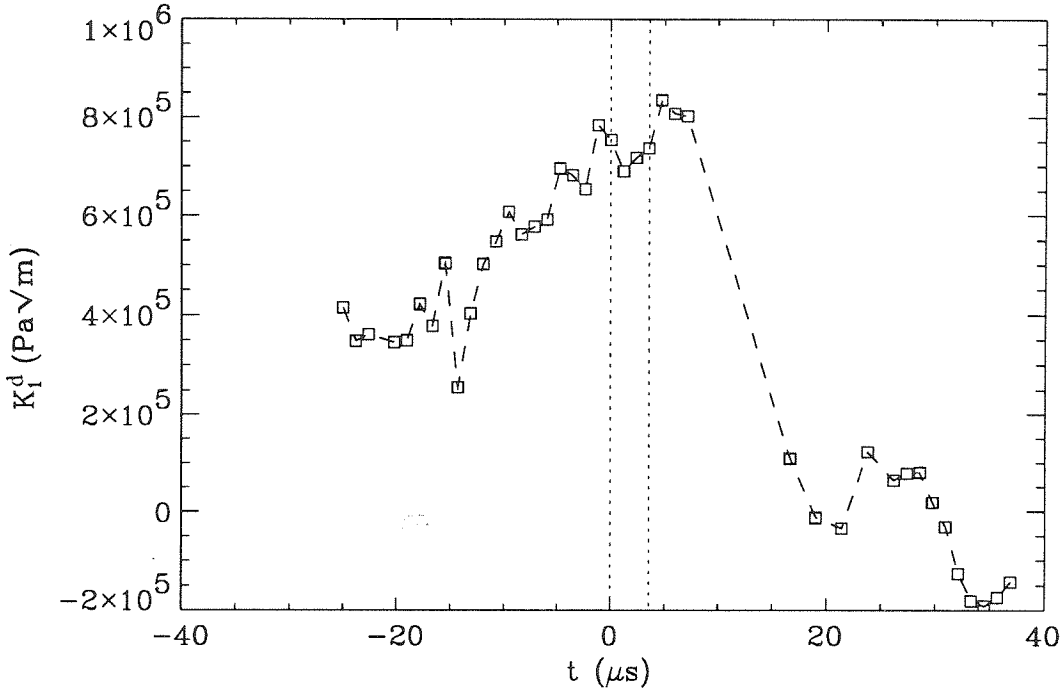

(a)

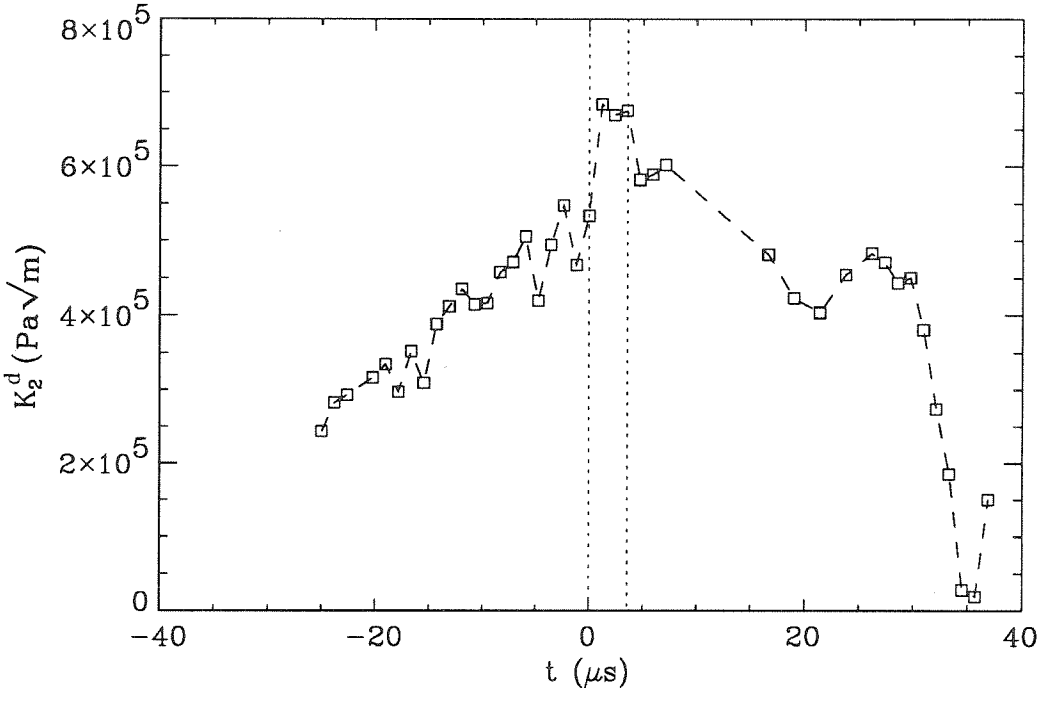

(b)

Figure 31(a,b): Time history of components of complex stress intensity factor for the experiment shown in figure 17.

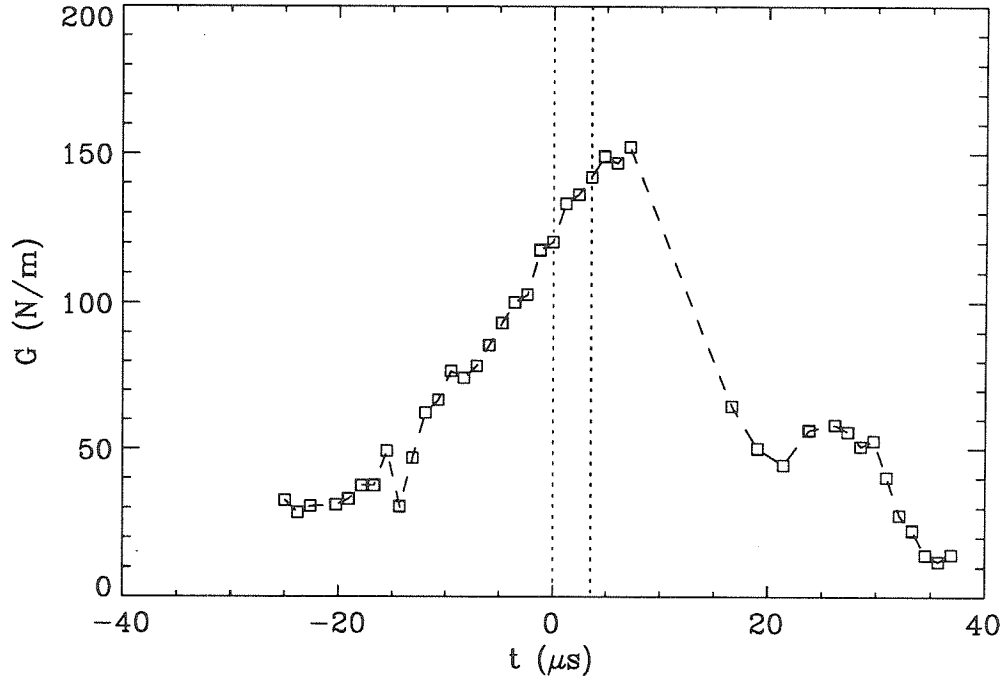

(a)

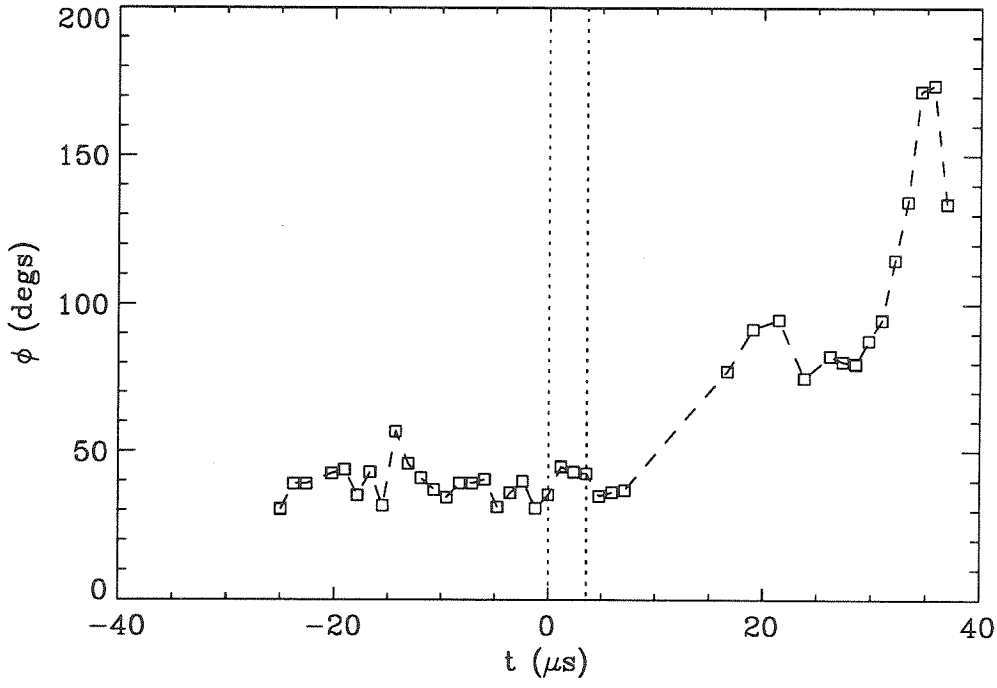

(b)

Figure 32(a,b): Time history of energy release rate and phase angle (L=1m) for the experiment shown in figure 17.

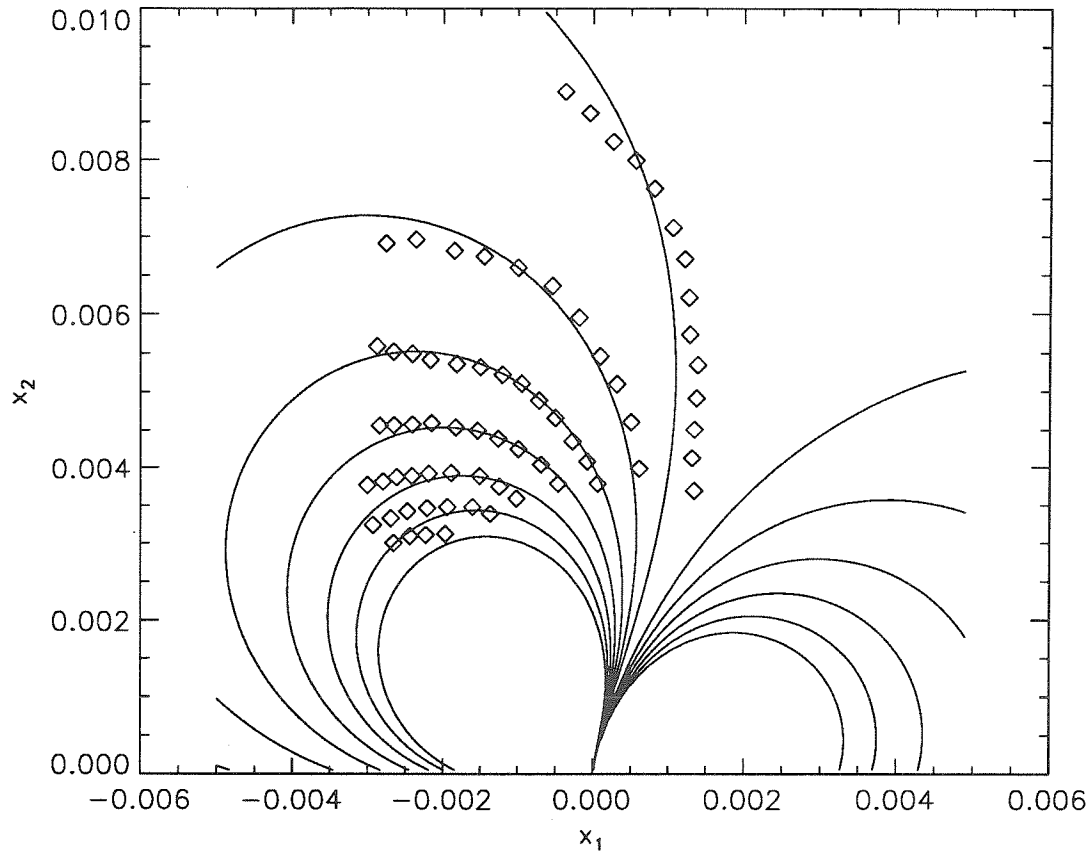

Figure 33: Illustration of collapse of K^d-field in inner fringes at times slightly after initiation.

outwards and destroy the K^d-field that was established in the pre-initiation stages of the experiment. It was possible to determine the time of initiation by choosing the interferogram immediately before the first sign that the innermost fringe did not conform to a K^d-dominant field, i.e., just before the emission of a wave from the crack tip. Even so there is some uncertainty in the exact time of crack initiation, based on when the crack is visually seen to propagate. This uncertainty is represented in figure 31 and 32 as being between the two dotted vertical lines.

It can be seen in figure 31(a,b) that both K_1^d and K_2^d increase to a maximum value and then sharply drop, with K_1^d attaining negative values towards the end of the test. Note

that the gap of data points in the curves of figures 31 and 32 corresponds to the region in which transient effects are dominant. No K^d-dominant results are available for those times. The energy release rate (figure 32(a)) also increases to a peak a little after $t=0\mu s$ and then drops to a value close to zero implying that the process of dynamic crack propagation along interfaces is highly unstable, at least in the particular experimental configurations and loading rates used in this study. This result is corroborated by the steep rise of the crack tip speed in very short times. It will be elaborated on further in chapter 4. On the other hand the phase angle ϕ increases throughout the test. The change in phase angle can be expected simply by looking at the dynamic interferograms. It was pointed out in section 3.1.1 that the CGS fringe pattern surrounding the propagating crack tip does not change much with time either in size or orientation, for the drop weight tower tests. This was clearly illustrated in figure 11. In figure 23 it was seen that the theoretically predicted fringe pattern from the Yang et al. (1991) K^d-dominant field rotates if the crack-tip speed v changes, but $|K^d|$ and ϕ remain fixed. Both the ϕ and v affect the orientation of the stress field as seen in the argument of the sines and cosines in equation (3.4). We have seen experimentally that v changes with time. Thus the phase angle ϕ has to vary in such a way so as to keep the fringe pattern the same throughout propagation. In effect the variation of ϕ cancels the influence the changing v has on the fringe pattern. *The link between the variations of* v *and* ϕ *will be used in the next chapter to propose a dynamic crack growth criterion.*

Because of the presence of oscillatory terms in the stress field shown in equation (3.2) all inconsistencies associated with the theory of static linear elastic interfacial mechanics are still present. Of paramount importance is the inconsistency of predicted interpenetration of the crack faces. The extent of the resulting contact zone is given by,

$$r_c = e^{\frac{-\pi/2-\phi+\tan^{-1}(2\varepsilon)}{\varepsilon}}. \qquad (3.10)$$

This is the same equation as (1.5) for the static case, but with ϕ and ε changing with velocity. To accept the measured values of G and ϕ as accurate we must make sure that the extent of predicted contact is much smaller than the smallest characteristic length of the problem and is embedded in the three-dimensional region of deformation. Only in that case can the K^d-field surrounding the crack tip control the fracture process. From figure 21, which shows the variation of ε with crack tip speed for a PMMA/steel system, it can be seen that as $v \rightarrow c_R^{PMMA}$, $\varepsilon \rightarrow +\infty$. As v, and consequently ε, gets larger it would seem that the predicted contact zone r_c would become unacceptably large. When calculating r_c though from experimental measurements it was found that the variation of ϕ suppressed the increase of the contact zone size keeping it at very low values for all but the highest crack tip velocities. An idea of the size of the contact zone predicted for a one point bend PMMA/steel test is given in figure 34. The solid lines are contours of constant contact zone size as derived from equation (3.10) for a range of v and ϕ. The diamond points are the calculated results from three nominally identical PMMA/steel one point bend drop weight tower tests (one of which was illustrated in figure 17). Clearly values of the contact zone are below 10^{-4}m. This is well within the zone of three-dimensional deformation surrounding the crack tip whose maximum extent is around 2mm.

Very similar results are obtained when analyzing the interferograms shown in figure 11. These are from a three point bend PMMA/aluminum experiment. The variation of G and ϕ with time for the propagation part of this experiment are shown in figures 35(a,b). The general trends are similar to those obtained before. The contact zone resulting from this test is shown in figure 36. It can be seen that in this case the predicted contact zone is less than 10^{-8}m, which makes the fitted values of K^d acceptable.

Results from air gun experiments, which are primarily shear dominated, provide a slightly different picture. The variations of G and ϕ with time for the subsonic regime of the test shown in figure 14 are depicted in figures 37(a,b). The main difference of these results and those in figure 32 is the fact that negative phase angles are attained at the beginning of

the propagation part of the air gun experiments. This denotes a more shear dominated stress field. In addition much larger values of energy release rate are observed, which implies that to maintain growth at these phase angles a large amount of energy is required.

All the above results will be used in chapter 4 to formulate a phenomenological criterion for dynamic crack growth along bimaterial interfaces.

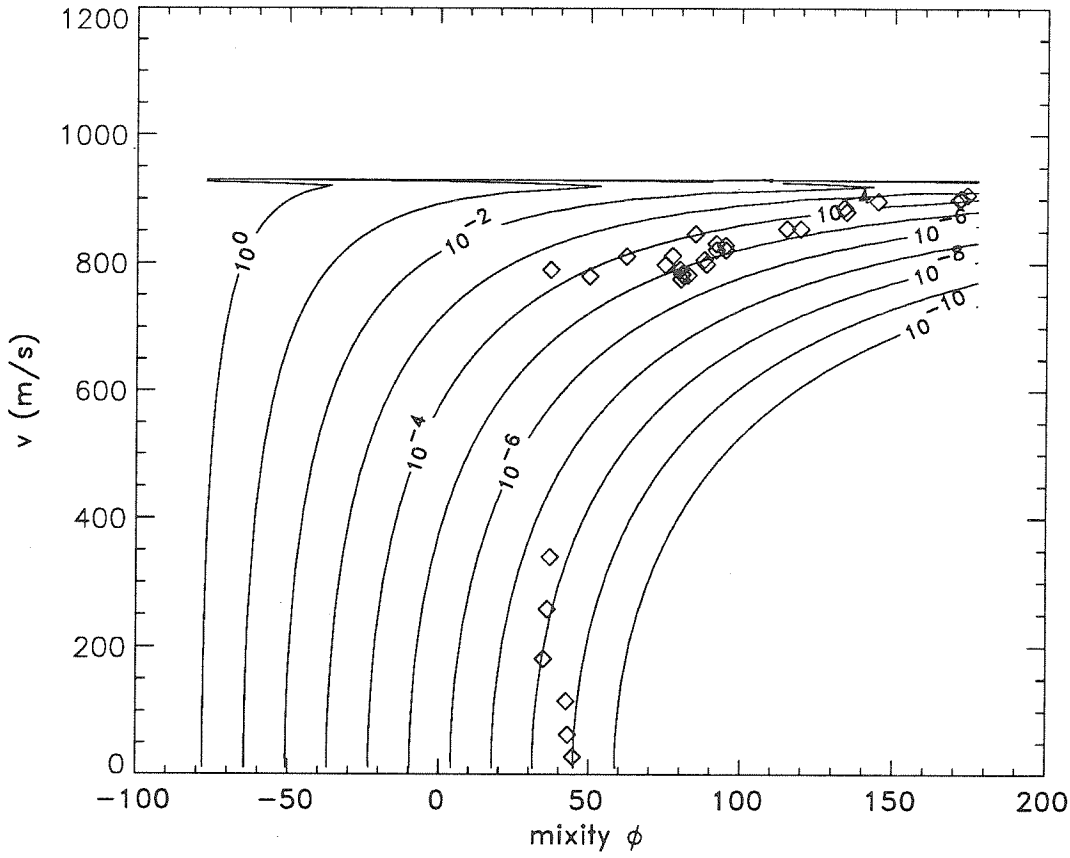

Figure 34: Magnitude of predicted contact zone in PMMA/steel one point bend drop weight tower experiments.

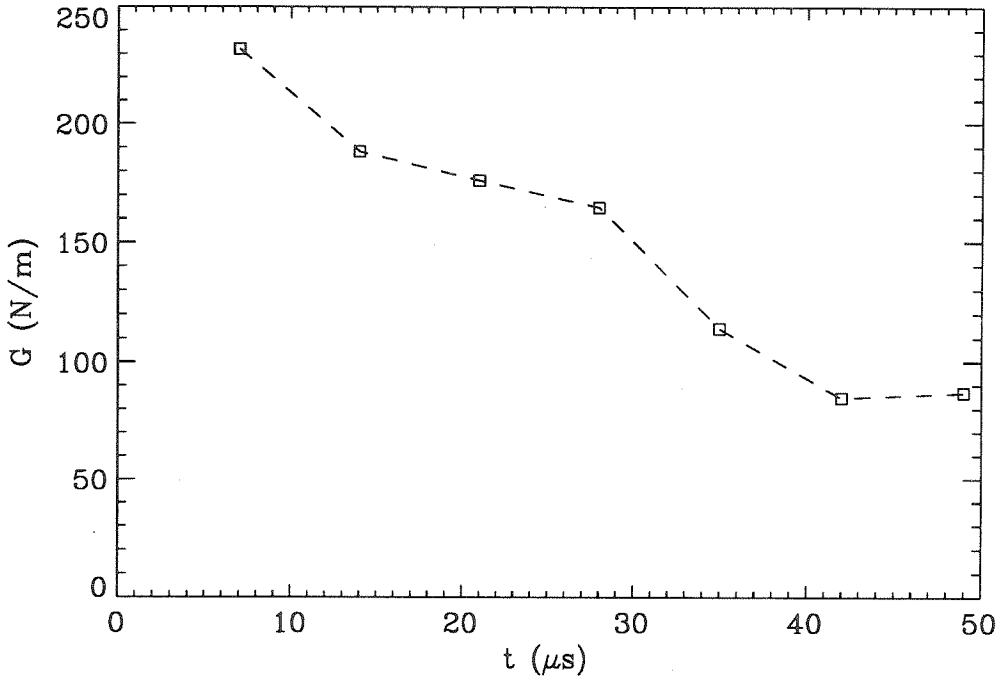

(a)

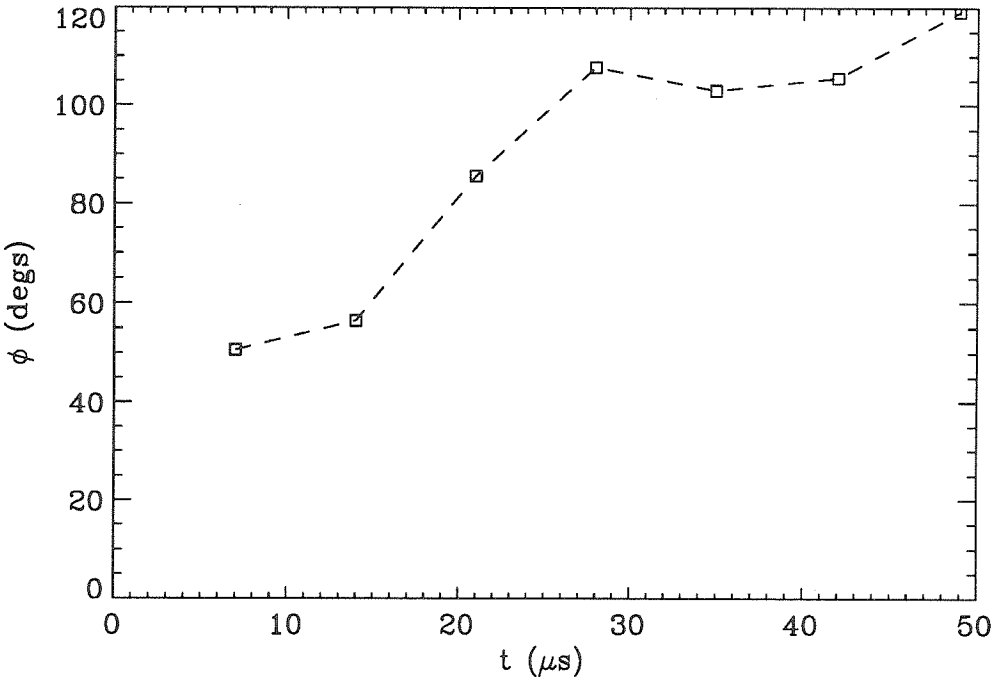

(b)

Figure 35(a,b): Time history of energy release rate and phase angle (L=1m) for the experiment shown in figure 11.

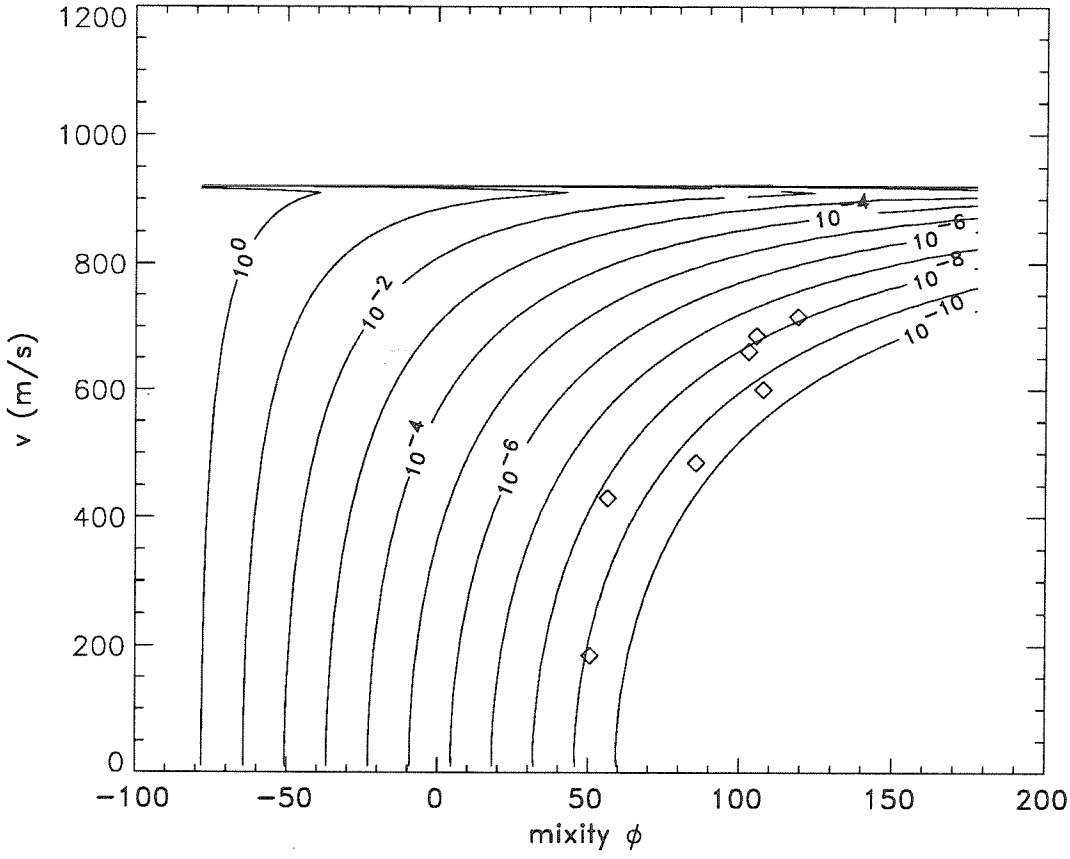

Figure 36: Magnitude of predicted contact zone in PMMA/aluminum three point bend drop weight tower experiment.

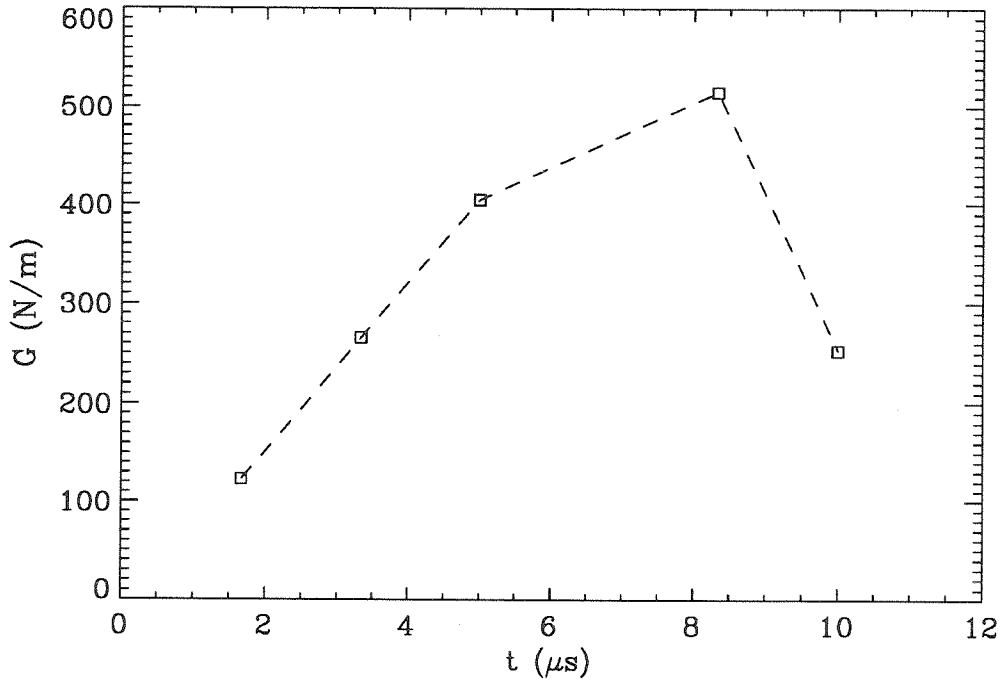

(a)

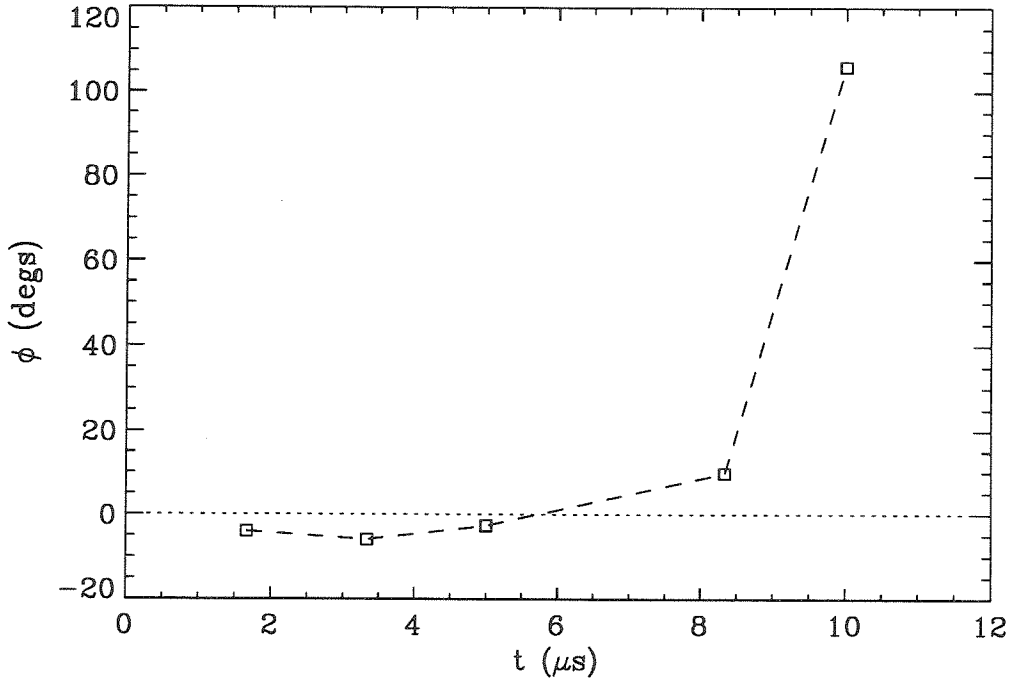

(b)

Figure 37(a,b): Time history of energy release rate and phase angle (L=1m) for the experiment shown in figure 17.

CHAPTER 4

A CRITERION FOR DYNAMIC INTERFACIAL CRACK GROWTH

Using the procedure described in chapter 3 several drop weight tower tests (low loading rate) and several air gun tests (high loading rate) were analyzed. Based on the results of those tests, in this chapter we shall proceed to formulate a dynamic fracture criterion for interfacial crack growth. In section 4.1 some experimental observations are made that lead to the formulation of the proposed criterion. In section 4.2 the results are critically discussed and evaluated.

4.1 Proposed fracture criterion based on crack face profile

A sequence of dynamic interferograms obtained from the tip of a crack lying along a PMMA/aluminum interface was shown in figure 16. Pre- and post- initiation pictures were shown. As was pointed out in section 3.1.1, before crack initiation ($t<0\mu s$) the fringe pattern around the tip changes both in size and orientation, denoting a change in the energy release rate G and phase angle ϕ. A variation was indeed seen in the measured values of G and ϕ at times before $t=0\mu s$, for the PMMA/steel drop weight tower test seen in figure 32. In contrast, after initiation, the fringe pattern surrounding the crack does not change significantly with time. This effect is seen in more detail in the interferograms presented in figure 11 which correspond only to the crack propagation phase of a drop weight tower test. As discussed in section 3.1.1, the implication of this visual observation is that some fundamental physical quantity, such as stress or crack opening displacement, must remain

constant throughout the crack growth phase. It has already been established in chapter 3 that v, ϕ and G (or $|K^d|$) all vary considerably during crack growth. Therefore, if we wish to mathematically model the fact that the fringe pattern during crack growth does not change, we must employ some *combination* of these three quantities that remains constant.

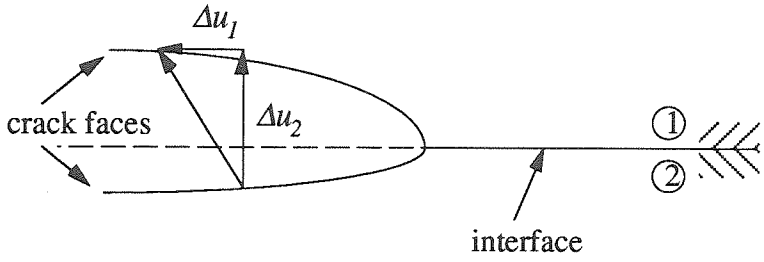

Figure 38: Schematic definition of opening and shearing displacements behind the interfacial crack tip.

It was seen from figure 34 in section 3.3.2 that the variations of v and ϕ were such as to keep the size of the predicted contact zone small throughout each test. This suggests that there is a separate link between v and ϕ during crack growth. In figure 34 it is clearly visible that the diamond points (corresponding to experimental results) curve to the right, denoting an increase in both v and ϕ as the crack grows. We intend to investigate whether the particular variation of v and ϕ in each experiment occurs in such a manner so as to maintain some fundamental quantity constant. A candidate for such a quantity would be something that does not involve $|K^d|$. We will look into the ratio of the opening (Δu_2) to shearing (Δu_1) displacements behind the crack tip as one possible candidate. With reference to the geometry of figure 1 Δu_1 and Δu_2 are defined as

$$\Delta u_\alpha(r) = u_\alpha(r,\theta=+\pi) - u_\alpha(r,\theta=-\pi), \quad \alpha = 1,2, \tag{4.1}$$

where $u_\alpha(r,\theta)$ is the displacement field surrounding the crack tip. Figure 38 shows a geometrical representation of Δu_1 and Δu_2 behind the crack tip. A positive Δu_2 means an

opening displacement, and a positive Δu_1 represents sliding of material-1 along the positive x_1 axis. From the asymptotic analysis of Yang et al. (1991), the crack face displacements are given by,

$$\Delta u_1(r) = \frac{H_{22}}{\cosh(\pi\varepsilon)}\sqrt{\frac{2r}{\pi}}\frac{|K^d|}{\sqrt{1+4\varepsilon^2}}\frac{1}{\eta}\sin\left(\phi + \varepsilon \ln r - \tan^{-1}(2\varepsilon)\right),$$

and (4.2)

$$\Delta u_2(r) = \frac{H_{22}}{\cosh(\pi\varepsilon)}\sqrt{\frac{2r}{\pi}}\frac{|K^d|}{\sqrt{1+4\varepsilon^2}}\cos\left(\phi + \varepsilon \ln r - \tan^{-1}(2\varepsilon)\right).$$

Quantities ε and η have been previously defined (section 3.2) and the function H_{22} is given in the appendix. Each of the two displacements in equation (4.2) depends on $|K^d|$, but their ratio is only a function of v and ϕ. It is given by,

$$\frac{\Delta u_1}{\Delta u_2}(r) = \frac{1}{\eta}\tan\left(\phi + \varepsilon \ln r - \tan^{-1}(2\varepsilon)\right). \tag{4.3}$$

If we assume that throughout propagation this ratio remains constant, say at a value C_1, at a fixed distance, say a, behind the crack tip, then equation (4.3) defines a single line in the v, ϕ plane. The equation of this line is given by,

$$\left.\frac{\Delta u_1}{\Delta u_2}\right|_{r=a} = C_1 = \frac{1}{\eta}\tan\left(\phi + \varepsilon \ln a - \tan^{-1}(2\varepsilon)\right),$$

or solving for ϕ,

$$\phi = \tan^{-1}(\eta C_1) + \tan^{-1}(2\varepsilon) - \varepsilon \ln a. \tag{4.4}$$

The dependence of ϕ on v comes in through the velocity dependence of the oscillatory index ε and the traction resolution factor η. (See figures 21 and 22 for the variation of ε and η with v respectively.)

Experimental data of v and ϕ have been obtained from a series of experiments using the data analysis procedure described in section 3. In figure 39, which is a plot in the (ϕ, v) plane, the experimental results of the measured crack tip speed v and calculated phase angle ϕ are shown as diamonds. These results are from three nominally identical PMMA/steel one point bend experiments conducted under drop weight tower impact at 4m/s. One of these three tests is the one for which results of K_1^d and K_2^d, G and ϕ were presented in figures 31 and 32. The solid line in figure 39 represents the curve given by equation (4.4) that best fits the experimental values. It was decided to evaluate equation (4.4) at a distance $a=2mm$, which is approximately the innermost radius of the region of K^d-dominance observed in most interferograms. This means that it is also the point closest to the crack tip where equation (4.4) is valid. The computed ratio $\Delta u_1/\Delta u_2$ for this fit is $C_1=-0.3$. From figure 39 it seems that indeed throughout crack propagation the quantity $\Delta u_1/\Delta u_2$ at 2mm behind the *moving* crack tip remains a constant. The amount of crack face opening is 3.3 times the amount of crack face sliding, thus indicating growth at a primarily opening mode *at this particular distance behind the tip*. This phenomenon is further discussed in the next section.

The condition of a constant $\Delta u_1/\Delta u_2$ behind the crack tip, equation (4.4), cannot constitute a dynamic crack growth criterion on its own because it does not predict the magnitude of the stresses surrounding the propagating crack. It may form part of a propagation criterion that relates the phase angle with the crack tip speed. The size of the stress field, and the CGS fringe pattern, surrounding the crack tip is primarily dependent upon $|K^d|$, the magnitude of the complex stress intensity factor. The second part of a fracture criterion would thus have to involve a link between $|K^d|$, v and ϕ. Consider a

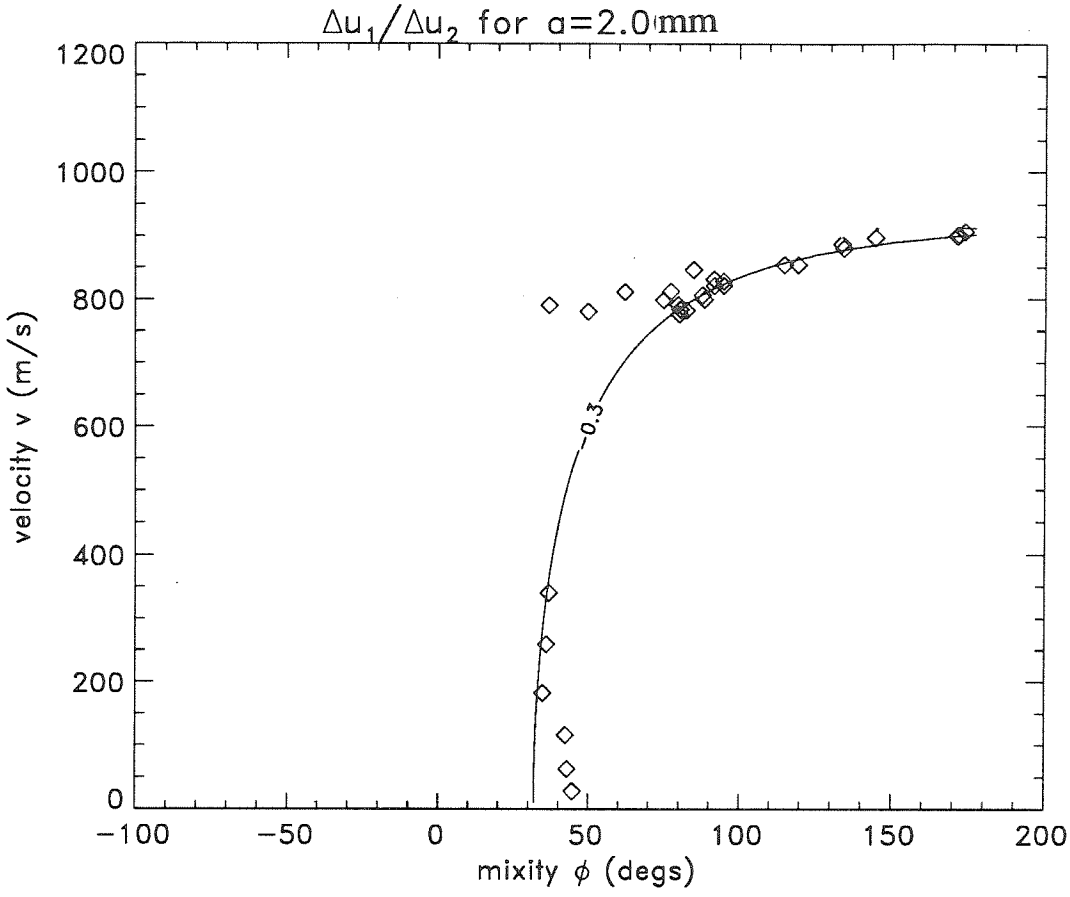

Figure 39: Fit of equation (4.4) to experimental data from three nominally identical one point bend PMMA/steel drop weight tower tests.

constant crack opening displacement, say of value C_2, at the same distance a behind the crack tip as before. From equation (4.2b) this can be expressed as

$$\Delta u_2(a) = \frac{H_{22}}{\cosh(\pi\varepsilon)}\sqrt{\frac{2a}{\pi}}\frac{|K^d|}{\sqrt{1+4\varepsilon^2}}\cos\left(\phi + \varepsilon \ln a - \tan^{-1}(2\varepsilon)\right) = C_2,$$

or solving for $|K^d|$

$$|K^d| = C_2\frac{\sqrt{1+4\varepsilon^2}\cosh(\pi\varepsilon)}{H_{22}}\sqrt{\frac{\pi}{2a}}\frac{1}{\cos\left(\phi + \varepsilon \ln a - \tan^{-1}(2\varepsilon)\right)}. \qquad (4.5)$$

The above is a relation between $|K^d|$, v and ϕ with C_2 and a as parameters. For specific values of C_2 and a equation (4.5) represents a surface in the $|K^d|$, v and ϕ space. An example of such a surface is plotted in figure 40 with $a=2mm$ and $C_2=1\,Pa$ (arbitrary).

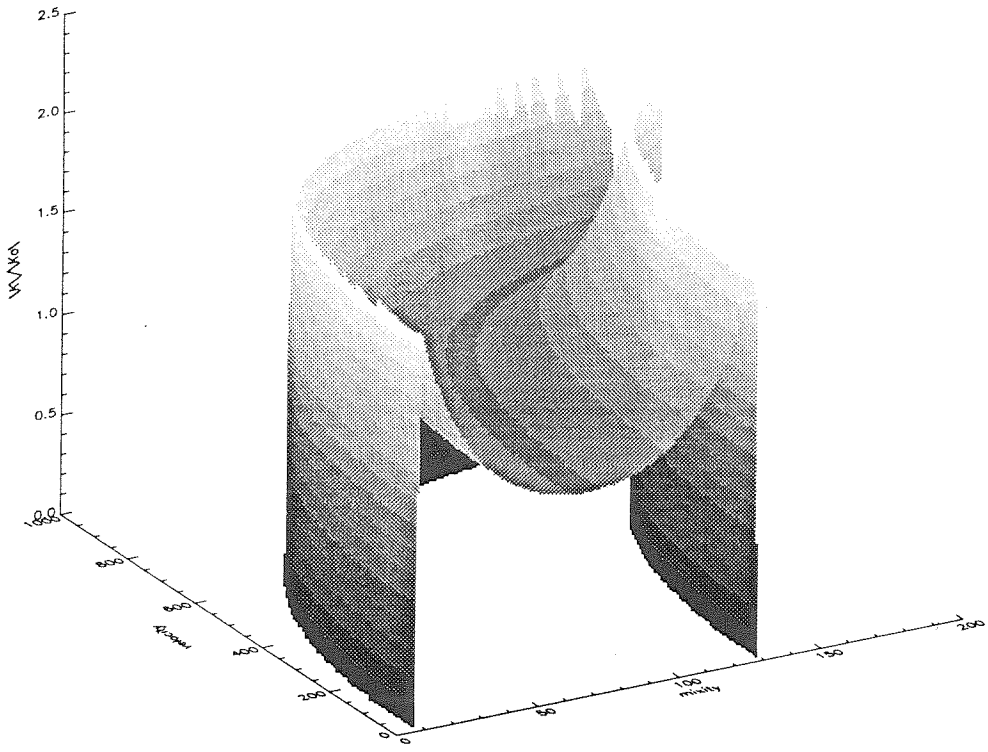

Figure 40: Three dimensional representation of the surface defined by equation (4.5), a constant crack opening displacement.

We have already seen from figure 39 that there is a relation between v and ϕ. We can now combine equations (4.4) and (4.5) to propose a complete criterion for dynamic crack growth along bimaterial interfaces. Substituting in equation (4.5) for ϕ from equation (4.4) we obtain a relation between $|K^d|$ and v only which incorporates the fact that $\Delta u_1/\Delta u_2$ is constant. The combination of (4.4) and (4.5) yields,

$$|K^d| = C_2 \frac{\sqrt{1+4\varepsilon^2}\cosh(\pi\varepsilon)}{H_{22}} \sqrt{\frac{\pi}{2a}} \frac{1}{\cos\left(\tan^{-1}(C_1\eta)\right)}. \tag{4.6}$$

The above depends on constants C_1 and C_2. Dependence on parameter a comes in only through its necessity in the choice of a constant C_1 to fit the experimental data using equation (4.4), as was done in figure 39. The value of C_1 is then fixed after performing this fit. For the results shown in figure 39 it was seen that C_1=*-0.3*. Unfortunately constant C_2, which essentially is the opening strength of the bond, cannot be easily determined. It can be eliminated though by normalizing equation (4.6) with some reference value. If we assume that one of the experimentally obtained data points, with parameters v_0, ε_0, η_0, H_{22}^0 $|K_0^d|$ and G_0, follows equation (4.6) then we can eliminate C_2 by computing $|K^d|/|K_0^d|$ as

$$\frac{|K^d|}{|K_0^d|} = \frac{\sqrt{(1+4\varepsilon^2)}\cosh(\pi\varepsilon)H_{22}^0\cos\left(\tan^{-1}(C_1\eta_0)\right)}{\sqrt{(1+4\varepsilon_0^2)}\cosh(\pi\varepsilon_0)H_{22}\cos\left(\tan^{-1}(C_1\eta)\right)}. \tag{4.7}$$

Comparison with all other experimental points is now possible by plotting equation (4.7) in the $|K^d|$, v plane.

For the PMMA/steel drop weight tower tests used previously, a comparison of the experimental data with equation (4.7) is shown in figure 41. The normalizing point used is the one corresponding to *v=180m/s*. This point is forced to agree with the computed curve (solid line in figure 41) since it has been used to eliminate the constant C_2. Nevertheless, the remaining points are not forced to follow the curve. It can be seen though that agreement is very good. A notable issue here is that the line in figure 41 is *not* a fit to the experimental values. Only C_1 is fitted to the experimental values using equation (4.4) as described above. Once this is done the curve given by equation (4.7) is *completely* specified. This implies that indeed not only is the ratio $\Delta u_1/\Delta u_2$ constant behind the crack tip, but Δu_2 itself is constant. These two facts therefore constitute the proposed dynamic fracture criterion for interfaces. An interfacial crack that has been impact loaded will initiate dynamic propagation at certain critical values of G_c and ϕ_c. Subsequently propagation will

be so as to maintain $\Delta u_1/\Delta u_2$ and Δu_2 constant at a critical distance behind the moving crack tip. Alternatively, the proposed criterion can be viewed as critical opening (Δu_2) and shearing (Δu_1) displacements at some distance a behind the moving crack tip. This is equivalent to requiring a self-similar crack profile throughout crack growth. A more

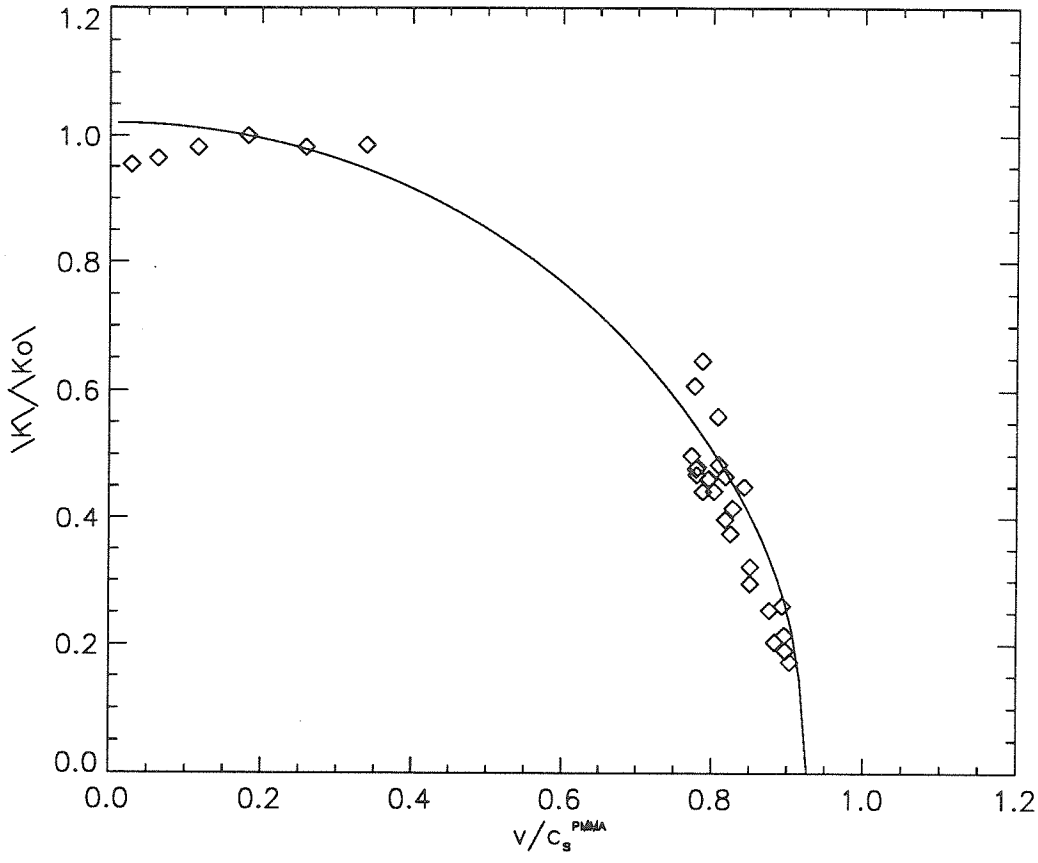

Figure 41: Comparison of normalized stress intensity factor from PMMA/steel drop weight tower tests with the result of equation (4.7).

detailed discussion of the proposed criterion and its implications is presented in the next section.

It is possible to convert equations (4.5), (4.6) and (4.7) to incorporate the energy release rate G instead of the magnitude of the stress intensity factor $|K^d|$. The quantities G and $|K^d|$ are related by equation (3.8). Figure 42 is analogous to figure 41, but with the

abscissa converted to the quantity G/G_0. Again it is seen that agreement between the proposed model and the experimental results is good. The deviation of the experimental

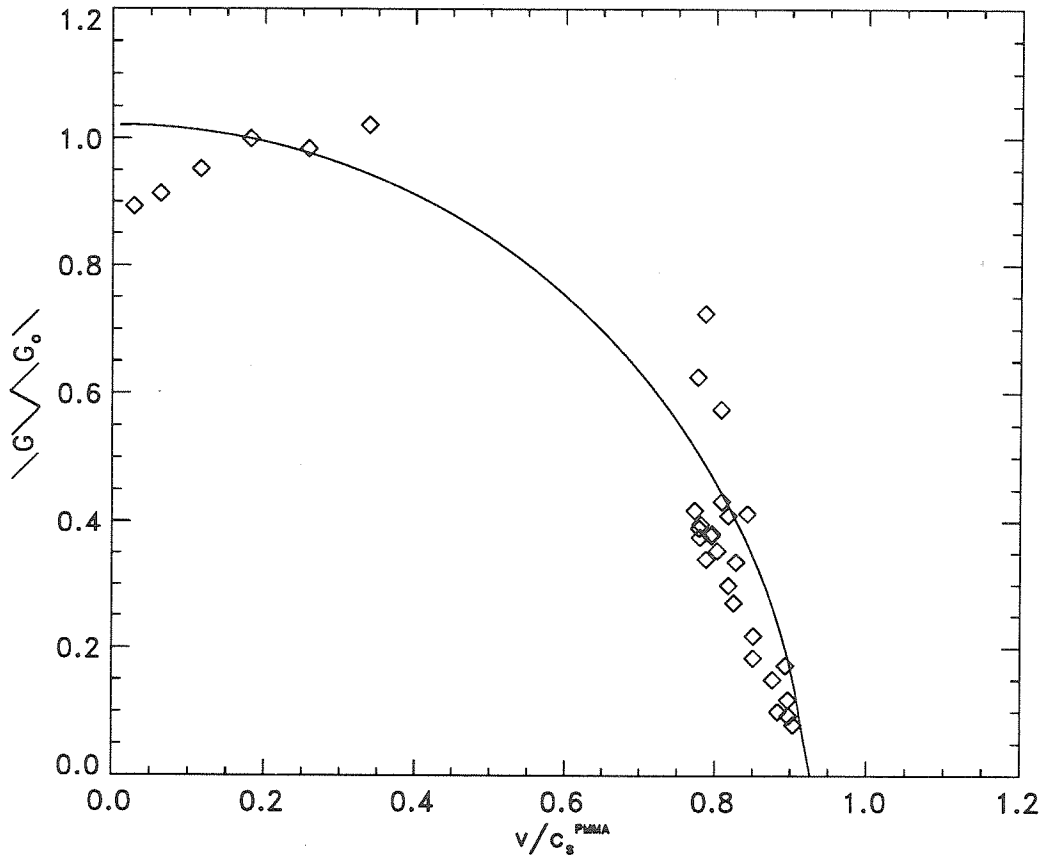

Figure 42: Comparison of normalized energy release rate from PMMA/steel drop weight tower tests with the result of equation (4.7).

points from the curve is somewhat more pronounced than in figure 41 since the energy release rate G depends on the second power of $|K^d|$.

Similar results were obtained when analyzing the PMMA/aluminum test shown in figure 11, and analyzed in figures 35 and 36. Figure 43 shows the best fit of equation (4.4) to those data points. Equation (4.4) has again been evaluated at $a=2mm$ which represents the inner size of the K^d-dominant region. A ratio of $\Delta u_1/\Delta u_2=0.5$ is now seen. The difference in loading history for the PMMA/aluminum system will cause crack initiation to

occur at different values of critical G_c and ϕ_c than before, which results in the difference in displacement ratio. Figure 44 shows a plot of equation (4.7) along with the experimental data points for this test. The normalization point used here is the one corresponding to *v=600m/s*. Once again agreement seems very good, reinforcing the validity of the proposed criterion by using a different material system.

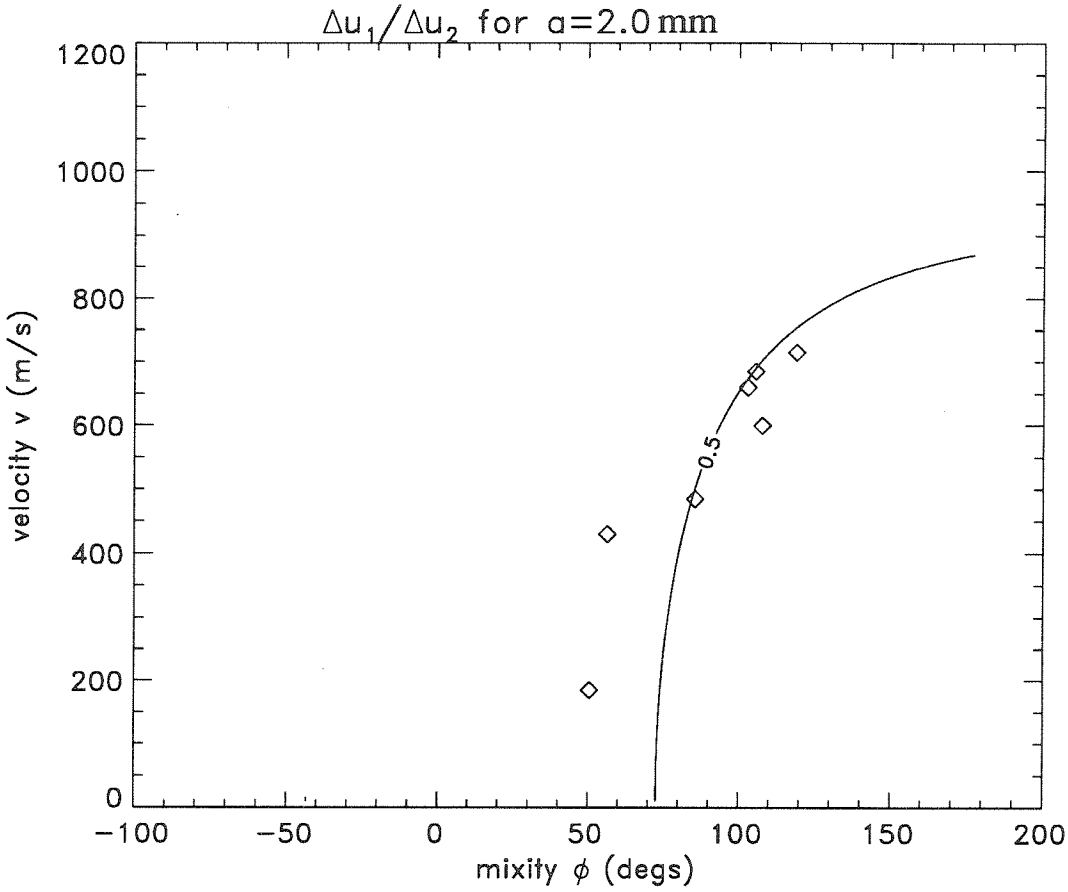

Figure 43: Fit of equation (4.4) to experimental data from a PMMA/aluminum drop weight tower test.

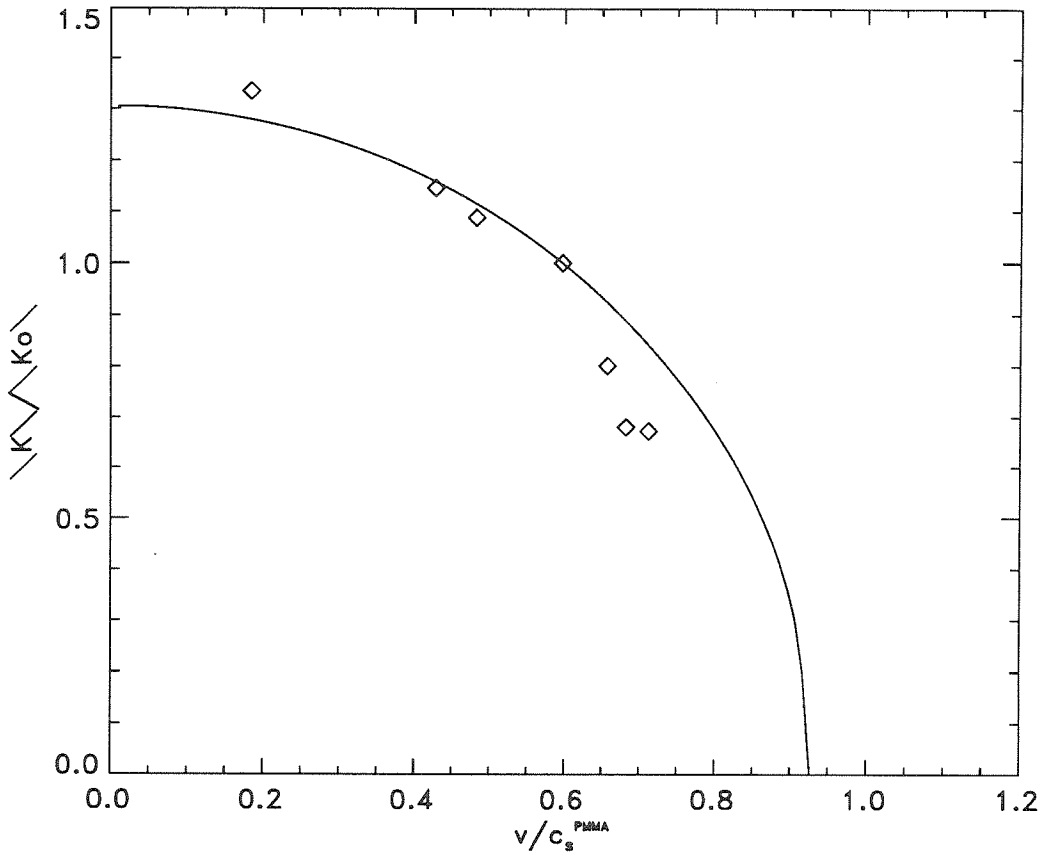

Figure 44: Comparison of normalized stress intensity factor a PMMA/aluminum drop weight tower test with the result of equation (4.7).

A parameter that would affect crack tip initiation conditions and hence the value of $\Delta u_1/\Delta u_2$, is the impact velocity. Several air gun experiments were performed on PMMA/steel bimaterial specimens. An impacted velocity of 20m/s was used, which produces a loading rate much higher than that of a drop weight device. (Initiation conditions are reached at much earlier times and at different combinations of G_c and ϕ_c). Results from three such air gun experiments are shown in figure 45. Here again we have plotted the best fit of equation (4.4) to the experimentally obtained values of v and ϕ. There is a larger amount of scatter in these data points primarily because the higher loading rates

cause larger transient effects in these experiments. Nevertheless the trend of the data shifting to the right is still present. Note that in these experiments $\Delta u_1/\Delta u_2$ is close to -3. This means that the magnitude of the shearing displacement is three times the magnitude of the opening displacement behind the crack tip (once again at a distance of $a=2mm$). Clearly these experiments are "shear" dominated, as was explained in section 3.1.2 using wave propagation arguments. When applying the result of equation (4.7) to the air gun test results using a value of $C_1=-3$ we obtain the solid line in figure 46. (The $C_1=-3$ value was obtained as generating the best fit of the data points in figure 45). The experimental points in this figure (diamonds) again have more scatter than before, but show an overall similar trend. The problem of increased scatter will be discussed further in the next section.

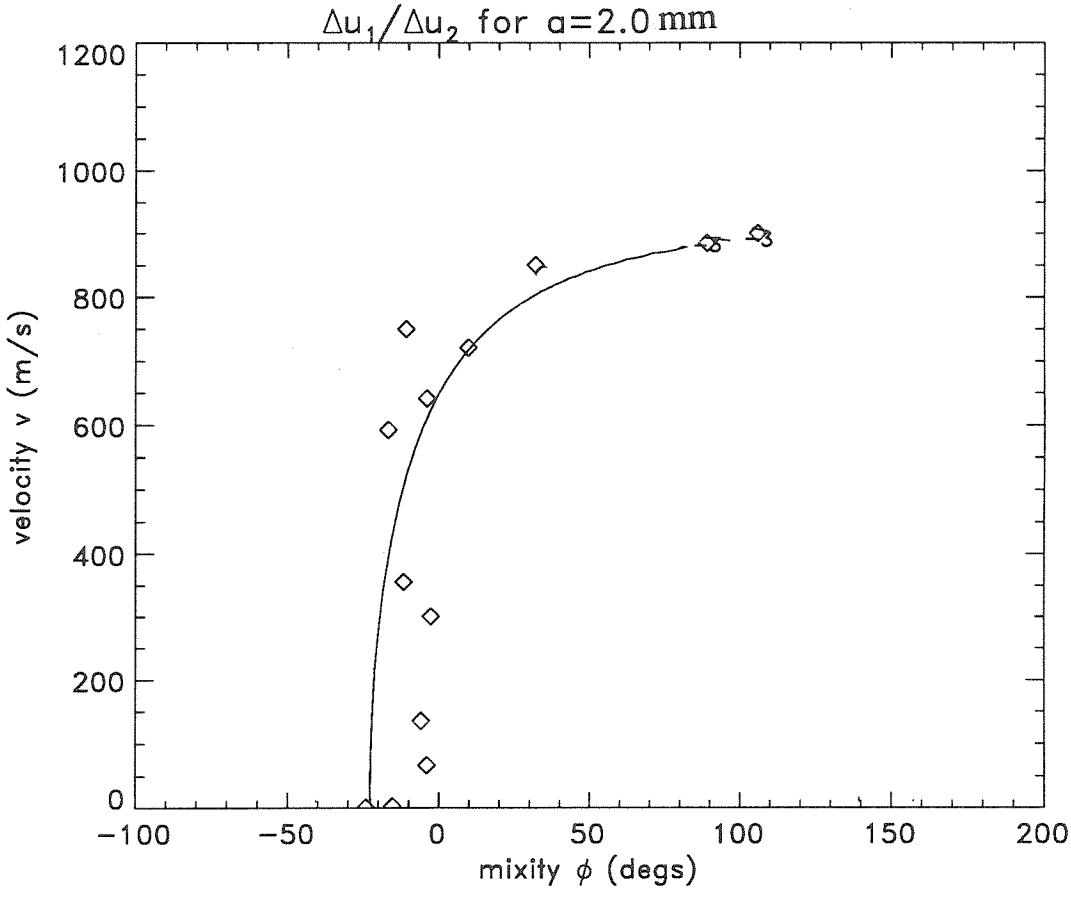

Figure 45: Fit of equation (4.4) to experimental data from three nominally identical one point bend PMMA/steel air gun tests.

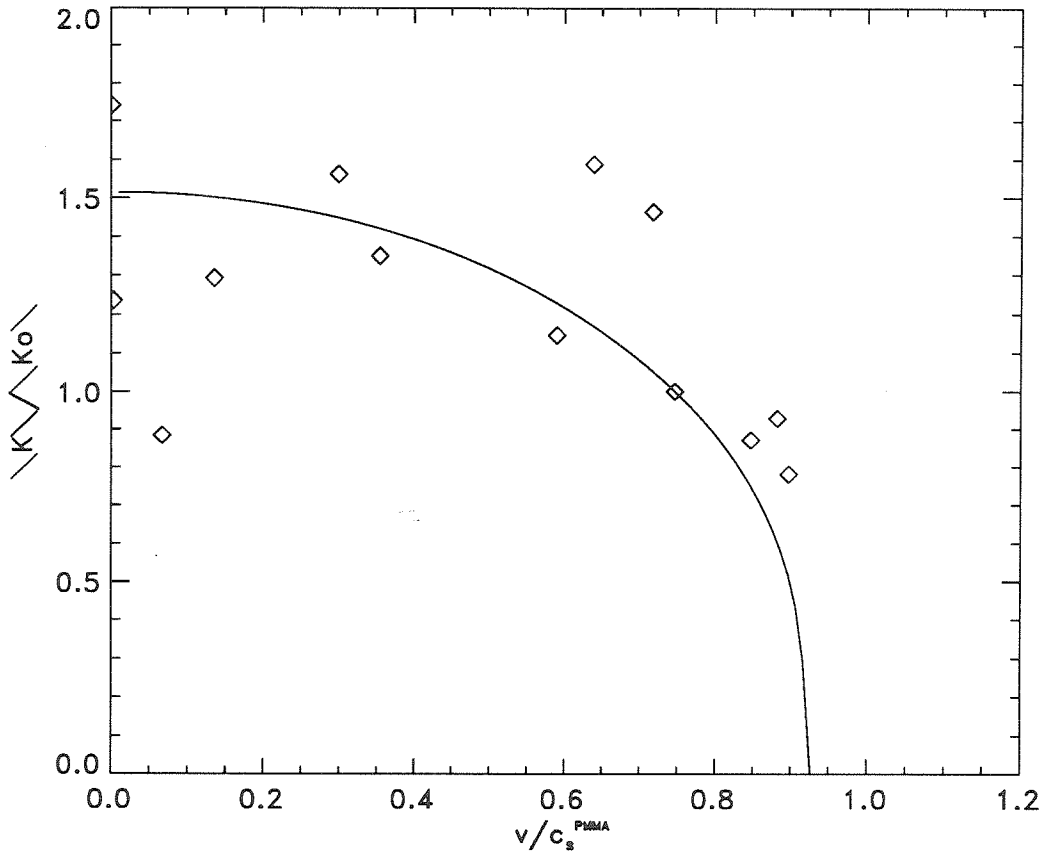

Figure 46: Comparison of normalized stress intensity factor from three PMMA/steel drop air gun tests with the result of equation (4.7).

All results shown above were based on the application of the proposed criterion at a distance of 2mm behind the propagating crack tip. Because of the nature of the interfacial stress and displacement field predicted by linear elasticity, the relative amounts of opening and shearing displacement behind the crack tip (displacement mixity) varies with distance. Therefore it is essential to make all comparisons at the same distance behind the tip. For this reason use of the proposed fracture criterion was made at 2mm behind the crack tip consistently. If we were to use a different distance behind the crack tip the numerical results would change, but the relative conclusions would still hold as long as all comparisons were made at that one fixed distance.

4.2 Discussion and implications of proposed fracture criterion

In all the above quoted experimental results it is worth noting that the data points corresponding to the lower velocities, and the first few microseconds after crack initiation in each test, are taken when very high transient effects involving $\dot{v}$ are present. The crack tip that has just initiated emits stress waves. Until these stress waves reach a particular material particle, that particle is not aware of the crack initiation event. Thus in most cases immediately after crack initiation a K-dominant stress field exists further away from the crack tip, while at closer distances it has been destroyed. This effect was discussed and illustrated in section 3.3.2 and in figure 33. It is this reason that causes the measured energy release rate G to rise a little after crack initiation has occurred (see the variation of G in figures 32, 35 and 37). The first few values of G after initiation are overestimated; they essentially correspond to the energy release rate of the *uninitiated* crack tip because the majority of material points are not yet aware of crack initiation. After a few microseconds when all material particles have felt the effects of crack initiation, the measured G drops. The same effects on measured energy release rate and fracture toughness have been observed in homogeneous materials. Aoki and Kimura (1993) in a numerical investigation using synthetic caustic patterns at the tip of a crack, observed an overshoot of the measured G just after initiation. In their work it was seen that the overshoot became much more pronounced as the loading rate on the crack-tip increased. Therefore in our experiments we expect this overshoot to be much more severe in the air gun rather than the drop weight tower tests. This probably accounts for the much larger increase of G during the initial stages of the air gun experiments (compare figures 32 and 37). Recall that in all gas gun experiments the crack-tip speed exceeded c_R^{PMMA}, the Rayleigh wave speed of Plexiglas, in less than 10μs. Therefore the results of the air gun tests should not be taken as being exact values for G and ϕ. They should rather be viewed as general trends.

It was clearly seen though, at least by the experimental results of the drop tower tests presented in the previous section, that a crack propagating dynamically along a

bimaterial interface did so while maintaining the opening and shearing displacements at a certain point behind its tip, constant. This fact was used to formulate a dynamic propagation criterion that essentially says that *the crack face profile remains the same during propagation.* What controls the exact crack face profile, or equivalently the constants C_1 and C_2 in equations (4.4) and (4.5), are the precise conditions at crack initiation. Dynamic crack initiation of a crack along a bimaterial interface is controlled by a relation between the critical energy release rate G_c and phase angle ϕ_c of the type shown in figure 2. This was discussed in section 1.2..2. As time progresses in an impact loading fracture experiment G and ϕ at the, still stationary, crack-tip change. When their values first match a point on the G_c-ϕ_c initiation curve then the crack initiates propagation. From that time onwards it propagates with a fixed crack face profile. Any initiation pair of G_c and ϕ_c is possible as long as it lies on the dynamic initiation criterion. Different values of C_1 and C_2, and thus different crack profiles, are possible by having different initiation conditions G_c and ϕ_c. Parameters that affect the initiation values of G and ϕ include the loading rate and the interface constituents. The former influence was experimentally investigated by the difference between the apparent values of C_1 and C_2 in the drop weight tower and air gun experiments. Also the PMMA/aluminum experiments produced a different crack face profile during propagation from equivalent PMMA/steel experiments. In all cases though it seemed that the crack face profile was maintained throughout propagation.

The propagation criterion proposed in this work agrees with the accepted initiation criterion based on G and ϕ which was described in section 1.2.2. Figure 40 shows a three-dimensional plot of $|K^d|$ (alternatively viewed as G) against v and ϕ. This curve represents one part of the criterion proposed in this study (from the equation $\Delta u_2\big|_{r=a} = C_2$). If $v=0m/s$ it is seen that this figure reduces to the "U" shaped dependence between G and ϕ presented in figure 2. A relation like $\Delta u_2\big|_{r=a} = C_2$ itself, equation (4.5), could conceivably be used as a fracture criterion. The surface in figure 40 would be a three-dimensional equivalent of the curve in figure 2. Any point on this surface would constitute a triad of $|K^d|$ (or G), v and ϕ

possible during crack propagation. The path followed by a growing crack whose propagation was governed by such a surface could be an arbitrary line on the surface $\Delta u_2|_{r=a} = C_2$. However we have seen experimentally that the condition $\Delta u_1/\Delta u_2|_{r=a} = C_1$ also holds throughout propagation. This therefore specifies a *particular* path to be followed on the surface $\Delta u_2|_{r=a} = C_2$. In our proposed criterion, once the initiation point on $v=0m/s$ has been established, the path $\Delta u_1/\Delta u_2|_{r=a} = C_1$ on the surface $\Delta u_2|_{r=a} = C_2$ is followed. This path selection is schematically illustrated in figure 47 in the$G$, v, ϕ space. Different impact velocities and geometries would cause initiation at a different point A (in figure 47) and the$G$, v, ϕ curve followed during crack growth would be different, but would still lay on the surface $\Delta u_2|_{r=a} = C_2$. Therefore all possible triads of$G$, v, ϕ for crack growth are given by $\Delta u_2|_{r=a} = C_2$, but they *cannot be attained arbitrarily.* They are only attainable when a path $\Delta u_1/\Delta u_2|_{r=a} = C_1$ is followed on the three-dimensional surface. This path corresponds to a self-similar crack profile throughout crack growth. Even though the interfacial crack growth criterion proposed here is more restrictive than just $\Delta u_2|_{r=a} = C_2$, it seems to agree well with the experimental data. In addition it makes good sense that in the problem of interfacial crack growth, which is inherently mixed mode, both opening and shearing displacements play a role in the fracture criterion. A similar result was seen in the work of Liechti and Knauss (1982a) and Liechti and Knauss (1982b). Using an interferometric technique, they observed a constant vectorial displacement behind the crack tip (i.e., a constant opening and shearing displacement) during quasi-static crack growth in bimaterial specimens. This is essential the same result with what we observe here for the case of dynamic interfacial crack growth.

A more general criterion for dynamic crack growth along bimaterial interfaces has been proposed by Lo et al. (1993). The criterion proposed there was,

$$G = \frac{G_n\left(1 - v/c_s^{(1)}\right)^{-\gamma}}{1 + (1-\lambda)\sin^2\phi},$$

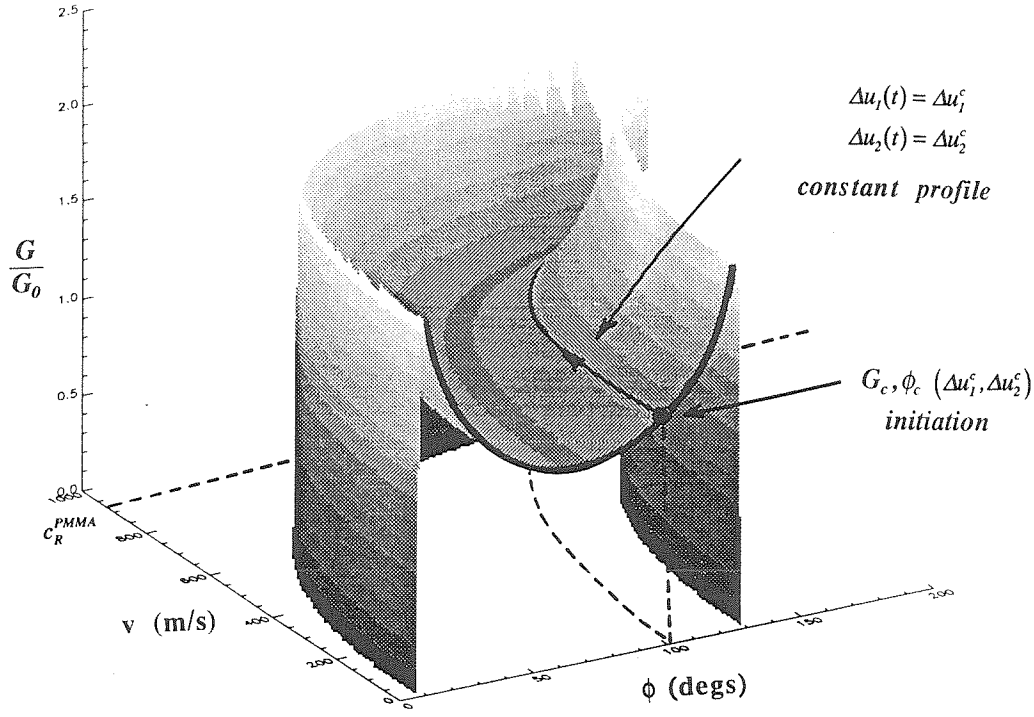

Figure 47: (G, v, ϕ) surface plot for $\Delta u_2|_{r=a} = const$. Crack path corresponding to constant crack face profile is superposed.

with the restriction that $\gamma>0$. The above equation has been adapted to nomenclature used in the present work. It represents a surface in the G, v, ϕ plane, much as equation (4.5) does. Lo et al. (1993) varied the values of the constants γ and λ to obtain a good fit with crack propagation velocities reported in the experiments of Tippur and Rosakis (1991). They resulted in values of $\gamma=0.2$ and $\lambda=0.3$. Since they did not have actual experimental data for G and ϕ at the time, the authors themselves admit that this criterion is purely speculative. In fact the current experimental measurements do *not* agree with this criterion since it predicts an increasing G with v, unless γ is a negative number.

A characteristic that has been observed in our experimental results is that crack propagation in the drop weight tower tests is more dominated by crack face opening than in the air gun tests (see figures 39 and 45). It must be pointed out though that the exact value of C_1 ($\Delta u_1/\Delta u_2\big|_{r=a} = C_1$) depends on the location, a, at which the ratio of displacements is evaluated. Even so the difference between drop weight and air gun tests will be maintained. The drop weight tower tests inherently are of a more "opening" nature.

The most predominant feature of our proposed model for dynamic interface fracture is that it predicts a decreasing energy release rate G as the crack-tip speed v increases. This is also seen by the experimental results obtained from real time interferograms (see figures 41, 42, 44 and 46). This means that there is actually a drop of the interface toughness as crack tip velocity increases. Such a behavior is uncharacteristic of most metals and polymers, though it has been observed in experiments involving certain ceramic and composite materials (Yang and Kobayashi (1990) and Razi and Kobayshi (1993)). The difference between the two cases arises because ductility in metals, and damage in polymers, induce shielding of the crack tip region in the form of plastic or damage zones. The size and shape of such zones is affected by inertia in such a way that it requires larger amounts of energy to sustain crack growth at higher speeds (see Freund and Douglas (1982)). In a purely brittle system, with no or very little non-linearity present, it may be possible to have a toughness that falls with increasing crack tip speed.

A decreasing dependence of G on v denotes an unstable crack growth process. Assuming that the externally supplied crack driving force remains constant, then the crack tip will continually accelerate. In fact, such a phenomenon is indeed observed in our dynamic interfacial crack growth experiments. Measured crack-tip speeds increase rapidly (within a few microseconds) to very high values. This observation is consistent with the instability caused by a constantly falling G, which reinforces the acceptability of the proposed fracture criterion. The trend of a falling G with increasing v also agrees with the theoretical analysis of Liu et al. (1993) who derived the asymptotic stress field surrounding

the tip of a crack propagating at $c_R^{PMMA} < v < c_S^{PMMA}$. (Recall that the stress fields in equations (3.4) and (3.5) are valid for $0 < v < c_R^{PMMA}$). In the work of Liu et al. (1993), for a crack propagation at a speed between the Rayleigh and shear wave speeds of PMMA (material-1) it was found that $G=0Nm$. Our experimental measurements predict a falling G which at higher crack growth speeds seems to approach zero.

Most results in metals and polymers that have predicted, or measured, toughening with increased crack-tip speed have been obtained on the basis of a steady crack growth event. There have been speculations by some researchers that a decreasing G with v might be possible, but has not yet been observed. This would represent an unstable branch in the G, v curve controlling dynamic fracture in homogeneous materials. As pointed out by Freund (1990), such a behavior could exist even in metallic solids, but would lead to an unstable event that is difficult to capture experimentally. Because of the nature of the interfacial problem and because we are using a very high framing rate in our high speed photographs we are able to capture these unstable phases of crack growth along bimaterial interfaces. Freund (1990), also found that a dropping energy release rate was possible during dynamic fracture of rate sensitive solids.

Finally, a very important point to note is that although the proposed criterion was derived using the results of the complex stress intensity factor history, the criterion itself may be general enough not to require K^d-dominance in its application. The criterion of a critical crack tip opening displacement, or opening angle, has been used extensively in the past for the fracture of homogeneous solids. It has been seen to be equivalent with initiation criteria based on K_I or J_I and growth criteria (quasi-static or dynamic) based on K_I in situations where K-dominance was assured. However, a criterion based on crack tip opening displacement has also been found to control fracture in instances when K_I or J_I are invalid or cannot be defined, such as growth in elastic-plastic materials. We therefore strongly believe that the proposed criterion for dynamic interfacial crack growth based on

both opening and shearing displacements behind the crack tip (crack profile) will be valid in a wide array of cases as well; even if a K^d-dominant region cannot be found.

In general, though the particular numerical values obtained in this study should be critically accepted, the trends indicated seem well founded and logical. Clearly more tests are required, using a wider array of loading geometries and loading rates, to obtain a complete understanding of the phenomena involved in dynamic interfacial fracture. Nevertheless, we believe that a dynamic propagation criterion involving critical displacements behind the crack tip is both reasonable and accurate, and should be investigated further.

CHAPTER 5

INTERSONIC CRACK GROWTH ALONG BIMATERIAL INTERFACES

In homogeneous materials intersonic crack growth is defined as the regime in which a dynamically growing crack is propagating at speeds between the shear and dilatational wave speeds of the material. Supersonic crack growth occurs when the crack speed exceeds the dilatational wave speed of the material. Extensive studies of high speed crack propagation phenomena have been made, albeit mostly of a theoretical nature. An early study of the fundamental solution of a moving point load propagating along an elastic half space was provided by Cole and Huth (1958). More recent theoretical contributions to the solution of the intersonic motion of a point load, or distribution of loads, on a half space are those of Georgiadis and Barber (1993a) and Georgiadis and Barber (1993b). In the area of high speed fracture there has been extensive theoretical work including the contributions of Burridge et al. (1979) and more recently of Broberg (1985), Broberg (1989), Bykovtsev and Kramarovskii (1989), Aleksandrov and Smetanin (1990) and Broberg (1993). As was shown by Broberg (1960), though, the speed of a remotely loaded traction free crack in a homogeneous material cannot exceed the Rayleigh wave speed c_R of that material. The energetic impossibility of exceeding c_R in homogeneous crack growth was discussed in section 3.1.2.

For the reason mentioned above it is difficult to obtain intersonic or supersonic crack growth in homogeneous materials under laboratory conditions. Since it is energetically impossible for a remotely loaded crack to travel at speeds over c_R, the only way to observe such propagation is to directly *supply* energy to the crack by driving it

externally. Examples of this include wedge opening of the crack faces or high energy laser pulse loading. Using laser pulse loading Winkler et al. (1970) and Curran et al. (1970) managed to drive cracks in KCl single crystals at supersonic speeds. More recently Huang and Virkar (1985) claimed to have recorded unassisted supersonic crack growth at very early stages (<1μs after initiation) of crack propagation in glass. In their paper they mention that Sanders (1972), using an atomistic model, was able to show that unassisted crack propagation at the atomic level may be possible at supersonic speeds. Although this result seems to corroborate the results of Huang and Virkar (1985) such high speed crack growth (supersonic) has not been observed by other researchers. One way to obtain high crack-tip speeds is to bond two elastic plates made of the same material and to initiate a crack on the interface. Washabaugh and Knauss (1993) have shown that as the bond strength is decreased, the crack-tip velocity increases to a significant fraction of c_R, but it never exceeds this value. In nature there have been some indications that certain seismic events can cause propagation of shear cracks at supersonic speeds, as reported by Broberg (1985). Clearly there are many problems associated with the experimental investigation of supersonic crack growth, and to our knowledge the above mentioned experimental works are the only ones of their kind.

As was mentioned before, in homogeneous materials intersonic crack growth occurs when a dynamically growing crack is propagating at velocities between the shear and dilatational wave speeds of the material. For the case of dynamic crack growth along bimaterial interfaces, the crack may be propagating intersonically with respect to one or the other material or with respect to both. The relative values of the wave speeds of the two materials define the possible cases. When the wave speeds of material-1 and material-2 are ordered as $c_s^{(1)} < c_l^{(1)} < c_s^{(2)} < c_l^{(2)}$ then intersonic crack growth may occur in one or the other material, but not in both. The first regime of intersonic crack growth would be when $c_s^{(1)} < v < c_l^{(1)}$ and would be subsonic for material-2. The second when $c_s^{(2)} < v < c_l^{(2)}$ and would be supersonic for material-1. The above mentioned arrangement of wave speeds is

exactly the case in our PMMA/steel specimens, with PMMA being material-1 and steel being material-2.

In section 3.1.2 the theoretical disagreement over the terminal crack-tip speed in dynamic interface fracture was presented. In addition it was mentioned that the work of Yang et al. (1991) predicted that the energy release rate remains finite for an interfacial crack traveling at $c_R^{(I)}$. Unlike crack growth in homogeneous materials, in this case there is no energetic restriction on the crack tip speed not to exceed $c_R^{(I)}$. The debate over the terminal crack speed has been essentially resolved by the findings of this study. The measured velocity history of crack propagation in a one point bend impact loaded PMMA/steel edge cracked plate was shown in figure 19. The results in figure 19 correspond to the sequence of interferograms in figure 14. Clearly both the Rayleigh and shear wave speeds of PMMA have been exceeded by this crack (see table 1 for wave speed values). In fact towards the end of the test the crack-tip speed seems to rise even further. The crack is propagating in the intersonic regime for PMMA, i.e., $c_s^{PMMA} < v < c_l^{PMMA}$, but is still under 50% of the Rayleigh wave speed of steel even at the largest measured crack tip speeds. The experiment whose interferograms are shown in figure 14 was conducted on a specimen having a sharp pre-crack along the interface. Impact was at 20m/s by an air gun projectile. Several other nominally identical test presented similar results. The velocity history from another such experiment is shown in figure 48. The same features are again present. A more notable feature in figure 48 is a distinct plateau just after the crack speed has exceeded c_s^{PMMA}. The reason for this deceleration and constant speed is not yet clear and is still being investigated. In any case it is a very repeatable feature of the experimental measurements. At later times the crack-tip speed increases even further.

To investigate whether even higher crack-tip speeds could be attained, a one point bend air gun impact experiment was conducted on a PMMA/steel specimen containing a *blunt* starter notch on the interface. A notch is able to store more energy before crack initiation occurs, thus driving the crack to higher speeds. A sequence of CGS

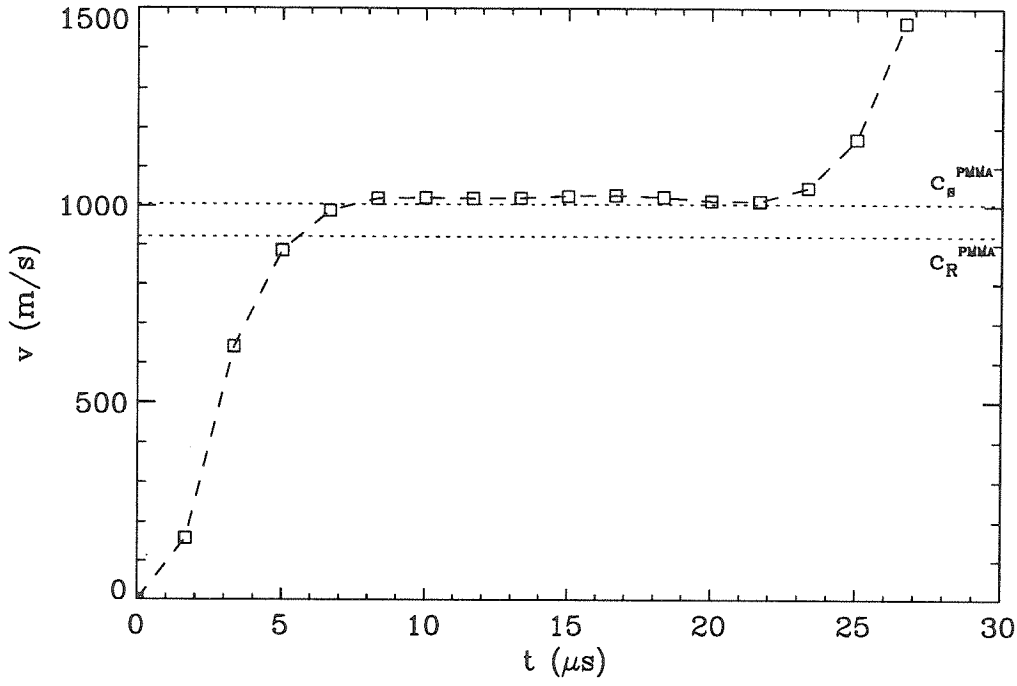

Figure 48: Velocity history for of a crack traveling along a PMMA/steel interface (air gun impact and a sharp starter crack were used).

interferograms for such a test is seen in figure 49. Once again only the PMMA side of the plate produces interferograms. The starter notch is clearly visible on the interface as a thick white band in the lower left-hand corner of each frame. The crack speed history for this test is shown in figure 50. In very short times the speed well exceeds the shear wave speed of Plexiglas. It then reaches a plateau value of about $1.4c_s^{PMMA}$. A clear change of the nature of the fringe pattern occurs between the first and last frames of figure 49. Initially, in the first one or two frames, the fringes are smooth and continuous. They represent the usual shear

dominated fringe pattern that somewhat resembles what has been observed during the early loading stages in drop weight tower experiments. As time progresses, but rather rapidly, the main lobe of the fringe pattern becomes squeezed and the fringes develop distinct kinks along certain directions. In the last interferogram of figure 49 the kinks have merged into

"shock-like" formations. It is not clear at this time exactly what these kinks represent. Since the crack is traveling at a velocity in the intersonic range for PMMA, we would expect shear, but not dilatational, shock waves to be present. Unfortunately because the optical technique of CGS measures gradients of direct stress components, shear effects cannot be imaged. It is believed that the apparent "shock" formations in the later interferograms either form because of Head waves, Achenbach (1973), that are propagating in front of the crack tip, or are three-dimensional effects associated with non-straight propagation of the crack front. This subject is still under investigation. Finally, additional visual evidence of the existence of large transonic and transient effects is seen in figure 51.

Unfortunately given existing theoretical analyses, we do not have the tools to fit any stress field to interferograms having a speed in the intersonic range of PMMA. We are currently in the process of developing an analysis for an interfacial crack traveling at speeds over c_s^{PMMA}. Nevertheless, even the physical implications of the observation of intersonic crack growth in bimaterial interfaces are important and should be discussed. It is believed that intersonic crack growth is possible in a bimaterial system because of an energy transfer mechanism from the stiffer (steel) to the softer (PMMA) side. The particulars of such a mechanism were explained in section 3.1.2 using wave propagation arguments. It was pointed out in that section that the time duration of the whole test is very small for any appreciable wave propagation to occur in PMMA. The duration of a typical experiment of an air gun loaded bimaterial plate is about 50μs from impact till the crack runs out of our field of view. Clearly therefore the whole propagation process is driven by energy leaking from the steel side across the interface. Because the Rayleigh wave speed of steel is larger than even the dilatational wave speed of Plexiglas, it is possible for the interface to sustain crack propagation at a speed in the range $c_s^{PMMA} < v < c_l^{PMMA} < c_R^{STEEL}$ by having the steel side supply energy to the PMMA and still provide the crack tip with enough energy to create new surfaces. Overall the composite specimen will be losing energy, which brings it to a more favorable state. An alternative presentation of this behavior is possible. As the steel

side of the bond fractures, the PMMA side feels the effect as a traction distribution on its surface. If the steel side of the specimen debonds fast enough, the traction distribution felt by the Plexiglas will be running on its surface at supersonic speeds (for Plexiglas). Thus the PMMA side of the bond sees a traction distribution propagating on its surface at speeds exceeding c_s^{PMMA}. For the steel side though the debonding that is occurring is doing so at speeds still below its own Rayleigh wave speed. It seems energetically logical that an interfacial crack could in no circumstances exceed the Rayleigh wave speed of steel. In fact the maximum crack tip speed possible would be somewhere between c_R^{PMMA} and c_R^{STEEL}. It would be the velocity at which the steel side would no longer be able to supply energy in the PMMA *and* keep the crack moving.

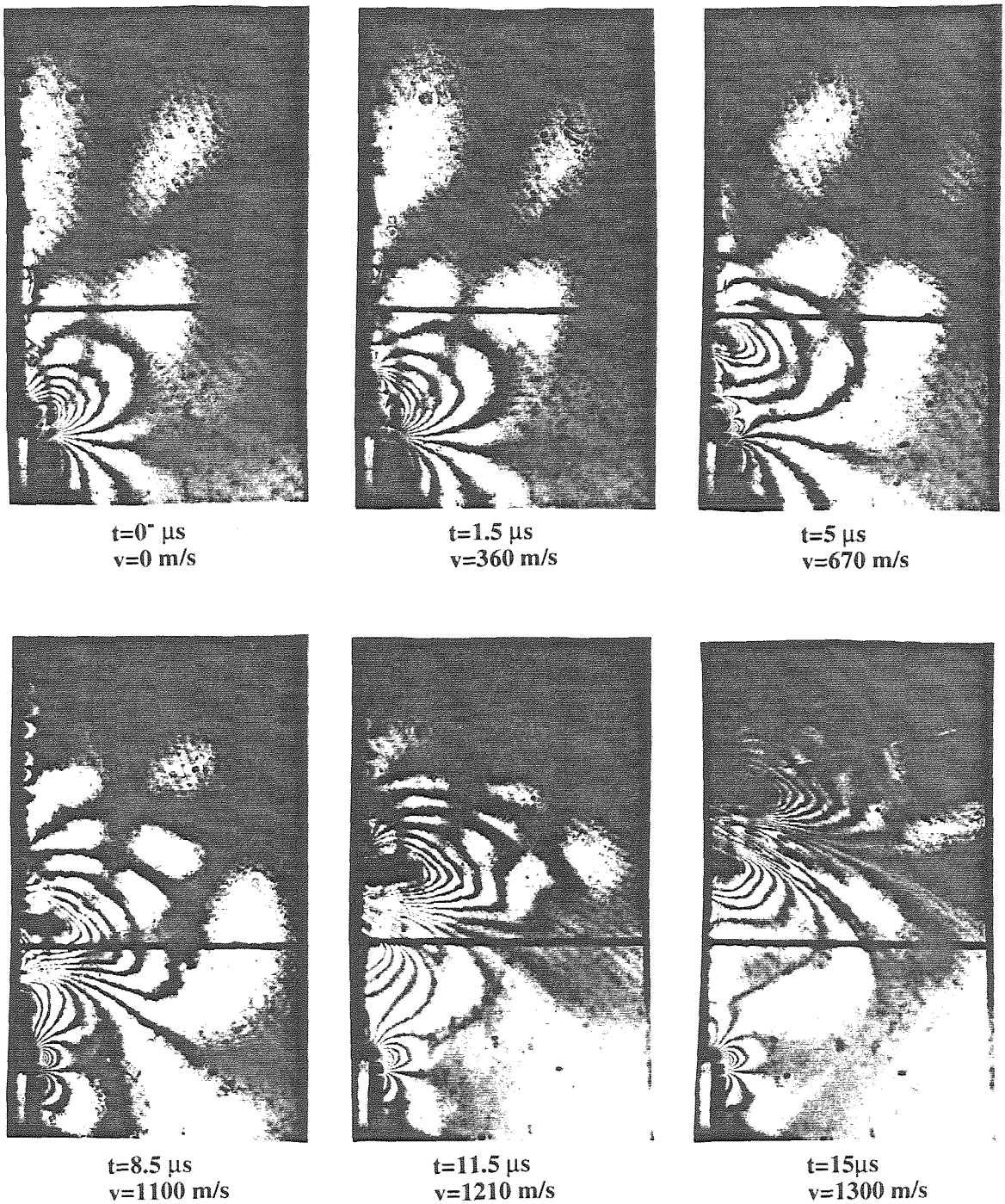

Figure 49: Selected sequence of CGS interferograms of a growing crack in a one point bend PMMA/steel air gun experiment (blunt starter notch).

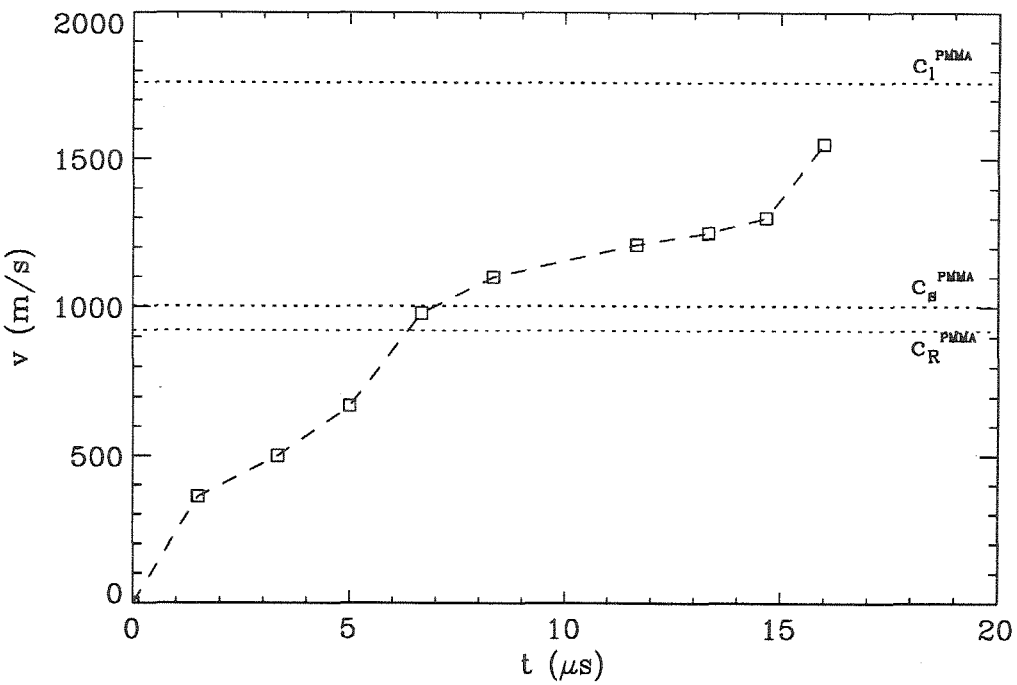

Figure 50: Velocity time history for the experiment shown in figure 49.

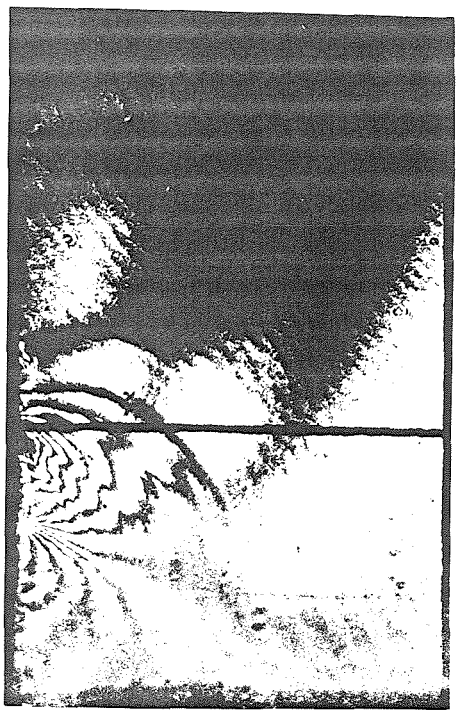

t=10 μs
v=1000 m/s

t=12.5 μs
v=1170 m/s

t=15.5 μs
v=1190 m/s

t=18.5 μs
v=1470 m/s

Figure 51: CGS interferograms providing visual evidence of the highly transient nature of dynamic interfacial crack growth.

CHAPTER 6

CONCLUDING REMARKS

The primary objective of the current study was to obtain a physically motivated and accurate criterion that governs dynamic interfacial fracture in bimaterial combinations with large mechanical property mismatch. To this end, a sequence of impact tests were performed on various loading configurations of PMMA/steel or aluminum bimaterial systems. Several conclusions may be drawn from the results of these tests, including a proposed interfacial crack growth criterion :

(i) Very large dynamic effects were observed in all dynamic bimaterial tests. In many instances, intense stress waves were seen emanating from the propagating crack tip. The higher the applied loading rate, the more severe the dynamic effects. In the case of the high speed gas gun experiments, a terminal crack propagation velocity around 90% of the plane stress dilatational wave speed of PMMA was observed. These observations have resolved the pre-existing debate on whether dynamic interfacial crack growth can occur at speeds exceeding the Rayleigh wave speed of the more compliant of the two constituents. The maximum possible velocity for interfacial crack growth is believed to be somewhere between the Rayleigh wave speeds of the two constituents.

(ii) The duration of the whole event, from impact to the end of crack propagation, is of the order of 110μs. For experiments at high loading rates it may even be less than half

this time. This suggests that the whole process of interfacial crack initiation and growth in these tests is driven by energy "leaking" from the metal side to the PMMA side of the bond.

(iii) In addition to dynamic effects, very severe transient effects have been seen to occur, especially during the early stages of crack growth. Evidence of transience are the very large accelerations recorded (maximum values of the order of 10^7g where g is the acceleration of gravity). The phenomenon of the existence of highly transient deformations was corroborated by direct comparison of the experimental results to a transient elastodynamic analysis.

(iv) It was experimentally observed that the crack profile (opening and shearing displacements at a given distance behind the propagating crack tip) remained constant throughout propagation. This observation formed the basis of the proposed dynamic fracture criterion. The use of the notion of an invariant crack face profile as a fracture criterion is both physically sensible and consistent with fracture models proposed for quasi-static and dynamic fracture of homogeneous materials. Even though in this particular study use of the complex dynamic stress intensity factor was made in the observation of a critical state in crack face displacements, the proposed fracture criterion itself is of a more general nature. A criterion based on crack face profile may still be applicable to situations where large plasticity and/or large-scale three-dimensional effects are dominant or where intersonic and supersonic crack growth is occurring (e.g., in a situation where there is no K^d-dominance).

(v) The energy release rate during crack growth was seen to decrease with increasing crack tip speed. This observation implies that interfacial crack propagation, at least in the geometries and systems tested in the current study, is an unstable process. This

is consistent with the very high crack tip speeds and accelerations recorded in the experiments.

To our knowledge this is the first thorough experimental investigation into the phenomenon of dynamic interfacial fracture. More work is required, though, for a complete understanding of the mechanics of dynamic interfacial crack growth. It may be possible to suppress the very high transient effects seen in current experiments, by performing tests at very low loading rates. Additional drop weight tower tests of PMMA/steel specimens impacted at 1-2m/s should provide more experimental results to verify the subsonic dynamic fracture criterion proposed in this study. On the other hand this is one of the few experimental studies to have observed intersonic crack growth under laboratory conditions. Experiments at higher loading rates should be able to drive the crack tip speeds even higher than recorded here. We believe it is possible to obtain crack growth at velocities exceeding the plane stress dilatational wave speed of PMMA. This would probably cause *dilatational* shock waves to appear in the CGS interferograms. Visualization of *shear* shock waves, which unfortunately could not be made in this study, is possible by using an optical technique sensitive to shear stresses (e.g., dynamic photoelasticity). In addition, an analytical solution of the asymptotic stress field surrounding the tip of an interfacial crack traveling at intersonic speeds would be extremely helpful. It would be of great interest to see whether the proposed criterion for subsonic interfacial crack growth can be extended to the transonic and intersonic regimes. It is certainly general enough. Finally, for the complete investigation of dynamic interfacial fracture, it would be advantageous to obtain optical data from both sides of a dynamically propagating bimaterial crack tip. For this purpose the constituents of the interface should be two transparent materials (e.g., PMMA and Homalite-100). A dynamic investigation of this kind would be very enlightening as to the precise mechanism of energy transfer between the two constituents. In addition the

smaller mismatch of elastic properties between PMMA and Homalite-100 may result in less severe transient effects.

The underlying motivation for this study, and most of the research on interfacial fracture mechanics, is to better understand failure mechanisms in composite materials. For this reason, continued research on interface fracture should primarily focus on idealized material systems that involve constituents relevant to composite materials. Such bimaterial systems include ceramic/polymer, ceramic/metal and ceramic/glass. Finally, in relation to the applicability of interfacial fracture to layered composites, or in fact layered microchips, an idealized multi-layered, multi-material system could also be tested.

REFERENCES

Achenbach, J. D. (1973), "Wave Propagation in Elastic Solids," North-Holland.

Aleksandrov, V. M. and Smetanin, B. I. (1990), "Supersonic Cleavage of an Elastic Strip," PMM U.S.S.R., **54**(5), pp. 677-682.

Aoki, S. and Kimura, T. (1993), "Finite Element Study on the Optical Method of Caustic for Measuring Impact Fracture Toughness," Journal of the Mechanics and Physics of Solids, **41**(3), pp. 413-425.

Atkinson, C., Ed. (1977), "Dynamic Crack Problems in Dissimilar Media," Mechanics of Fracture 4 : Elastodynamic Crack Problems.

Beinert, J. and Kalthoff, J. F. (1981), "Experimental Investigation of Stress Intensity Factors by Shadow Patterns," Mechanics of Fracture 7, pp. 281-330.

Broberg, K. B. (1960), "The Propagation of a Griffith Crack," Ark. Fys., **18**, pp. 159.

Broberg, K. B. (1985), "Irregularities at Earth-Quake Slip," Journal of Technical Physics, **26**(3-4), pp. 275-284.

Broberg, K. B. (1989), "The Near-Tip Field at High Crack Velocities," International Journal of Fracture, **39**(1-3), pp. 1-13.

Broberg, K. B. (1993), "Intersonic Mode II Crack Expansion," private communication.

Brock, L. M. and Achenbach, J. D. (1973), "Extension of an Interface Flaw under the Influence of Transient Waves," International Journal of Solids and Structures, **9**, pp. 53-67.

Burridge, R., Conn, G. and Freund, L. B. (1979), "The Stability of a Rapid Mode II Shear Crack with Finite Cohesive Traction," Journal of Geophysical Research, **85**(B5), pp. 2210-2222.

Bykovtsev, A. S. and Kramarovskii, D. B. (1989), "Non-Stationary Supersonic Motion of a Complex Discontinuity," PMM U.S.S.R., **53**(6), pp. 779-786.

Cagniard, L. (1962), "Reflection and Refraction of Progressive Seismic Waves," New York, McGraw-Hill.

Cole, J. and Huth, J. (1958), "Stress Produced in a Halfplane by Moving Loads," Journal of Applied Mechanics, **25**, pp. 433-436.

Comninou, M. (1977a), "The Interface Crack," Journal of Applied Mechanics, **44**, pp. 631-636.

Comninou, M. (1977b), "Interface Crack with Friction in the Contact Zone," Journal of Applied Mechanics, **44**, pp. 780-781.

Curran, D. R., Shockey, D. A. and Winkler, S. (1970), "Crack Propagation at Supersonic Velocities, II. Theoretical Model," International Journal of Fracture, **6**(3), pp. 271.

Deng, X. (1991), "General Crack Tip Fields for Stationary and Steadily Growing Interface Cracks in Anisotropic Bimaterials," Journal of the Mechanics and Physics of Solids.

Deng, X. (1992), "Complete Complex Series Expansions of Near Tip Fields for Steadily Growing Interface Cracks in Dissimilar Isotropic Materials," Engineering Fracture Mechanics, **42**(2), pp. 237-242.

Dundurs, J. (1969), "Edge-Bonded Dissimilar Orthogonal Elastic Wedges Under Normal and Shear Loading," Journal of Applied Mechanics, (September), pp. 650-652.

England, A. H. (1965), "A crack between dissimilar media," Journal of Applied Mechanics, pp. 400-402.

Erdogan, F. (1965), "Stress Distribution in Bonded Dissimilar Materials with Cracks," Journal of Applied Mechanics, (June), pp. 403-410.

Erdogan, F. and Sih, G. E. (1963), "On the Crack Extension in Plates under Plane Loading and Transverse Shear," Journal of Basic. Engineering, **85**, pp. 519-527.

Evans, A. G. (1989), "The Mechanical Performance of Fiber-Reinforced Ceramic Matrix Composites," Materials Science and Engineering, **A107**, pp. 227-239.

Foltyn, P. A. and Ravichandar, K. (1993), "Initiation of an Interface Crack under Mixed-Mode Loading," Journal of Applied Mechanics, **60**(1), pp. 227-229.

Freund, L. B. (1990), "Dynamic Fracture Mechanics," Cambridge University Press.

Freund, L. B. and Douglas, A. S. (1982), "The Influence of Inertia on Elastic-Plastic Antiplane Shear Crack Growth," Journal of the Mechanics and Physics of Solids, **30**, pp. 59-74.

Freund, L. B. and Rosakis, A. J. (1992), "The Structure of the Near Tip Field During Transient Elastodynamic Crack Growth," Journal of the Mechanics and Physics of Solids, **40**(3), pp. 699-719.

Gautsen, A. K. and Dundurs, J. (1987), "The Interface Crack in a Tension Field," Journal of Applied Mechanics, **54**, pp. 93-98.

Gautsen, A. K. and Dundurs, J. (1988), "The Interface Crack under Combined Loading," Journal of Applied Mechanics, **55**, pp. 580-586.

General (1989), "Aerospace Structural Metals Handbook," Columbus, Ohio, Battelle Columbus Laboratories.

Georgiadis, H. G. and Barber, J. R. (1993a), "Steady-State Transonic Motion of a Line Load over an Elastic Half-Space - The Corrected Cole Huth Solution," Journal of Applied Mechanics, **60**(3), pp. 772-774.

Georgiadis, H. G. and Barber, J. R. (1993b), "On the Super-Rayleigh Subseismic Elastodynamic Indentation Problem," Journal of Elasticity, **31**(3), pp. 141-161.

Geubelle, P. H. and Knauss, W. G. (1991), "Crack Propagation At and Near Bimaterial Interfaces : Linear Analysis," to appear in Journal of Applied Mechanics.

Geubelle, P. H. and Knauss, W. G. (1992a), "Finite Strains at the Tip of a Crack in a Sheet of Hyperelastic Material : II. Special Bimaterial Cases," to appear in Journal of Elasticity.

Geubelle, P. H. and Knauss, W. G. (1992b), "Finite Strains at the Tip of a Crack in a Sheet of Hyperelastic Material : III. General Bimaterial Case," to appear in Journal of Elasticity.

Goldshtein, R. V. (1967), "On Surface Waves in Joined Elastic Materials and their Relation to Crack Propagation along the Junction," Applied Mathematics and Mechanics, **31**, pp. 496-502.

Griffith, A. A. (1921), "The Phenomena of Rupture and Flow in Solids," Philosophical Transactions Royal Society of London, **A221**, pp. 163-197.

Gu, P. (1991), "Multi-Layer Material with an Interface Crack," Brown University Report.

Hashin, Z. (1983), "Analysis of Composite Materials - A Survey," Journal of Applied Mechanics, **50**(9), pp. 481-505.

Huang, J. L. and Virkar, A. V. (1985), "High Speed Fracture in Brittle Materials: Supersonic Crack Propagation," Engineering Fracture Mechanics, **21**(1), pp. 103-113.

Hutchinson, J. W. (1989), "Mixed Mode Fracture Mechanics of Interfaces," Harvard University Report.

Kanninen, M. F. and Popelar, C. H. (1985), "Advanced Fracture Mechanics," Oxford University Press.

Knowles, J. K. and Sternberg, E. (1983), "Large Deformations Near a Tip of an Interface Crack Between Two Neo-Hookean Sheets," Journal of Elasticity, **13**, pp. 257-293.

Krishnaswamy, S., Rosakis, A. J. and Ravichandran, G. (1991), "On the Extent of Dominance of Asymptotic Elastodynamic Crack-Tip Fields; Part II : A Numerical Investigation of Three-Dimensional and Transient Effects," Journal of Applied Mechanics, **58**(1), pp. 95-103.

Lee, Y. J., Lambros, J. and Rosakis, A. J. (1993), "Analysis of Coherent Gardient Sensing (CGS) by Fourier Optics," submitted to Optics and Lasers in Engineering.

Lee, Y. J. and Rosakis, A. J. (1992), "Interfacial Cracks in Plates : A Three-Dimensional Numerical Investigation," to appear in the International Journal of Solids and Structures.

Liechti, K. M. and Chai, Y. S. (1991), "Biaxial Loading Experiments for Determining Interfacial Fracture-Toughness," Journal of Applied Mechanics, **58**(3), pp. 680-687.

Liechti, K. M. and Chai, Y. S. (1992), "Asymmetric Shielding in Interfacial Fracture under Inplane Shear," Journal of Applied Mechanics, **59**(2), pp. 295-304.

Liechti, K. M. and Knauss, W. G. (1982a), "Crack Propagation at Material Interfaces : I Experimental Technique to Determine Crack Profiles," Experimental Mechanics, **22**(7), pp. 262-269.

Liechti, K. M. and Knauss, W. G. (1982b), "Crack Propagation at Material Interfaces : II Experiments on Mode Interaction," Experimental Mechanics, **22**(10), pp. 383-391.

Liu, C., Lambros, J. and Rosakis, A. J. (1993), "Highly Transient Elastodynamic Crack Growth in a Bimaterial Interface : Higher Order Asymptotic Analysis and Experiments," Journal of the Mechanics and Physics of Solids, **41**(12), pp. 1887-1954.

Lo, C. Y., Nakamura, T. and Kushner, A. (1993), "Computational Analysis of Dynamic Crack Propagation Along Bimaterial Interfaces," to appear in Journal of the Mechanics and Physics of Solids.

Malyshev, B. M. and Salganik, R. L. (1965), "The Strength of Adhesive Joints using the Theory of Cracks," International Journal of Fracture Mechanics, **1**, pp. 114-128.

Mecholsky, J. J. (1989), "Engineering Research Needs of Advanced Ceramics and Ceramic-Matrix Composites," Ceramic Bulletin, **68**(2), pp. 367-375.

Murty, M. V. R. K. (1964), "The use of a single plane parallel plate as a lateral shearing interferometer with a visible gas laser source," Applied Optics, **3**, pp.

Nakamura, T. (1991), "Three Dimensional Stress Fields of Elastic Interface Cracks," Journal of Applied Mechanics, **58**(4), pp. 939-946.

O'Dowd, N. P., Stout, M. G. and Shih, C. F. (1992), "Fracture-Toughness of Aluminum Niobium Interfaces - Experiments and Analyses," Philosophical Magazine A, **66**(6), pp. 1037-1064.

Ravichandran, G. and Knauss, W. G. (1989), "A Finite Elastostatic Analysis of Bimaterial Interface Cracks," International Journal of Fracture, **39**(1-3), pp. 235-253.

Razi, H. and Kobayshi, A. (1993), "Delamination in Cross-Ply Laminated Composite Subjected to Low Velocity Impact," AIAA Journal, **31**(8), pp. 1498-1502.

Rice, J. R. (1988), "Elastic Fracture Mechanics Concepts for Interfacial Cracks," Journal of Applied Mechanics, **55**(March), pp. 98-103.

Rice, J. R. and Sih, G. C. (1965), "Plane Problems of Cracks in Dissimilar Media," Journal of Applied Mechanics, (June), pp. 418-423.

Rosakis, A. J. (1993), "Two Optical Techniques Sensitive to Gradients of Optical Path Difference: The Method of Caustics and the Coherent Gradient Sensor (CGS)," Experimental techniques in fracture, pp. 327-425.

Rosakis, A. J. and Ravi-Chandar, K. (1986), "On Crack-Tip Stress States : An Experimental Evaluation of Three Dimensional Effects," International Journal of Solids and Structures, **22**, pp. 121-134.

Rosakis, A. J. and Zehnder, A. T. (1985), "On the Dynamic Failure of Structural Metals," International Journal of Fracture, **27**, pp. 169-186.

Sanders, W. T. (1972), "On the Possibility of a Supersonic Crack in a Crystal Lattice," Engineering Fracture Mechanics, **4**, pp. 145.

Shih, C. F. (1991), "Cracks on Bimaterial Interfaces : Elasticity and Plasticity Aspects," Materials Science and Engineering, **A143**, pp. 77-90.

Shih, C. F., Delorenzi, H. G. and Andrews, W. R. (1979), "Studies on Crack Initiation and Stable Crack Growth," Elastic-Plastic Fracture, **ASTM STP 668**(J. D. Landes (ed.)), pp. 65-120.

Sih, G. C. and Rice, J. R. (1964), "Bending of Plates of Dissimilar Materials with Cracks," Journal of Applied Mechanics, **31**, pp. 477-482.

Symington, M. F. (1987), "A Review of some Aspects of the Linear Elastic Analysis of Bimaterial Cracks," Brown University, Masters Thesis.

Tippur, H. K., Krishnaswamy, S. and Rosakis, A. J. (1991), "Optical Mapping of Crack Tip Deformations Using the Method of Transmission and Reflection Coherent Gradient Sensing: A Study of Crack Tip K-Dominance," International Journal of Fracture, **52**, pp. 91-117.

Tippur, H. V. (1992), "Coherent Gradient Sensing : A Fourier Optics Analysis and Applications to Fracture," Applied Optics, **31**(No. 22), pp. 4428-4439.

Tippur, H. V., Krishnaswamy, S. and Rosakis, A. J. (1991), "A Coherent Gradient Sensor for Crack Tip Measurements : Analysis and Experimental Results," International Journal of Fracture, **48**, pp. 193-204.

Tippur, H. V. and Rosakis, A. J. (1991), "Quasi-static and Dynamic Crack Growth along Bimaterial Interfaces : A Note on Crack-Tip Field Measurements Using Coherent Gradient Sensing," Experimental Mechanics, **31**(No. 3), pp. 243-251.

Wang, J.-S. and Suo, Z. (1990), "Experimental Determination of Interfacial Toughness Curves Using Brazil-Nut-Sandwiches," Acta Metallurigica Materialis, **38**(7), pp. 1279-1290.

Washabaugh, P. G. and Knauss, W. G. (1993), "A Reconciliation of Dynamic Crack Velocity and Rayleigh Wave Speed in Isotropic Brittle Solids," submitted to the International Journal of Fracture.

Wells, A. A. (1961), "Unstable Crack Propagation in Metals, Cleavage and Fast Fracture," The Crack Propagation Symposium, Cranfield, England.

Wells, A. A. (1963), "Applications of Fracture Mechanics At and Beyond General Yield," British Welding Res. Ass. Rept., **M13/63**, pp.

Williams, M. L. (1959), "The Stresses Around a Fault or Crack in Dissimilar Media," Bulletin of the Seismological Society of America, **49**(No. 2), pp. 199-204.

Willis, J. R. (1971), "Fracture Mechanics of Interfacial Cracks," Journal of the Mechanics and Physics of Solids, **19**, pp. 353-368.

Willis, J. R. (1973), "Self-Similar Problems in Elastodynamics," Philosophical Transactions of the Royal Society (London), **274**, pp. 435-491.

Winkler, S., Shockey, D. A. and Curran, D. R. (1970), "Crack Propagation at Supersonic Velocities, I," International Journal of Fracture, **6**(2), pp. 151.

Wu, K. C. (1991), "Explicit Crack Tip Fields of an Extending Interface Crack in an Anisotropic Bimaterial," International Journal of Solids and Structures, **27**(4), pp. 455-466.

Yang, K. H. and Kobayashi, A. (1990), "Dynamic Fracture Response of Alumina and Two Ceramic Composites," Journal of American Ceramics Society, **73**(8), pp. 2309-2315.

Yang, W., Suo, Z. and Shih, C. F. (1991), "Mechanics of Dynamic Debonding," Proceedings of the Royal Society of London, **A433**, pp. 679-697.

APPENDIX

PROPERTIES OF INTERFACES

In Yang et al. (1991), a compliance like Hermitian matrix characterizing the interface is defined as

$$H = B^{(1)} + \overline{B}^{(2)},$$

where an overbar denotes a complex conjugate. For an isotropic material B takes the form of,

$$B = \frac{1}{\mu D}\begin{pmatrix} \alpha_s\left(1-\alpha_s^2\right) & i\left(1+\alpha_s^2-2\alpha_l\alpha_s\right) \\ -i\left(1+\alpha_s^2-2\alpha_l\alpha_s\right) & \alpha_l\left(1-\alpha_s^2\right) \end{pmatrix},$$

where μ is the shear modulus of the material, i is the square root of -1 and the Rayleigh function D is given by,

$$D = 4\alpha_l\alpha_s - \left(1+\alpha_s^2\right)^2,$$

with α_l, α_s having been defined in section 3.2.1. For the case of isotropic materials therefore, H depends on three independent coefficients $H_{\alpha\beta}$:

$$H = \begin{pmatrix} H_{11} & iH_{12} \\ -iH_{12} & H_{22} \end{pmatrix}.$$

These coefficients can be related to the interface parameters ε (through the second Dundurs parameter β), η and F.

Parameters β, η and F are given by,

$$\beta = -H_{12}\left(H_{11}H_{22}\right)^{-1/2}, \qquad \eta = \left(H_{22}/H_{11}\right)^{1/2} \qquad \text{and } F = \mu_1\left(H_{22} - H_{12}^2/H_{11}\right),$$

and ε is related to β through equation (1.4). The variation of ε and η with crack-tip speed for a PMMA/steel bimaterial system was shown in figures 21 and 22 respectively. The variation of F shown in figure A1 below.

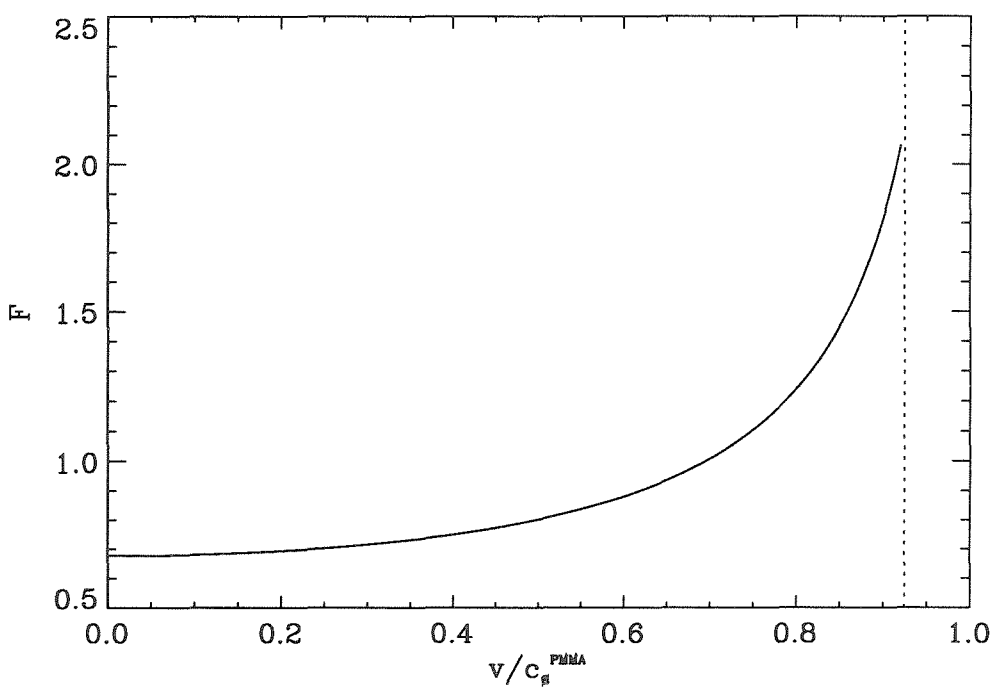

Figure A1: Variation of F with velocity for a PMMA/steel bimaterial system (plane stress conditions).

In addition functions P11 and P12 are defined as (see Yang et al. (1991),

$$P_{11} = \left(1+\alpha_s^2\right)\cosh\varepsilon\left(\pi-\theta_t\right) - 2\eta\alpha_s \sinh\varepsilon\left(\pi-\theta_t\right),$$

and

$$P_{12} = \left(1+\alpha_s^2\right)\sinh\varepsilon\left(\pi-\theta_t\right) - 2\eta\alpha_s \cosh\varepsilon\left(\pi-\theta_t\right).$$